Westfälisch-Wilhelms-Universität Münster
Fachbereich Physik

Diplomarbeit in Physik

Validation and Comparison of Realistic Head Modeling Techniques and Application to Somatosensory E/MEG Data

Benjamin Lanfer

20.09.2007

Gutachter:
Prof. Sergej O. Demokritov
Prof. Christo Pantev

Contents

1 Introduction **5**

2 Theory **7**

2.1 Origin of the Electric Currents in the Brain 7
2.2 Equations for the Electric Potential and the Magnetic Vector Potential . . 9
2.3 Analytical Solutions 13
2.3.1 Analytical Solutions for the EEG 13
2.3.2 Analytical Solution for the MEG 14
2.4 Boundary Element Method 14
2.5 The Finite Element Method 16
2.5.1 FEM Solution for the EEG 16
2.5.2 FEM Solution for the MEG 18
2.5.3 Venant's Approach 19
2.5.4 Subtraction Approach 20
2.5.5 Lead Field Basis Approach 21
2.6 Mesh Generation 22
2.6.1 Generation of the FEM Meshes 22
2.6.2 Generation of the BEM Meshes 24
2.7 SQUIDs 24
2.8 Noise Rejection with Synthetic, Higher Order Gradiometers 28
2.9 Inverse Methods 31
2.9.1 Moving Dipole Fit 31
2.9.2 Goal Function Scan 32

3 Validation of FEM in Multilayer Sphere Models **33**

3.1 Methods 33
3.1.1 Multilayer Sphere Models 33
3.1.2 The Sensor Configurations 35
3.1.3 Generation of the FEM and BEM Meshes 36
3.1.4 Error Measures 40
3.2 Results and Discussion 40
3.2.1 EEG Results 40
3.2.2 Discussion EEG 50
3.2.3 MEG Results 52
3.2.4 Discussion MEG 58

4 The Phantom Study **63**
4.1 Methods . . . 63
4.1.1 Head Phantom . . . 63
4.1.2 MEG Machine . . . 64
4.1.3 Measurement Procedure . . . 64
4.1.4 Generation of the FEM Meshes . . . 65
4.1.5 Inverse Methods . . . 65
4.2 Results and Discussion . . . 66
4.2.1 Results of the Goal Function Scans . . . 66
4.2.2 Discussion of the Goal Function Scan Results . . . 67
4.2.3 Results of the Moving Dipole Fits . . . 70
4.2.4 Discussion of the Moving Dipole Fit Results . . . 75

5 Validation in a Realistic Head Model **77**
5.1 Methods . . . 77
5.1.1 Current Dipoles and Sensor Configurations . . . 77
5.1.2 Generation of the FEM and BEM Meshes . . . 78
5.2 Validation on the Forward Problem . . . 82
5.2.1 Results and Discussion . . . 82
5.3 Validation on the Inverse Problem . . . 86
5.3.1 Results and Discussion . . . 86

6 Application of the Finite Element Method to a SEP/SEF Experiment **89**
6.1 Methods . . . 89
6.1.1 The Somatosensory Experiment . . . 89
6.1.2 Sensor Configurations and FEM Meshes . . . 90
6.1.3 Solving the Inverse Problem . . . 90
6.2 Results and Discussion . . . 90

7 Conclusion **95**

1 Introduction

Brain activity is directly correlated to electric activity in the brain. When a task is processed electric currents in the dimension of a few nAm are flowing in the active area of the brain. These currents produce electric potentials on the surface and magnetic fields outside of the head. The first measurement of a human electroencephalogram (EEG), that is the measurement of the electric potentials on the surface of the head, was done in 1929 by H. Berger[4]. Around forty years later D. Cohen first recorded the magnetic fields produced by the brain, the magnetoencephalogram (MEG)[7]. The sensitivity of the MEG and therefore its importance was increased when superconducting quantum interference devices (SQUIDs) were invented. The first MEG using SQUIDs was recorded in 1972 from D. Cohen et al.[8].

Today electroencephalography and magnetoencephalography are often used, for example in neurophysiological experiments and in clinical applications. In neurophysiological experiments the EEG and the MEG are measured with a high temporal resolution to find out which parts of the brain are active to perform certain tasks and how these parts interact. A clinical application is for example epilepsy research where EEG and MEG are recorded to find the defective area in the brain which causes the epileptic seizures.

In both of the above described applications a central question is how the current density distribution looks like, which generates the recorded electric potentials and magnetic fields. The problem to find this current density distribution is called the *inverse problem*. An essential part of the solution of the inverse problem, the source reconstruction, is to simulate the electric potentials and magnetic fields produced by a given current density distribution. This problem is referred to as the *forward problem*. Analytical solutions for the forward problem only exist when it is assumed that the head as a volume conductor has a special geometry, for example a spherical geometry. For arbitrary geometries of the volume conductor numerical methods are needed to simulate the electric potentials and magnetic fields. There are two numerical methods widely used in the EEG and MEG source reconstruction: the boundary element method (BEM) and the finite element method (FEM). In this thesis the application of the finite element on the simulation of the EEG and the MEG will be validated by showing that FEM can solve the forward problem with a high accuracy that is sufficient to accurately solve the inverse problem. In addition the accuracy of FEM is compared to that of BEM as a competing numerical method. For the FEM computations the implementation of the finite element method into the software *NeuroFEM* was used.

This thesis can be divided into five parts. In the first part, chapter (2), the theoretical background needed for this work is explained. Chapter (3) deals with the validation of the forward computations of the EEG and MEG using the finite element method in multilayer sphere models of varying complexity. in addition BEM and FEM are compared in the multilayer sphere models with regard to their accuracy. In chapter (4)

it is studied on MEG measurements with a spherical phantom head model how accurately the inverse problem can be solved using FEM. After having studied only simple spherical geometries until this point, in chapter (5) the accuracy of the FEM forward computations and the solution of the inverse problem using FEM in a realistic volume conductor is tested. Again the comparison to the boundary element method is drawn. Finally in chapter (6) the finite element method is applied to reconstruct the underlying current density distribution for EEG and MEG data recorded during a real neurophysiological experiment.

2 Theory

In this chapter the theoretical background for the application of the finite element method for the reconstruction of current density distributions from a measured EEG and MEG is explained. First the neurophysiological origin of the electric currents which produce the electric potentials and magnetic flux densities measured with the EEG respectively the MEG is described. Then the equations governing the generation of the potentials and fields by these electric currents are derived and the analytical solutions for special geometries and the numerical solutions for arbitrary geometries are presented. How the very small magnetic fields evoked by the brain are measured, using a technical device called SQUID, and how environmental magnetic noise can be rejected is described in the next sections. Finally the two algorithms employed in this thesis for the solution of the inverse problem are briefly explained.

2.1 Origin of the Electric Currents in the Brain

The magnetoencephalogram and the electroencephalogram measure the magnetic fields respectively the potential differences caused by electric currents in the brain. In this section it will be explained what the origin of these currents is. For this purpose a brief explanation of the basic structure of the brain and its physiology is given.

Anatomically you can differentiate between three parts of the human brain. First there is the brain stem, then there is the cerebellum and finally the telencephalon or cerebrum, which is with more than 80% of the whole brain the biggest and for us the most interesting part as it is responsible for many complex tasks, like processing speech or controlling motor functions, to give just a few examples. The telencephalon itself consists of two hemispheres, which are divided by a deep groove, the medial longitudinal fissure. The two hemispheres of the cerebrum are linked by several bundles of nerve fibres, of which the largest bundle is the corpus callosum.

Each of the two hemispheres of the brain can furthermore be divided into the grey matter at the surface and the white matter beneath the surface. The grey matter layer at the surface of the cerebrum is called cerebral cortex. It consists of a large number (10^9 to 10^{10}) of nerve cells. The white matter is mainly composed of nerve fibres which connect the different regions of the cortex to each other and to other parts of the brain.

The focus will now be on the structure of the cerebral cortex. It is a up to 5 mm thick, strongly folded layer at the surface of the cerebrum. The cortex itself is made up of six layers which are alternately composed of nerve cells, the neurons, and nerve fibres. The neurons of the cortex are mainly ($\approx 80\%$) pyramidal neurons. Information is stored and processed in the cortex by interaction of these neurons.

To see how the neurons can interact and how signals can be transmitted between these

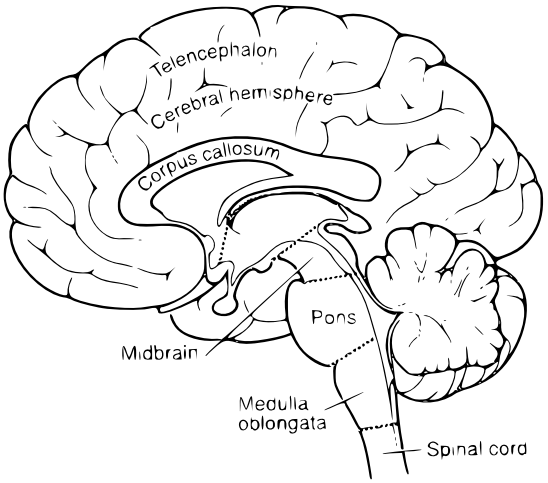

Figure 2.1: The major parts of the brain. Midbrain, pons and medulla oblongata together from the brain stem. From [17].

the basic structure of a neuron will be briefly described. The neuron consists of a cell body, which is called soma, dendrites and an axon. Neurons only have one axon, but they can have many dendrites. The dendrites can receive electric signals from other cells and signals can be transmitted to other cells through the axon. When an neuron is at rest, you can measure a potential of -50 to -80 mV for a pyramidal neuron between the inside of the cell and the outside of the cell, where the inside of the cell is more negative. This potential is called resting membrane potential. It is mainly caused by the diffusion of K^+-ions from the inside of the cell to the outside. The diffusion is driven by the concentration gradient of K^+-ions between the intracellular and the extracellular liquid and continues until the electric force caused by the membrane potential is at equilibrium with the diffusion force caused by the concentration gradient.

Now two mechanisms of signal transmission in and between neurons, which could be causing potential differences and magnetic fields visible in the EEG respectively MEG will be discussed. The first mechanism is the action potential. When by some external stimulus the membrane potential of the neuron is suddenly increased by approximately 20 mV the permeability of the membrane for Na^+-ions grows steeply and sodium ions can diffuse into the cell. This leads to a further depolarization of the cell and causes the action potential, which has an amplitude of 60 to 100 mV. The depolarization also increases, with a certain delay, the permeability of the cell membrane for potassium ions, so that K^+ ions start to diffuse out of the cell. This decreases the membrane potential and the resting potential is restored. In pyramidal cells the generation of the action potential and the restoration of the resting potential happens very fast. The action potential only lasts 0.5 to 2 ms. Because the growth and decay of the potential is so fast and because the excitation of the action potential is not perfectly synchronous between simultaneously active neurons the potential differences and the magnetic fields which are caused by single neurons do not sum up to a signal that can be observed in the EEG

or the MEG.

The second mechanism that will be discussed is the excitatory post synaptic potential (EPSP). The axon of one cell is connected to the dendrite of another cell through a synapse. In most of the synapses the signal is transmitted in a chemical way. When an electric signal reaches the synapse from the axon the synapse emits certain chemical messenger substances. These substances reach the dendrite and increase the membrane potential to more positive values. This depolarization of the dendrites is called excitatory post synaptic potential. It lasts some ten milliseconds. The potential difference between the depolarized dendrite and the soma at resting potential causes electric currents to flow through the liquid outside the cells. If in many, that is some thousand, neighbouring neurons such a potential is excited, the caused potential differences and magnetic fields will sum up and form a signal which can be measured with the EEG or the MEG. In animal experiments, in which simultaneously the potential inside and outside the cell and the EEG was measured, it was shown that this in fact is the case. So we can say, that the origin of the currents that cause the electric potentials and magnetic fields that are measured in the EEG respectively the MEG are the excitatory post synaptic potentials especially of the dendrites close to the surface of the cortex.

2.2 Equations for the Electric Potential and the Magnetic Vector Potential

In this section the governing equations for the electric potential and the magnetic vector potential in the quasi-static approximation are derived. Therefore first the dynamic partial differential equation for the electric potential is derived. Then the different dynamic effects incorporated by this equation are discussed and their size is estimated. Finally the quasi-static approximation for the electric potential and the equation for the magnetic vector potential are presented.

The starting point for the derivation are the Maxwell equations of electro dynamics.

$$\nabla \cdot \mathbf{B} = 0 \tag{2.1a}$$

$$\nabla \times \mathbf{E} + \dot{\mathbf{B}} = 0 \tag{2.1b}$$

$$\nabla \times \mathbf{H} - \dot{\mathbf{D}} = \mathbf{j} \tag{2.1c}$$

$$\nabla \cdot \mathbf{D} = \rho \tag{2.1d}$$

Here $\mathbf{B}$ is the magnetic flux density, $\mathbf{E}$ is the electric field, $\mathbf{H}$ is the magnetic field and $\mathbf{D}$ is the electric displacement field. In addition $\mathbf{j}$ is the current density and ρ is the electric charge.

It can be assumed that biological tissue acts as an electrolyte. So the material equations for a linear, homogeneous medium can be used. Furthermore, as biological tissue is non magnetic, the assumption $\mu_r = 1$ can be made.

$$\mathbf{B} = \mu_0 \mathbf{H} \tag{2.2a}$$

$$\mathbf{D} = \epsilon\epsilon_0\mathbf{E} \tag{2.2b}$$

Here μ_0 denotes the magnetic permeability in free space and ϵ_0 and ϵ stand for the permittivity in free space respectively the relative permittivity.

The current density on the right hand side of equation (2.1c) can be divided into two parts:

$$\mathbf{j} = \mathbf{j}_p + \sigma\mathbf{E} \tag{2.3}$$

The first part, $\mathbf{j}_p$, is the impressed or primary current density, which represents the electric currents in the brain, and the second part, $\sigma\mathbf{E}$, describes the ohmic volume currents. The primary currents have to be stated explicitly, as their generation is not covered by the Maxwell equations, but by some neurophysiological effects, which are outlined in section (2.1). Using this relation (2.3) for the current density in equation (2.1c) results in equation (2.4).

$$\nabla \times \mathbf{H} - \dot{\mathbf{D}} = \mathbf{j}_p + \sigma\mathbf{E} \tag{2.4}$$

Now the scalar electric potential ϕ and the magnetic vector potential $\mathbf{A}$ are introduced. They are defined as follows:

$$\mathbf{B} = \nabla \times \mathbf{A} \tag{2.5a}$$

$$\mathbf{E} = -\nabla\phi - \dot{\mathbf{A}} \tag{2.5b}$$

This definition does not unambiguously determine ϕ and $\mathbf{A}$. Assuming that the vector potential $\mathbf{A}$ fulfils equation (2.5a) and having in mind, that the curl of a gradient of a scalar function is zero, one can see that

$$\widehat{\mathbf{A}} = \mathbf{A} + \nabla\chi \quad \text{and} \quad \widehat{\phi} = \phi - \dot{\chi}$$

with an arbitrary scalar function $\chi = \chi(\mathbf{r}, t)$, also fulfil equations (2.5a) and (2.5b). The scalar function χ can be chosen in such a way that the Lorenz-condition is fulfilled.

$$\nabla \cdot \mathbf{A} + \mu_0\epsilon_0\epsilon\dot{\phi} + \mu_0\sigma\phi = 0 \tag{2.6}$$

As the Maxwell equations with linear material equations are also linear, the Fourier decomposition of j_p, ϕ and $\mathbf{A}$ is possible. Therefore assuming a harmonic time dependency of this quantities is possible.

$$\begin{aligned}
\mathbf{j}_p(\mathbf{r}, t) &= \mathbf{j}_p(\mathbf{r})\, \mathrm{e}^{\mathrm{i}\omega t} \\
\mathbf{A}(\mathbf{r}, t) &= \mathbf{A}(\mathbf{r})\, \mathrm{e}^{\mathrm{i}\omega t} \\
\phi(\mathbf{r}, t) &= \phi(\mathbf{r})\, \mathrm{e}^{\mathrm{i}\omega t}
\end{aligned}$$

To obtain the partial differential equation for the electric potential ϕ the divergence is applied to equation (2.4). Furthermore the linear material equations are employed, the electric field $\mathbf{E}$ is replaced by the electric potential ϕ (Equation (2.5b)) and the assumption of harmonic time dependency is used. This yields the following equation.

$$\nabla \cdot \left(\sigma \left(1 + \frac{\mathrm{i}\omega\epsilon_0\epsilon_r}{\sigma} \right) \nabla\phi + \mathrm{i}\omega\sigma \left(1 + \frac{\mathrm{i}\omega\epsilon_0\epsilon_r}{\sigma} \right) \mathbf{A} \right) = \nabla \cdot \mathbf{j}_p \tag{2.7}$$

This equation describes three kinds of dynamic effects: capacitive effects, propagation effects and inductive effects. These dynamic effects are now discussed and it is shown that they are negligible for the simulation of the EEG and MEG.

Capacitive Effects

The capacitive effects are related to the imaginary part of the factor $\left(1 + \frac{\mathrm{i}\omega\epsilon_0\epsilon_r}{\sigma}\right)$ in equation (2.7). This imaginary part can be taken as the ratio of capacitive currents to resistive currents. Capacitive effects can be neglected, if the capacitive currents are much smaller than the resistive currents. This means

$$\frac{\omega\epsilon_0\epsilon_r}{\sigma} \ll 1.$$

For different biological tissues and for varying frequencies the value of the ratio of capacitive to resistive currents was measured[22]. Table (2.1) shows the measured values.

	10 kHz	100 kHz	1000 kHz
Lung	0.15	0.025	0.05
Fatty Tissue		0.01	0.03
Liver	0.20	0.035	0.06
Heart Muscle	0.10	0.04	0.15

Table 2.1: Measured values for the ratio of capacitive to resistive currents.

The maximum measured value for the ratio is 0.2. For this reason capacitive effects can be neglected when modelling the EEG or the MEG.

Propagation effects

Assuming a infinite homogeneous medium equation (2.7) can be solved using Green's function

$$G_k\left(R\right) = \frac{\mathrm{e}^{-\mathrm{i}kR}}{R} \quad \text{, where} \quad R = \left|\mathbf{r} - \mathbf{r}^{'}\right|. \tag{2.8}$$

This yields equation (2.9) as a solution for the magnetic vector potential.

$$\mathbf{A}\left(\mathbf{r}, t\right) = \frac{\mu_0}{4\pi} \int_{\Omega} \frac{\mathbf{j}_p\left(\mathbf{r}^{'}\right) \mathrm{e}^{\mathrm{i}\omega t - \mathrm{i}kR}}{R} \, \mathrm{d}\Omega \tag{2.9}$$

The propagation effects are represented by the phase factor $\mathrm{e}^{-\mathrm{i}kR}$. By looking at the series expansion of this factor,

$$\mathrm{e}^{-\mathrm{i}kR} = 1 - \mathrm{i}kR - \frac{(kR)^2}{2!} + \mathrm{i}\,\frac{(kR)^3}{3!} \ldots,$$

one can see that it is negligible, if

$$k \cdot R \ll 1.$$

R describes the distance between the source point and the measurement point. The maximum value, R_{max}, can be conservatively choosen as $R_{max} = 1\text{m}$. For EEG and MEG R will in most cases be smaller than this. To estimate the size of k the definition in equation (2.10) can be used.

$$k = (1 - \mathrm{i}) \sqrt{\frac{\omega \mu_0 \sigma}{2} \left(1 + \mathrm{i} \, \frac{\omega \epsilon_0 \epsilon}{\sigma}\right)} \tag{2.10}$$

A good estimate for the frequency ν of the current density is $\nu = 1$ kHz, as the fastest process in the brain is the rise of the action potential which has a duration of around 1 ms. According to table (2.1) it is reasonable to assume a value of $\sqrt{2} - 1$ for the ratio of capacitive to resistive currents. The conductivity is chosen as $\sigma = 0.33 \, \frac{\mathrm{S}}{\mathrm{m}}$. This value is often used as the conductivity of the brain. With these values $k \cdot R$ can be estimated as

$$k \cdot R \approx (1 - \mathrm{i}) 0.04.$$

The error of the magnitude of the phase factor is then approx. 4% and the error of the phase is around 2.5°. Therefore propagation effects can be neglected.

Inductive effects

The left hand side of the dynamic partial differential equation (2.7) can be interpreted as consisting of two parts, a static part and an inductive part.

$$\underbrace{\nabla \cdot \left(\sigma \left(1 + \frac{\mathrm{i}\omega\epsilon_0\epsilon_r}{\sigma}\right) \nabla\phi\right)}_{\text{Static part}} + \underbrace{\mathrm{i}\omega \nabla \cdot \left(\sigma \left(1 + \frac{\mathrm{i}\omega\epsilon_0\epsilon_r}{\sigma}\right) \mathbf{A}\right)}_{\text{Inductive part}} = \nabla \cdot \mathbf{j}_p$$

The inductive part is describing the inductive effects. The influence of the inductive effects can be described using the ratio of the inductive to the static part. Inductive effects can be neglected, if

$$\frac{|\mathrm{i}\omega \mathbf{A}\,|}{|\nabla\phi|} = |k \cdot R|^2 \ll 1 \tag{2.11}$$

This relation is satisfied, as $|k \cdot R| \ll 1$, which was already shown, when estimating the size of propagation effects. This means that inductive effects can be neglected.

Neglecting these dynamic effects in equation (2.7) yields the quasi-static approximation of the Maxwell equations for the electric potential ϕ in equation (2.12).

$$\nabla \cdot (\sigma \, \nabla\phi) = \nabla \cdot \mathbf{j}_p \tag{2.12}$$

The equation for the magnetic vector potential $\mathbf{A}$ (equation (2.13)) is derived using Biot-Savart's law.

$$\mathbf{A}\,(\mathbf{r}, t\,) = \frac{\mu_0}{4\pi} \int\limits_{\Omega} \frac{\mathbf{j}_p\left(\mathbf{r}', t\right)}{R} \, \mathrm{d}\Omega - \frac{\mu_0}{4\pi} \int\limits_{\Omega} \frac{\sigma \, \nabla\phi\left(\mathbf{r}', t\right)}{R} \, \mathrm{d}\Omega \tag{2.13}$$

R means here, as above, the distance between the measurement point, $\mathbf{r}$, and the source point, $\mathbf{r}'$.

$$R = \left| \mathbf{r} - \mathbf{r}' \right|$$

The mathematical formulation of the problem is not complete without boundary conditions. On the interfaces, Γ, between compartments with different conductivity Neumann boundary conditions apply.

$$(\sigma_1 \nabla \phi_1) \cdot \mathbf{n} = (\sigma_2 \nabla \phi_2) \cdot \mathbf{n} \qquad \text{on} \qquad \Gamma \tag{2.14}$$

$\mathbf{n}$ is the normal vector on Γ. For $\Gamma = \partial\Omega$, that is for the surface of the base domain, equation (2.14) becomes

$$(\sigma \nabla \phi) \cdot \mathbf{n} = 0 \qquad \text{on} \qquad \Gamma = \partial\Omega. \tag{2.15}$$

In addition the value of the electric potential at one point has to be set to a defined value.

$$\phi \left(\mathbf{r}^{\text{reference}} \right) \equiv 0 \tag{2.16}$$

2.3 Analytical Solutions for the Quasi-Static Approximation

2.3.1 Analytical Solutions for the EEG

For special geometries of the volume conductor the quasi-static approximation for the electric potential (equation (2.12)) can be solved analytically. An analytical solution exists, for example for a multilayer sphere model, which consists of a number of concentric sphere shells, where the conductivity of each shell is constant. Using the analytical solution the electric potential can be computed easily. Therefore multilayer sphere models were and are still used to model the human head. In this thesis the exact analytical solutions are used as reference solutions to which the numerical solutions are compared.

There exist several formulas for the quasi-static potential in spherical volume conductors of varying complexity. Geselowitz derived in [12] an expression for the potential in a three layer, isotropic sphere model. In this model the sphere shells with constant, isotropic conductivity reflect the conductivity profile of a human head with the three compartments scalp, skull and brain. Another formula was developed by Hosek in [13] to calculate the electric potential in a four layer, isotropic sphere model. The four compartments of this model mirror the compartments scalp, skull, cerebro spinal fluid (CSF) and brain of the human head. Furthermore de Munck presented in [10] a series expansion for the electric potential, which is able to treat an arbitrary number of layers and radial to tangential anisotropic conductivity in each of the layers. Using de Munck's formula the head can be modelled with an anisotropic skull layer, because measurements in for example [2] showed that the skull has an anisotropic conductivity.

2.3.2 Analytical Solution for the MEG

For the MEG, as for the EEG, analytical solutions exist for special geometries. Sarvas, for example, studied the solution of the MEG for spherical volume conductors. In [21] he derived a formula for the magnetic fields outside a sphere. The analytical solution for the MEG has some remarkable characteristics. One of these characteristics is, that the solution does not at all depend on the conductivity profile of the spherical volume conductor. It only depends on the position of the dipole relative to the centre of the sphere. Another important property of the MEG solution is that a radially orientated dipole in a sphere does not produce any magnetic field outside of the sphere. Furthermore Sarvas found that only the primary current density contributes to the radial component of the magnetic field.

2.4 Boundary Element Method

The quasi-static approximation of Maxwell's equations cannot be solved analytically for arbitrary geometries and conductivity profiles of the volume conductor. Therefore numerical methods must be applied to compute the electric potential and the magnetic vector potential. A numerical method which can be used to solve the quasi-static approximation for arbitrary geometries is the boundary element method (BEM). In the next sections it is briefly explained how the electric potential and the magnetic flux density can be numerically calculated using BEM[34].

For the boundary element method it is assumed that the inhomogeneous base domain Ω can be divided into p compartments Ω_i with homogeneous and isotropic conductivities. Γ_i is the outer interface of the compartment Ω_i. In this case an integral equation for the electric potential on i-the interface, $\mathbf{x} \in \Gamma_i$, can be derived.

$$\left(\sigma_i^- + \sigma_i^+\right) \phi\left(\mathbf{x}\right) = 2\phi^\infty\left(\mathbf{x}\right) - \sum_{j=1}^{p} \left(\sigma_j^- - \sigma_j^+\right) \int_{\Gamma_j} k\left(\mathbf{x}, \mathbf{x}'\right) \phi\left(\mathbf{x}'\right) \mathrm{d}\Gamma_j \tag{2.17}$$

$k\left(\mathbf{x}, \mathbf{x}'\right)$ is the dipole kernel,

$$k\left(\mathbf{x}, \mathbf{x}'\right) = -\frac{1}{2\pi} \frac{\mathbf{n}\left(\mathbf{x}'\right) \cdot \left(\mathbf{x}' - \mathbf{x}\right)}{\left|\mathbf{x}' - \mathbf{x}\right|^3},$$

and $\phi^\infty\left(\mathbf{x}\right)$ is the potential of a dipole in an infinite, homogeneous medium,

$$\phi^\infty\left(\mathbf{x}\right) = \frac{1}{4\pi} \frac{\mathbf{M} \cdot \left(\mathbf{x} - \mathbf{x}_0\right)}{\left|\mathbf{x} - \mathbf{x}_0\right|^3}.$$

$sigma^-$ and $sigma^+$ are the conductivites inside respectively outside of the interface $Gamma_i$. To solve this integral equation numerically the interfaces $l = 1, \ldots, p$ are discretised into triangles Δ_m^l. On these triangles basis functions h_n^l and collocation points ξ_n^l are chosen to approximate the electric potential as in equation (2.18).

$$\phi^h = \sum_{l=1}^{p} \sum_{n=1}^{k(l)} \alpha_n^l \, h_n^l \tag{2.18}$$

To determine the potential at the collocation points the coefficients α_l^n have to be computed.

In general for the basis functions polynomials are chosen. Often used are constant and linear basis functions. For a constant collocation the collocation points are the barycentres of the triangles and the basis functions are defined by

$$h_n^l(\mathbf{x}) = \begin{cases} 1 & : \quad \mathbf{x} \in \Delta_n^l \\ 0 & : \quad \mathbf{x} \notin \Delta_n^l \end{cases} . \tag{2.19}$$

For the linear collocation the basis functions

$$h_n^l(\mathbf{x}) = \begin{cases} 1 & : \quad \mathbf{x} = \mathbf{x}_n^l \\ 0 & : \quad \mathbf{x} \neq \mathbf{x}_n^l \end{cases} \tag{2.20}$$

are chosen. The vertices of the triangles are used as collocation points. So at the vertices $\mathbf{x}_m^i$ of the triangle mesh the basis functions can be expressed using the δ function.

$$h_n^l\left(\mathbf{x}_m^i\right) = \delta_{li}\delta_{mn}$$

Inserting the linear basis functions in the integral equation yields equation (2.21).

$$\begin{aligned} \left(\sigma_i^- + \sigma_i^+\right) \sum_{l=1}^{p} \sum_{n=1}^{N(l)} \alpha_n^l h_n^l\left(\mathbf{x}_m^i\right) \\ = 2\,\phi^\infty\left(\mathbf{x}_m^i\right) - \sum_{j=1}^{p} \left(\sigma_j^- - \sigma_j^+\right) \int_{\Gamma_j} k\left(\mathbf{x}_m^i, \mathbf{x}'\right) \sum_{n=1}^{N(j)} \alpha_n^j h_n^j\left(\mathbf{x}'\right) \mathrm{d}\Gamma_j \end{aligned} \tag{2.21}$$

This equation can be written as a matrix equation $\mathbf{A} \cdot \mathbf{a} = \mathbf{b}$, that can be solved to obtain the potential at the vertices of the triangle mesh.

For the magnetic flux density also an integral equation can be found.

$$\mathbf{B}(\mathbf{x}) = \mathbf{B}^\infty(\mathbf{x}) + \mu_0 \sum_{l=1}^{p} \left(\sigma_j^+ - \sigma_j^-\right) \int_{\Gamma_j} \left(\phi_i\left(\mathbf{x}'\right) \nabla \frac{1}{|\mathbf{x} - \mathbf{x}'|}\right) \times \mathrm{d}\Gamma_j \tag{2.22}$$

When inserting the approximation for the electric potential (2.18) into this equation it can be rewritten as a matrix equation.

$$\mathbf{B} = \mathbf{S} \cdot \mathbf{a} \tag{2.23}$$

So the magnetic flux density $\mathbf{B}$ can be computed when the potential at the vertices of the triangle surfaces mesh is known.

2.5 The Finite Element Method

A second numerical method, which is widely used in scientific and engineering applications and able to treat arbitrary geometries, is the finite element method (FEM)[23]. In the following section the application of FEM to the simulation of the EEG and MEG is presented. In addition two different ways of modelling the mathematical current dipole are presented and an very efficient method to compute the potential and flux with regard to the inverse problem is described.

2.5.1 Finite Element Method Solution for the EEG

To solve a differential equation using FEM first the base domain has to be discretised. This is done by separating the base domain into smaller regions, the elements. Often used elements are tetrahedra and hexahedra. In the simulations for this thesis tetrahedra, regular hexahedra and deformed hexahedra elements are used.

Then for the elements an appropriate ansatz function has to be chosen. Very common as ansatz functions are polynomials. For the FEM computations with tetrahedra elements in this thesis a linear ansatz function was chosen.

$$ {}^{(e)}\phi^h(x,y,z) = c_1 + c_2x + c_3y + c_4z \tag{2.24} $$

For the hexahedra elements in the FEM computations a bilinear ansatz was used.

$$ {}^{(e)}\phi^h(x,y,z) = c_1 + c_2x + c_3y + c_4z + c_5xy + c_6xz + c_7yz \tag{2.25} $$

As the electric potential is continuos the approximation of the potential has to be continuous, too. The continuity can more easily be guaranteed when turning from the element based ansatz function ${}^{(e)}\phi^h$ to the node based form functions ${}^{(e)}\psi_k$. For a single element the form functions are defined by equation (2.26).

$$ {}^{(e)}\phi^h(x,y,z) = \sum_i^p {}^{(e)}u_k \, {}^{(e)}\psi_k(x,y,z) \tag{2.26} $$

p is the number of nodes of the element and the ${}^{(e)}u_k$ are called *node variables*. As equation (2.26) has to be fulfilled for any choice of values for the node variables, the form function ${}^{(e)}\psi_k$ has to be 1 at the node P_k and 0 at all other nodes, $P_{j\neq k}$, of the element. Let $\mathbf{r}_j$ be the coordinates of the node P_j then this characteristic of the form functions is described by equation (2.27).

$$ {}^{(e)}\psi_k(\mathbf{r}_j) = \begin{cases} 1, & \text{if } j = k \\ 0, & \text{if } j \neq k \end{cases} \tag{2.27} $$

The ansatz for the whole base domain is now constructed piecewise from the ansatz functions for the single elements. As discussed above using node based form functions is of advantage. Therefore the nodes of all elements are numbered consecutively and *global form functions*, ψ_k, are introduced. The global form function ψ_k is composed of

all the local form functions which are 1 at node k. Due to this construction the global form function ψ_k is only non-zero in the elements to which the node k belongs. Now the ansatz for the electric potential in the whole base domain can be written as in equation (2.28).

$$\phi^h(x,y,z) = \sum_k^n u_k \psi_k(x,y,z) \tag{2.28}$$

Next *Galerkin's method* is applied to the partial differential equation (2.12).Therefore the ansatz (2.28) is inserted into the differential equation. For an arbitrary choice of the node variables u_k the equation will in general not be solved exactly, but there still is a residuum.

$$R(x,y,z) = \sum_k^n u_k \nabla \cdot (\sigma \nabla \psi_k(x,y,z)) - \nabla \cdot \mathbf{j}_p \tag{2.29}$$

Following the *method of weighted residues* the node variables u_k shall now be chosen in such a way that the residuum weighted with functions w_j integrated across the whole base domain Ω is zero.

$$\int_\Omega R(x,y,z)\; w_j \; \mathrm{d}\Omega \stackrel{!}{=} 0\,, \qquad j = 1,\ldots,n \tag{2.30}$$

In Galerkin's method the weighting functions are chosen equal to the form functions, $w_j = \psi_j$. Applying furthermore Green's formula results in equation (2.31).

$$\sum_k^n \underbrace{\int_\Omega (\sigma \nabla \psi_k) \cdot \nabla \psi_j \; \mathrm{d}\Omega}_{\equiv K_{jk}} + \underbrace{\int_\Omega (\nabla \cdot \mathbf{j}_p)\, \psi_j \; \mathrm{d}\Omega}_{\equiv -J_j} = 0 \tag{2.31}$$

The surface integral from applying Green's formula is zero because of the homogeneous boundary conditions on the surface of the base domain. In addition the equation was multiplied with -1.

An important characteristic of the stiffness matrix can be seen directly from its definition. When remembering that the ansatz function ψ_k is only non-zero in elements that belong to the node k, it is obvious that the integrand in the definition of $\mathbf{K}$ is only non-zero when j and k are nodes of the same finite element, that is neighbouring nodes. Because of this one row of the stiffness matrix only has as many non-zero entries as a node has neighbours. So the stiffness matrix is sparsely populated with only around 30 or 40, depending on the element type, non-zero entries. Due to this fact and due to the fact that $\mathbf{K}$ is in addition symmetric the matrix can be handled on a common desktop computer with limited memory even for FE meshes with hundreds of thousands of nodes.

With the definitions of the stiffness matrix $\mathbf{K}$, the potential vector $\mathbf{u}$ and the source vector $\mathbf{J}$ equation (2.31) can be rewritten as a matrix equation.

$$\mathbf{K} \cdot \mathbf{u} = \mathbf{J} \tag{2.32}$$

This equation can be solved in a computer to get $\mathbf{u}$, the electric potential at the nodes of the finite element mesh.

2.5.2 Finite Element Method Solution for the MEG

The magnetic flux through the coil of a sensor is often computed as the integral of the magnetic flux density across the face of the sensor. Using FEM it is more convenient to reformulate the equation for the magnetic flux using Stoke's formula.

$$\Phi = \int_S \mathbf{B} \cdot \mathrm{d}\mathbf{S} = \int_S (\nabla \times \mathbf{A}) \cdot \mathrm{d}\mathbf{S} = \int_{C \equiv \partial S} \mathbf{A} \cdot \mathrm{d}\mathbf{C} \tag{2.33}$$

Now that it is integrated along the contour of the coils this contour has to be modelled with bar elements, which can be straight or curved. For the simulations in this thesis curved bar elements were used, which better approximate the geometry of the circular coils[19].

Using the magnetic vector potential from equation (2.13) in the magnetic flux from equation (2.33) yields equation (2.34).

$$\Phi_j = \underbrace{\frac{\mu_0}{4\pi} \oint_{C_j} \int_{\Omega} \frac{\mathbf{j}_p\left(\mathbf{r}'\right)}{R} \, \mathrm{d}\Omega \cdot \mathrm{d}\mathbf{s}}_{\text{Primary Magnetic Flux } \Phi_j^p} \underbrace{- \frac{\mu_0}{4\pi} \oint_{C_j} \int_{\Omega} \frac{\sigma \nabla \phi\left(\mathbf{r}'\right)}{R} \, \mathrm{d}\Omega \cdot \mathrm{d}\mathbf{s}}_{\text{Secondary Magnetic Flux } \Phi_j^s} \tag{2.34}$$

The separation of the electric current density $\mathbf{j}$ into an primary, impressed current and the secondary, volume currents also shows in this formula for the magnetic flux. It consists of two parts. The first one, the primary magnetic flux, describes the contribution of the impressed current to the magnetic flux and the second part, the secondary magnetic flux, describes the contributions of the volume currents.

As the electric current density is always assumed to be a mathematical dipole (see section (2.3.1)) the expression for the primary magnetic flux can be calculated using equation (2.35).

$$\Phi_j^p = \frac{\mu_0}{4\pi} \mathbf{M} \cdot \underbrace{\oint_{C_j} \frac{1}{|\mathbf{r}' - \mathbf{r_0}|} \, \mathrm{d}\mathbf{s}}_{\equiv \mathbf{I}_j} = \frac{\mu_0}{4\pi} \mathbf{M} \cdot \mathbf{I}_j \tag{2.35}$$

$\mathbf{r}_0$ denotes the coordinates of the current dipole. The integrand in the above formula can be calculated analytically, while the integration is performed numerically on the bar elements, with which the sensor coils are modelled.

To calculate the secondary magnetic flux first the ansatz (2.28) is inserted for the

electric potential.

$$\Phi_j^s = -\frac{\mu_0}{4\pi} \sum_{k=1}^{n} u_k \underbrace{\left\{ \oint_{C_j} \int_{\Omega} \frac{\sigma \nabla \psi_k \left(\mathbf{r}' \right)}{|\mathbf{r} - \mathbf{r}'|} \, \mathrm{d}\Omega \cdot \mathrm{d}\mathbf{s} \right\}}_{\equiv S_{jk}} \tag{2.36}$$

$\mathbf{S}$ is the secondary magnetic flux integration matrix[19]. Equation (2.36) can be rewritten into a matrix equation.

$$\mathbf{S} \cdot \mathbf{u} = \mathbf{\Phi}^s \tag{2.37}$$

To compute the secondary magnetic flux, first the electric potential at every node of the FEM mesh has to be computed. One can interpret the matrix entry S_{jk} of the secondary magnetic flux integration matrix as the magnetic flux a unit potential at node k would cause at the sensor j.

2.5.3 Venant's Approach for Modelling the Mathematical Dipole

When numerically computing the electric potential one has to model the mathematical current dipole. One method used for the dipole modelling is *Venant's approach*.

The mathematical current dipole $\mathbf{j}_p(\mathbf{r}) = \mathbf{M} \cdot \delta(\mathbf{r} - \mathbf{r}_0)$ can be defined by two monopoles, that is one current source and one current sink, which are positioned equally far away from the dipole location on the axis defined by the vector $\mathbf{M}$.

$$j_p = \lim_{\substack{J \to \infty \\ d \to 0}} \left\{ J\left(+\frac{d}{2}\right) - J\left(-\frac{d}{2}\right) \right\} = \lim_{\substack{J \to \infty \\ d \to 0}} J \cdot d \tag{2.38}$$

In the limit of $J \to \infty$ and $d \to 0$ the dipole moment $M = Jd$ shall be constant.

In addition the divergence of the current density, $\mathbf{j}_p$, can, in analogy to Gauß' law of electrostatics, be expressed using the current sources J_p.

$$\nabla \cdot \mathbf{j}_p = J_p \tag{2.39}$$

Following Venant's principle, it is not important for the electric fields far away from the source location, how, in detail, the monopoles are distributed to form a current dipole. Therefore in the Venant approach, the mathematical dipole can be modelled by placing current sources and sinks on finite element nodes in the immediate vicinity of the current dipole. This is done by first finding the FE node which is closest to the source. Then for this node the neighbouring nodes of the FE mesh are searched. The current sources and sinks are then distributed on these neighbouring nodes.

How the values of the nodal loads J_k have to be chosen to form a current dipole with the dipole moment $\mathbf{M}$ is described in detail in [5]. In general the first order moment in the direction of $\mathbf{r}$ at node i, ${}^{n_0}M_i^r$, is related to the nodal loads J_k as stated in equation (2.40).

$${}^{n_0}M_i^r = \left(\frac{\Delta x_{ik}^r}{a_{\mathrm{ref}}} \right)^{n_0} J_k \tag{2.40}$$

Here Δx_{ik}^r means the r-component of the distance between node k and the source node i, n_0 is the order of the moment and a_{ref} is a reference length, which guarantees that the series $\left(\frac{\Delta x_{ik}^r}{a_{\text{ref}}}\right)^{n_0}$ converges to 0 for $n_0 \to \infty$.

2.5.4 Subtraction Approach for Modelling the Current Dipole

The second approach which is used in this work to model the mathematical current dipole is the *subtraction approach*[36]. This approach is based on the fact, that many numerical difficulties arise from the singularity of the dipole current distribution. Therefore the conductivity and the potential are split into two parts.

$$\sigma = \sigma^{\infty} + \sigma^{\text{corr}} \tag{2.41}$$

$$\phi = \phi^{\infty} + \phi^{\text{corr}} \tag{2.42}$$

σ^{∞} stands for the conductivity in the region around the current dipole, in which this conductivity is assumed to be homogeneous. ϕ^{∞}, the infinity potential is supposed to deal with the singularity at the dipole location. It is the potential generated by the dipole in an infinite, homogeneous volume conductor. For this potential the Poisson-equation (2.43) applies.

$$\Delta\phi^{\infty} = \frac{\nabla \cdot \mathbf{j}_p}{\sigma^{\infty}} \tag{2.43}$$

As ϕ^{∞} does not accurately describe the electric potential in a realistic volume conductor, the correction potential, ϕ^{corr}, is introduced to correct the potential with respect to the volume conductor.

The approaches for ϕ, equation (2.42), and σ, equation (2.41), can now be inserted into the quasistatic approximation. The resulting relation can be simplified by using the Poisson equation for the infinity potential.

$$\nabla \cdot (\sigma \nabla \phi^{\text{corr}}) = -\nabla \cdot ((\sigma - \sigma^{\infty}) \nabla \phi^{\infty}) \tag{2.44}$$

When using these approaches the boundary conditions are no longer homogeneous.

$$(\sigma \nabla \phi^{\text{corr}}) \cdot \mathbf{n} = -(\sigma \nabla \phi^{\infty}) \cdot \mathbf{n} \qquad \text{on} \qquad \Gamma = \partial\Omega \tag{2.45}$$

This relation means that the currents which would flow out of the base domain due to the potential of a dipole in an unbounded medium have to be compensated by opposite currents caused by the gradient of the correction potential.

For this partial differential equation an ansatz similar to equation (2.28) is chosen for the correction and the infinity potential and a matrix equation is derived, again following Galerkin's method.

$$\mathbf{K} \cdot \mathbf{u}^{\text{corr}} = \mathbf{J}^{\text{corr}} \tag{2.46}$$

The stiffness matrix is the same as for the finite element method using Venant's approach. $\mathbf{u}^{\text{corr}}$ is the correction potential vector and $\mathbf{J}^{\text{corr}}$ is defined by equation (2.47).

$$\mathbf{J}^{\text{corr}} = -\mathbf{K}^{\text{corr}} \cdot \mathbf{u}^{\infty} - \mathbf{S} \cdot \mathbf{u}^{\infty} \tag{2.47}$$

The definition of $\mathbf{K}^{\text{corr}}$ and $\mathbf{S}$ is given in equation (2.48) respectively (2.49).

$$K_{ij}^{\text{corr}} = \int_{\Omega} \left((\sigma - \sigma^{\infty}) \nabla \psi_i \right) \cdot (\nabla \psi_j) \, \mathrm{d}\Omega \tag{2.48}$$

$$S_{ij} = \int_{\Gamma} (\sigma^{\infty} \nabla \psi_j) \cdot \mathbf{n} \, (\nabla \psi_i) \, \mathrm{d}\Gamma \tag{2.49}$$

The ψ_i are here the node based global ansatz functions. To calculate the total electric potential at the nodes of the FE mesh, first the potential caused by the dipole in an infinite, homogeneous medium is analytically computed. Then the correction potential is computed numerically by solving the system of equations (2.46). Summing up the inifinity potential and the correction potential yields the total electric potential.

2.5.5 Lead Field Basis Approach

With regard to the inverse problem it is necessary to compute the electric potentials and magnetic fields for potentially many thousand dipoles. Solving a FE equation system as in equation (2.32) for each of the dipoles would last a long time. Therefore the associativity of the matrix multiplication is exploited in a trick to speed up the simulations. This method is called the lead field basis approach for EEG[33] and MEG[11, 38].

When solving the inverse problem one is not interested in the electric potential at every node of the FE mesh, but only in the potential at the EEG electrodes. To extract the potentials at the electrodes, $\mathbf{u}^{\text{EEG}}$, from the potential vector, $\mathbf{u}$, a restriction matrix $\mathbf{R}$ is applied.

$$\mathbf{u}^{\text{EEG}} = \mathbf{R} \cdot \mathbf{u} \tag{2.50}$$

$\mathbf{R}$ is a $s \times n$ matrix, where s is the number of sensors and n is the number of FE nodes. R_{ij} is 1 if the FE node j models the electrode i.

Although the stiffness matrix, because of the usually large number of nodes, cannot be inverted directly equation (2.50) can still be rewritten formally using equation (2.32).

$$\mathbf{u}_{\text{EEG}} = \mathbf{R} \left(\mathbf{K}^{-1} \mathbf{J} \right) = \left(\mathbf{R} \, \mathbf{K}^{-1} \right) \mathbf{J} = \mathbf{B}_{\text{EEG}} \, \mathbf{J} \tag{2.51}$$

Here $\mathbf{B}_{\text{EEG}}$, the lead field basis for the EEG, is introduced. One can see from equation (2.51) that it is possible to calculate the electric potential at the electrodes by a simple and fast matrix-vector-multiplication when the lead field basis $\mathbf{B}_{\text{EEG}}$ is known.

To calculate the lead field basis for the EEG its definition is multiplied with $\mathbf{K}$ from the right side and transposed. In addition the fact that the stiffness matrix $\mathbf{K}$ is symmetric is applied.

$$\mathbf{K} \, \mathbf{B}_{\text{EEG}}^{t} = \mathbf{R}^{t} \tag{2.52}$$

The rows of $\mathbf{B}_{\text{EEG}}$ can now be computed by solving the system of equations (2.52) s times for the column vectors of $\mathbf{R}^{t}$.

A very similar thing can be done for the calculation of the secondary magnetic flux for the MEG. The secondary magnetic flux can be written as in equation (2.53).

$$\mathbf{\Phi}^{s} = \mathbf{S} \, \mathbf{u} = \mathbf{S} \left(\mathbf{K}^{-1} \right) \mathbf{J} \big) = \left(\mathbf{S} \, \mathbf{K}^{-1} \right) \mathbf{J} = \mathbf{B}_{\text{MEG}} \, \mathbf{J} \tag{2.53}$$

Here the lead field basis for the MEG, $\mathbf{B}_{\mathrm{MEG}}$, is defined, which allows computing the secondary magnetic flux with one simple matrix-vector-multiplication. The definition of the lead field basis can, as above, be multiplied with $\mathbf{K}$ from the right and transposed. The result is equation (2.54).

$$\mathbf{K}\,\mathbf{B}_{\mathrm{MEG}}^{t} = \mathbf{S}^{t} \tag{2.54}$$

The lead field basis for the MEG can be computed by solving the above system of equations for the s column vectors of the transposed secondary magnetic flux integration matrix, $\mathbf{S}^{t}$.

2.6 Mesh Generation

For the simulation of the electric field or the magnetic flux the geometry and the conductivity profile of the volume conductor have to be represented somehow. For the boundary element method triangle surface meshes represent the boundaries of the different head compartments. For the finite element method the head volume has to be represented with tetrahedra or hexahedra meshes. In this section the generation of these BEM and FEM meshes shall be described briefly.

In the studies for this work for the generation of a finite element or boundary element mesh first a MR image of the head was segmented. The results of the segmentation are surfaces describing the boundaries between the different compartments of the head. These surfaces are the starting point for the mesh generation.

2.6.1 Generation of the FEM Meshes

Tetrahedra Meshes - Ordinary Delaunay Tetrahedralisation

For the FE simulations tetrahedra meshes that were constructed using two different approaches were used. The first one uses a simple Delaunay tetrahedralisation[31, 35].

In a first step element nodes, so called vertices, are distributed on the segmented boundaries of the MR image. Additionally vertices are distributed on surfaces which are generated by eroding the innermost segmented boundary. Now vertices are spread across the whole head volume. From these vertices tetrahedra are then constructed by combining four vertices to form one tetrahedron in such a way that the *Delaunay criterion* is fulfilled. The Delaunay criterion demands that no vertex lies in the circumcircle of a tetrahedra. The four vertices of the tetrahedron lie on the circumcircle. Figure (2.2(a)) illustrates this criterion. In the first method the tetrahedralisation of all the vertices which fulfils the Delaunay criterion is constructed using an iterative algorithm. To explain this algorithm it is assumed that already a tetrahedralisation of a part of the volume exists. All the orientated surface triangles of this tetrahedralisation are now inserted into a queue. From this queue than the first triangle is taken and the one vertex is searched, with which the triangle forms a tetrahedron satisfying the Delaunay criterion. If the surface triangles of the new tetrahedron were already in the queue, they are deleted from the queue. If they were not yet in the queue they are added to it. In

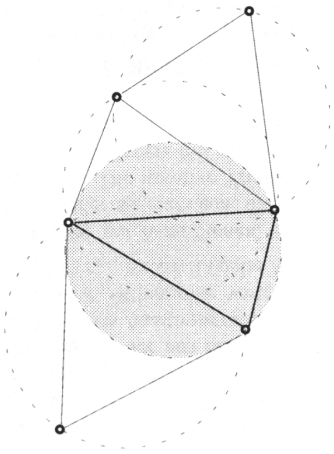

(a) The delaunay criterion. From [35].

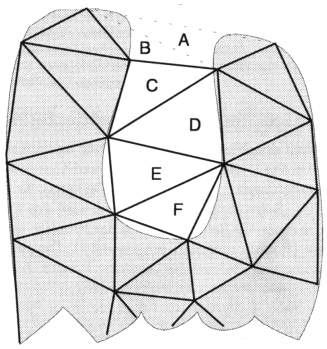

(b) The deletion of tetrahedra lying outside of the volume to be meshed. From [35].

Figure 2.2: On the tetrahedra mesh generation.

this way from all the triangles in the queue tetrahedra are created, which leads to a tetrahedralisation of the whole volume.

It can happen that in this way tetrahedra are constructed that lie outside of the volume, that should be meshed. This situation is shown in figure (2.2(b)). These tetrahedra are removed by an additional iterative algorithm. This algorithm loops across all the surface triangles and checks for the tetrahedra the surface triangle belongs to if they are lying inside or outside the volume. The decision if it lies inside or outside can be based on several criteria. Two criteria are, for example, if the centre of gravity respectively the centre of the circumsphere of the tetrahedra lies inside the volume.

Tetrahedra Meshes - Constrained Delaunay Tetrahedralisation

An improved method to generate a FE tetrahedra mesh is the constrained Delaunay tetrahedralisation[25]. The starting point for this method are surface meshes describing the boundaries of the compartments. The constrained Delaunay tetrahedralisation now constructs a tetrahedra mesh, which always respects this boundary. This is no tetrahedron crosses the provided compartment boundaries. This leads to a better geometrical approximation of the volume conductor.

Furthermore the second approach for tetrahedra mesh generation allows to define a volume constraint for each compartment and a quality constraint. When a volume constraint is applied the tetrahedra are iteratively refined by inserting new vertices, so that the mesh contains no tetrahedra with a larger volume than specified with the volume constraint. Providing a quality constraint generates tetrahedra meshes with tetrahedra of a very regular shape. This is important to avoid numerical errors.

Hexahedra Meshes

To discretise the volume conductor in this work also hexahedra elements were used. The generation of the hexahedra FEM meshes is more simple than the tetrahedra mesh generation. Starting from a MR image the voxels of the images are subsampled, that is a number of voxels is combined to form a larger hexahedron. The hexahedron then belongs to the compartment to which the majority of its voxels belong.

To smooth the stair-step like surfaces of a regular hexahedra mesh the hexahedra can be deformed using the *nodeshift approach*[37] to better represent the smooth boundaries of the volume conductor. Following this approach for each node lying on the boundary between two compartments it is counted how many of the eight neighbouring elements of the node belong to which compartment. If less than four elements belong to one compartment the node is shifted towards this minority compartment. Figure (2.3) shows how this method works.

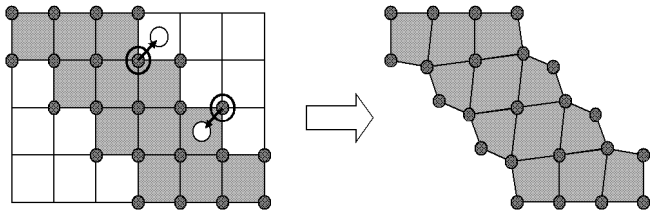

Figure 2.3: The nodeshift approach for hexahedra mesh generation. From [35].

2.6.2 Generation of the BEM Meshes

The starting point for the generation of the BEM meshes is again a segmented boundary of the MR image. Vertices are then distributed on the boundary. The distance of two neighbouring vertices on the surface determines the edge length of the surface triangles that will be constructed. As for the generation of the ordinary Delaunay tetrahedralisation the boundary is now eroded in several steps to create new boundaries. On all of the new boundaries vertices are distributed and the ordinary Delaunay tetrahedralisation for all the vertices is constructed. The surface triangles of the tetrahedralisation of the volume inside the boundary then form the triangulation of the surface, that is the BEM mesh.

2.7 Superconducting Quantum Interference Devices

The magnetic fields produced by the currents in the brain are of the order of magnitude of typically 100 fT, which is many times less than, for example, the magnetic field of the earth. Therefore very sensitive sensors are needed to measure these extremely small fields. In commercially available MEG systems *superconducting quantum interference devices* (*SQUID*), which are sensitive enough to detect the magnetic fields generated by

brain activity, are used. In this section it will be explained how SQUIDs work. To do this first a few aspects of superconductivity have to be discussed[20].

The phenomenon that in certain substances the electric resistivity drops to values, which cannot be measured, when the substance is cooled down to temperatures near absolute zero is called superconductivity. In a microscopic theory the special properties of a superconductor are explained by the formation of electron pairs, called Cooper pairs. The formation of the pairs happens by an indirect interaction in which one electron excites a vibrational state of an atom of the lattice, a phonon, which is immediately absorbed by a second electron. When assuming that the current density is homogeneous, that is the momentum of all electron pairs is the same, the Cooper pairs can be described by one *electron pair wave function*.

$$\Psi_P = \Psi \, \mathrm{e}^{\mathrm{i}(\mathbf{P}\cdot\mathbf{r})/\hbar} \tag{2.55}$$

$\mathbf{P}$ is here the momentum. The current density of the supercurrent is related to this momentum by equation (2.56).

$$\mathbf{j} = \frac{e n_s \mathbf{P}}{2m} \tag{2.56}$$

e and m are here the charge respectively the mass of an electron and n_s is the density of electrons in the superconducting state. The momentum of the electron pairs in the superconducting state cannot exceed a certain maximum value. Therefore there also is a maximum current density for the supercurrent, the *critical current*. When the current density is increased above the critical current the specimen goes from the superconducting state to the state with normal resistivity.

Because the electron pairs in the superconducting state can move through the lattice of a solid without being scattered, the wave is coherent over a infinite distance and interference of the wave with other electron pair waves or itself is possible. The coherence is important, for example for the case of a superconducting loop. The wave function of the electron pairs propagating through the loop has to be unique. To avoid that the function gets multivalued the phase difference of the wave after propagating around the loop must be an integer multiple of $2\,\pi$.

$$\Delta\phi \stackrel{!}{=} n\,2\pi \tag{2.57}$$

For the discussion how a SQUID works it is, in addition, important to explain how an applied magnetic field affects the electron pair wave function. Assuming that first the applied field is zero and then switched on, it induces a circular current in the loop. In a normally conducting loop this induced current would die away in a short time due to the resistivity of the loop. For the superconducting loop this is not the case. Here the induced current flows without being attenuated. If the induced supercurrent is less than the critical current the supercurrents can generate a magnetic field, so that the generated magnetic flux cancels out the externally applied magnetic flux.

An applied magnetic field furthermore causes a phase difference of the electron pair wave. This phase difference for a wave that propagates in a superconductor from point

X to Y can be written as in equation (2.58).

$$\Delta\phi\,(B) = \frac{4\pi e}{h} \int_X^Y \mathbf{A} \cdot \mathrm{d}\mathbf{l} \tag{2.58}$$

Here $\mathbf{A}$ is the magnetic vector potential. For a not too thin closed superconductor loop, where the phase condition (2.57) has to be met, equation (2.58) indicates that the flux enclosed by the loop can only have values which are an integer multiple of the magnetic flux quantum $\Phi_0 = \frac{h}{2e}$.

As a final prerequisite it is described what Josephson junctions are and how they influence the phase of the electron pair wave. Josephson connections are very thin ($< 10^{-9}\,\mathrm{m}$) insulating layers between two superconductors. By an effect called Josephson tunnelling the Cooper pairs can tunnel through the junction and a resistanceless current can flow. Between the electron pair waves on both sides of the junction there is a phase difference which is related to the current through the insulating layer, i, by equation (2.59).

$$i = i_c \,\sin\left(\Delta\phi\,(i)\right) \tag{2.59}$$

i_c is the critical current of the Josephson junction. Currents larger than i_c cannot flow resistanceless through the junction. When a larger current than i_c is tunnelling through the Josephson contact a voltage difference can be measured across the junction. This voltage difference depends on the total tunnelling current i.

Basically a SQUID consists of a superconducting ring with two Josephson junctions. The critical current of the junctions is much smaller than that of the superconductor, so that the current density can be assumed to be low. This means that the momentum of the electron pairs is small and therefore their wavelength is long. As the wavelength is long the phase difference between any two points in one superconductor is, in the absence of a magnetic field, negligible. Furthermore it is assumed that the superconductor is cooled down below its transition temperature with no external magnetic field applied.

Now a magnetic field is applied and a circular current is induced in the ring. For the special SQUID that is described here, the assumption that the inductance L is small, so that $L\,i_c \ll \Phi_0$, is made. This means that the circular currents in the ring can only generate a flux which is much smaller than the magnetic flux quantum and cannot compensate the flux produced by the applied magnetic field. The net flux enclosed by the superconducting loop is then approximately equal to the flux caused by the externally applied magnetic field.

For the electron pair wave in the ring the phase condition (2.57) must still be fulfilled. To the total phase difference of the wave the applied magnetic field and the two Josephson junctions contribute according to equations (2.58) resp. (2.59). This yields condition (2.60).

$$\Delta\phi\,(i) + \frac{1}{2}\,\Delta\phi\,(B) \stackrel{!}{=} n\,2\pi \tag{2.60}$$

The phase shift due to the Josephson junctions can be positive or negative depending on the direction of the current i through the superconducting ring. So one can think of

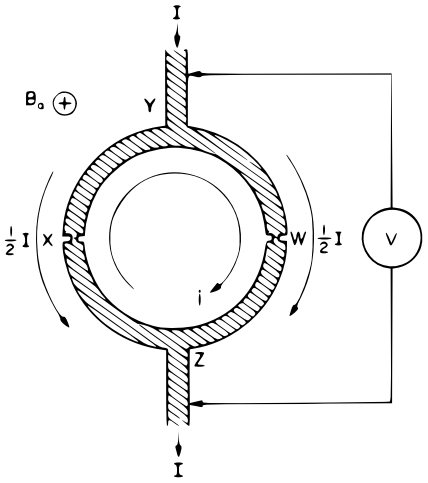

Figure 2.4: Superconducting ring with two Josephson junctions. A dc bias current is applied.

two currents which fulfil the phase condition. One flowing clockwise through the ring and the other one flowing counter-clockwise. When increasing the externally applied magnetic field from $\Phi_a = 0$ to $\Phi_a = \frac{1}{2}\,\Phi_0$ the counter-clockwise current i^-, which by convention produces a negative phase shift, is energetically more favourable. Using the phase condition (2.60) the magnitude of the counter-clockwise current can be described by equation (2.61).

$$\left|i^-\right| = i_c \left|\sin\left(\pi\,\frac{\Phi_a}{\Phi_0}\right)\right| \tag{2.61}$$

For the interval between $\Phi_a = \frac{1}{2}\,\Phi_0$ and $\Phi_a = \Phi_0$ a clockwise current i^+, which produces a positive phase change is energetically more favourable. The magnitude of the current i^+ depending on the externally applied flux is equal to the magnitude of i^-.

The current i through the superconducting ring with two Josephson junctions is periodically depending on the applied magnetic flux Φ_a as can be seen from equation (2.61). This periodic dependence with very small period Φ_0 is the basis for the measurement of the magnetic flux using a SQUID.

The current through the superconducting ring is not easy to measure. Because of this in a SQUID the ring is biased with the measurement current I. In the dc-SQUID, which is discussed here, the ring is biased with a dc-current as it is illustrated in figure (2.4). Assuming that the ring is symmetric the current I splits up equally along the two arms of the ring. Now the total current, consisting of the induced current i and the bias current I, through the Josephson junction at W is different than the total current through the junction at X. Using the phase condition one can now find the inequality (2.62).

$$I \leq 2i_c \left|\cos\left(\pi\,\frac{\Phi_a}{\Phi_0}\right)\right| \tag{2.62}$$

If the current I is too large and does not fulfil this condition then not all electrons, which are carrying the currents, are in the superconducting state. The maximum current still

fulfilling the inequality (2.62) is called the critical measurement current I_c.

$$I_c = 2i_c \left| \cos\left(\pi \frac{\Phi_a}{\Phi_0} \right) \right| \tag{2.63}$$

For currents larger than the critical measurement current a voltage drop across the SQUID appears. As can be seen from equation (2.63) the critical measurement current depends periodically on the applied magnetic flux with period Φ_0. As the voltage drop across the SQUID for currents I larger than I_c is directly related to the critical measurement current, the voltage is also changing periodically with changing applied magnetic flux Φ_a. The very small period of the voltage change makes it possible to detect changes of the applied magnetic flux smaller than the magnetic flux quantum Φ_0. This voltage output can be measured directly to measure the applied magnetic flux.

In commercial MEG systems with low T_c-SQUIDs the SQUIDs furthermore do not directly measure the magnetic flux generated by electric currents in the brain. The MEG sensors instead consist of superconducting pick-up coils, an input coil and the SQUID. The pick-up coils are located in the dewar as close as possible to the head. A few examples of pick-up coil shapes often used can be seen in figure (2.5). Magnetic flux generated by brain activity induces currents in these pick-up coils. These currents then flow through the input coil which is very close to the SQUID. The magnetic flux produced by the currents through the input coil can then be measured by the SQUID.

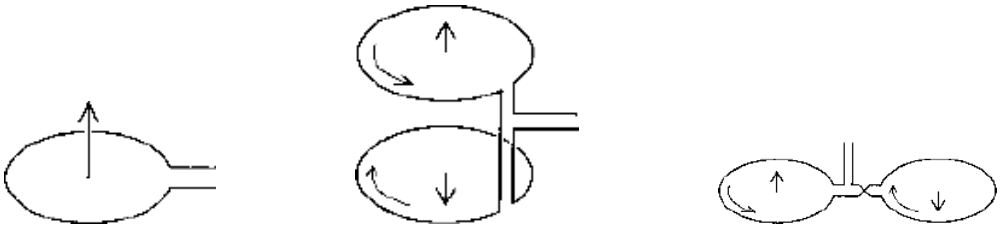

(a) Magnetometer (b) Axial gradiometer (c) Planar gradiometer

Figure 2.5: Examples of pick-up coil shapes. From [29].

2.8 Noise Rejection with Synthetic, Higher Order Gradiometers

Environmental magnetic noise is a large problem when measuring the fields caused by brain activity, because these fields are much smaller than the everywhere present fields generated by sources in the environment for example by the electrical power system. One mean to reduce the magnetic noise is putting up the MEG machine in a magnetically shielded room which strongly attenuates the fields of outside sources. Nevertheless there still are magnetic fields penetrating the shielding and in addition there are the magnetic fields generated by the human body. The strength of the magnetic field the heart generates, for example, is more than hundred times larger than the typical magnetic field caused by brain activity. So another thing one does to only measure the signal

generated by sources inside the brain is not to measure the absolute magnetic flux using magnetometers, but the spatial gradient of the flux using gradiometers.

Using magnetometers a distant, but strong source, like for example the human heart, would still significantly contribute to the measured signal, whereas using gradiometers the contribution of the distant, but strong source would be much less. The amplitude of the signal which is caused by a close, but weak source, like the brain activity, is not attenuated when measuring with gradiometers instead of magnetometers.

This concept of noise rejection by means of measuring the spatial gradient of the magnetic field can be extended to synthetic gradiometers[28, 29]. To cancel the noise with higher order, synthetic gradiometers the field is not only measured at the primary, measurement sensors, but also at a number of reference sensors. Synthetic gradiometers can now be composed of one measurement sensor and a number of reference sensors by subtracting a linear combination of the signals measured by the reference sensors from the signal measured by the measurement sensor.

$$\Phi_i^{*,\,\mathrm{meas}} = \Phi_i^{\mathrm{meas}} - \sum_j C_{ij} \cdot \Phi_j^{\mathrm{ref}} \tag{2.64}$$

Here $\mathbf{\Phi}^{*,\,\mathrm{meas}}$ and $\mathbf{\Phi}^{\mathrm{meas}}$ are the signals of the measurement sensors with respectively without applied noise rejection and $\mathbf{\Phi}^{\mathrm{ref}}$ are the signals measured at the reference sensors. $\mathbf{C}$ is the coefficient matrix. With the definitions

$$\mathbf{B} = (\mathbf{I}\,|\mathbf{C}) \quad \text{and} \quad \mathbf{\Phi}^{\mathrm{meas,\,ref}} = \begin{pmatrix} \mathbf{\Phi}^{\mathrm{meas}} \\ \mathbf{\Phi}^{\mathrm{ref}} \end{pmatrix} \tag{2.65}$$

equation (2.64) can be rewritten as in equation (2.66).

$$\mathbf{\Phi}^{\mathrm{meas}} = \mathbf{B} \cdot \mathbf{\Phi}^{\mathrm{meas,\,ref}} \tag{2.66}$$

The coefficients $\mathbf{C}$ for the linear combination of the reference signals are determined in such a way, that the synthetic gradiometer mimics a hardware gradiometer of the same order. How this is done shall be shown for a first order synthetic gradiometer following [28, 29]. The signal for a first order synthetic gradiometer can be composed of the signal of one primary measurement magnetometer and one reference vector magnetometer. The vector magnetometer consists of three magnetometers whose orientations are orthogonal to each other.

When applying a magnetic field $\mathbf{B}$ the signal of the measurement magnetometer is

$$\Phi^{\mathrm{meas}} = \alpha_{\mathrm{p}}\, \mathbf{B} \cdot \mathbf{p}^{\mathrm{meas}} \ ,$$

where α_p is the gain of the primary magnetometer and $\mathbf{p}^{\mathrm{meas}}$ is its orientation. The signal of the reference vector magnetometer can be written as a vector $\mathbf{\Phi}^{\mathrm{ref}}$ with components

$$\Phi_k^{\mathrm{ref}} = \alpha_{\mathrm{ref}}\, B_k \ .$$

Here α_r is the gain of the vector magnetometers and

$$B_k = \mathbf{p}^{\mathrm{ref,\,k}} \cdot \mathbf{B}$$

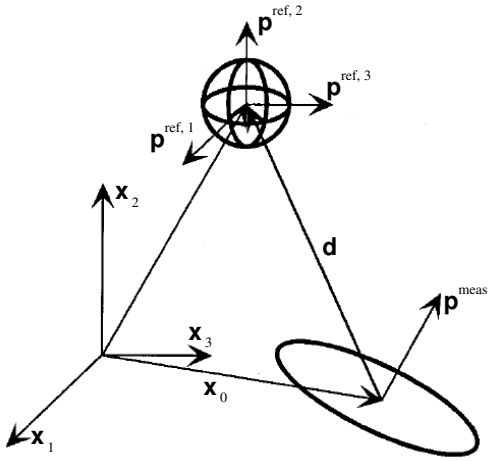

Figure 2.6: Measurement and vector reference magnetometer. Figure from [29].

is the component of the magnetic flux density parallel to the orientation of the k-th magnetometer of the reference vector magnetometer. Now the magnetic flux density $\mathbf{B}$ is approximated by the first terms of a Taylor series around the center of the measurement sensor, $\mathbf{x}_0$.

$$\mathbf{B}\left(\mathbf{x}\right) = \mathbf{B}_0 + \mathbf{G}_0\ \left(\mathbf{x} - \mathbf{x}_0\right) + O\left(x^2\right) \tag{2.67}$$

$\mathbf{G}_0 = \nabla \mathbf{B}\left(\mathbf{x}\right)|_{\mathbf{x}=\mathbf{x}_0}$ denotes the first gradient of the magnetic flux density. With the first two terms of the Taylor expansion and using equation (2.64) the signal of the synthetic first order gradiometer can be written as in equation (2.68).

$$\Phi^{*,\,\mathrm{meas}} = \alpha_\mathrm{p}\,\mathbf{p}^\mathrm{meas} \cdot \mathbf{B}_0 + \sum_k C_{1\,k}\,\alpha_\mathrm{ref}\,\mathbf{p}^{\mathrm{ref,\,k}}\left(\mathbf{B}_0 + G_0 \cdot \mathbf{d}\right) \tag{2.68}$$

The vector pointing from the centre of the measurement magnetometer to the centre of the reference vector magnetometer is called the baseline $\mathbf{d}$.

The coefficients $C_{1\,k}$ are chosen in such a way that the synthetic gradiometer mimics a real gradiometer. By definition a n-th order gradiometer cancels out the contributions from gradients of the magnetic flux densities that are of order $(n-1)$ or below. So in the case of a homogeneous field the signal of the first order synthetic gradiometer has to be zero.

$$\alpha_\mathrm{p}\mathbf{p}^\mathrm{meas} \cdot \mathbf{B}_0 = -\sum_k C_{1\,k}\alpha_\mathrm{ref}\mathbf{p}^{\mathrm{ref,\,k}} \cdot \mathbf{B}_0 \tag{2.69}$$

This equation can be solved for the coefficients $C_{1\,k}$ using the fact, that the orientations of the reference magnetometers are orthogonal to each other. Equation (2.70) shows the solution for the coefficients of a first order synthetic gradiometer.

$$C_{1\,k} = -\frac{\alpha_\mathrm{p}}{\alpha_\mathrm{ref}}\ \left(\mathbf{p}^{\mathrm{ref,\,k}} \cdot \mathbf{p}^\mathrm{meas}\right) \tag{2.70}$$

From this equation it can be seen that the coefficients for first order synthetic gradiometers are the orientations of the reference magnetometers projected onto the orientations of the measurement magnetometer and normalized to the latter's gain. The coefficients for higher order synthetic gradiometers can be derived in a similar way.

Although the synthetic gradiometers mainly cancel out lower gradients of the magnetic flux density, which are caused by distant, strong sources, that is environmental magnetic noise, it can also influence a signal produced by brain activity. So when an inverse method is to be applied to data, to which the discussed noise rejection was applied, the noise rejection technique also has to be modelled for the forward problem. That is one has to simulate the magnetic flux not only at the measurement sensors but also at the reference sensors and then calculate the signal of the higher order synthetic gradiometers as in equation (2.64). The noise rejection with synthetic higher order gradiometers for the FEM forward problem was therefore implemented into the software *NeuroFEM* as a part of this diploma thesis. This implementation was used for data from the phantom study (see chapter (4)) and for the source reconstruction on the MEG data of the SEP/SEF experiment in chapter (6).

2.9 Inverse Methods

The reconstruction of the current density distribution from a measured EEG or MEG is called the inverse problem. There are a many algorithms for the solution of the inverse problem. In this thesis two simple algorithms were used for the source reconstruction. Those will be explained briefly in this section.

2.9.1 Moving Dipole Fit

The first method to reconstruct the underlying sources of a EEG or MEG is the moving dipole fit[15]. For the moving dipole fit it is assumed, that the current density can be described by a number of discrete current dipoles. The number of dipoles, p, has to be chosen using a priori knowledge. The whole current density distribution can now be described with the locations, orientations and magnitudes of the current dipoles. For a moving dipole fit first the non-linear location parameters $\mathbf{q}$ are chosen. Then the linear parameters describing the orientation and magnitude that minimize the difference between the simulated and measured data are determined. This procedure is repeated until a stop criterion is met.

First it will be explained how to determine the linear parameters for given non-linear parameters $\mathbf{q}$. The electric potential respectively the magnetic flux is simulated for 3 orthogonal dipoles of unit strength at each dipole location. The simulated data for the orthogonal dipoles form the columns of the specific $3r \times s$ lead field matrix, $\mathbf{L}_q$, for the location parameters $\mathbf{q}$. s is here the number of sensors. The lead field matrix can now be used to calculate the simulated data for dipoles with arbitrary orientations and magnitudes.

$$\mathbf{u}^{\text{sim}} = \mathbf{L}_q \, \mathbf{J}_q \tag{2.71}$$

$\mathbf{u}^{\text{sim}}$ is here the simulated data and $\mathbf{J}_q$ is a vector containing the orientation and magnitude parameters of the p dipoles. These parameters are optimized linearly to minimize the difference between the simulated and the measured data of the EEG respectively the MEG.

$$H(\mathbf{q}) = \|\mathbf{L}_q \mathbf{J}_q - \mathbf{u}^{\text{meas}}\| \stackrel{!}{=} \min \tag{2.72}$$

$H(\mathbf{q})$ is the goal function to be minimized. From equation (2.72) the linear parameters $\mathbf{J}_q$ that minimize $H(\mathbf{q})$ can be found using for example a singular value decomposition.

The non-linear location parameters of the current dipoles are in the studies for this thesis chosen by a downhill simplex optimizer[16]. To find the global minimum of the cost function $H(\mathbf{q})$ using a simplex optimizer, the function is not only evaluated at a single point, or vertex, $\mathbf{q}$ in the parameter space, but at a set $\mathbf{q}_i = (q_0, \ldots, q_i + \Delta q, \ldots, q_n)$ of vertices. These vertices are forming a simplex. The simplex moves through the parameter space by reflection of the vertex with the highest goal function value. Depending on certain criteria the simplex can also expand to avoid local minima and when reaching the global minimum it contracts itself around this global minimum. Because of the simplex ability to contract and expand it is reliable and often able to find the global minimum.

The moving dipole fit is stopped when one of the stop criteria is met. One stop criterion is for example the absolute goal function value. If it exceeds a certain value the moving dipole fit assumes it has found a reasonable dipole configuration and stops.

2.9.2 Goal Function Scan

The second inverse method used in this thesis is the goal function scan. It can only be used when assuming that the current density distribution can be described by a single current dipole. As input for the goal function scan a source grid is provided. The vertices, $\mathbf{q}_i$, of the grid are possible locations for a current dipole. Now for every vertex of the source grid the lead field L_q is calculated and the minimum goal function value $H(\mathbf{q})$ as defined in equation (2.72) is determined. The output of a goal function scan is then a goal function value for each of the grid nodes. When reconstructing a dipolar source the node with the minimum goal function value can be taken as the reconstructed source location. Often a goal function scan does not deliver the goal function values directly but values that describe how much of the measured data a dipole at the vertices describes as in equation (2.73). The best value for H^* is 1.

$$H^*(\mathbf{q}_i) = 1 - \frac{H(\mathbf{q}_i)}{\|\mathbf{u}^{\text{meas}}\|} \tag{2.73}$$

3 Validation of the Finite Element Method Based Forward Computations in Multilayer Sphere Models

The first step for the validation of the forward computations using the finite element method is to compare the FEM forward solutions to a known exact reference solution and determine in this way how accurate FEM can simulate the electric potential and the magnetic flux. So in this chapter FEM is used to compute the electric potential and the magnetic flux for dipoles in multilayer spherical volume conductors, for which exact reference solutions exist. For the EEG the accuracy of FEM is studied for multilayer sphere models with varying complexity. For the MEG the focus is on the accuracy of the FEM simulation of the secondary magnetic flux and its contribution to the total magnetic flux. Additionally the accuracy of the finite element method will be compared to the accuracy of a boundary element solution.

3.1 Methods

In this section the methods for the EEG and MEG studies in the multilayer sphere models shall be presented. This includes the description of the studied volume conductors, the used sensor configurations, the generation of the FEM and BEM meshes and the error measures used in this work.

3.1.1 Multilayer Sphere Models

Volume Conductors for the EEG Studies

In the EEG studies spherical volume conductors with varying complexity were used. The most simple volume conductor used is the three layer sphere model with isotropic skull. Three compartment volume conductors are commonly used to model the head. Radii and conductivities of the layers can be found in table (3.1).

	scalp	**skull**	**brain**
radius	92.0 mm	86.0 mm	80.0 mm
conductivity	0.33 S/m	0.0042 S/m	0.33 S/m

Table 3.1: The three layer sphere model with isotropic skull used in the EEG studies.

When modelling the head as a three compartment volume conductor the tissues brain and cerebro spinal fluid (CSF) are merged into one compartment with one conductivity

value. As measurements showed that the CSF is much more conductive than the brain often four layer volume conductors with an additional CSF compartment are used to model the head. For this reason in the EEG studies a four layer sphere model with isotropic skull is used which incorporates the CSF as a separate layer. The radii and conductivities of the model can be seen from table (3.2).

	scalp	**skull**	**CSF**	**brain**
radius	92.0 mm	86.0 mm	80.0 mm	78.0 mm
conductivity	0.33 S/m	0.0042 S/m	1.79 S/m	0.33 S/m

Table 3.2: The four layer sphere model with isotropic skull used in the EEG studies.

Anatomically the skull consists of two layers of compact bone, the compacta, with a fatty bone layer, the spongiosum, in between. The conductivity of the spongiosa was measured to be much higher than the conductivity of the bone layers[2]. When modelling the skull as one compartment as it is usually done this results in an anisotropic conductivity of the skull where the conductivity in tangential directions is ten times higher than the conductivity in radial direction. That is the ratio of radial to tangential conductivity is $1 : 10$ [1]. For this reason the accuracy of the FEM simulation of the EEG was also studied for a four layer sphere model with $1 : 10$ anisotropic skull.

To fix the radial and tangential conductivity of the skull in addition to determine a ratio of radial to tangential conductivity an assumption on the relation to the isotropic conductivity value has to be made. Four possible ways to fix the anisotropic conductivities are shown in table (3.3). The first possibility is to only vary the tangential

	σ_{rad} $[S/m]$	σ_{tang} $[S/m]$
Tangential $\sigma_{\text{rad}} = \sigma_{\text{iso}}$	0.0042	0.042
Wang's Constraint $\sigma_{\text{rad}} \cdot \sigma_{\text{tang}} = \sigma_{\text{iso}}^2$	0.00133	0.01328
Volume Constraint $\sigma_{\text{rad}} \cdot \sigma_{\text{tang}}^2 = \sigma_{\text{iso}}^3$	0.00090	0.00905
Radial $\sigma_{\text{tang}} = \sigma_{\text{iso}}$	0.00042	0.0042

Table 3.3: Additional assumptions and radial and tangential conductivity values for the four possible ways of fixing the radial and tangential conductivity of the skull.

conductivity and assign the isotropic conductivity value to the radial conductivity of the skull. In the second possibility, following [32], the product of radial and tangential conductivity is assumed to be equal to the square of the isotropic conductivity value. The

third assumption means that the volume of the conductivity tensors in the anisotropic case is equal to the volume of the tensor in the isotropic case. Varying only the radial conductivity and keeping the tangential conductivity fixed to the isotropic value is the last way to fix the anisotropic conductivities.

The simulated electric potentials for one dipole and all four methods showed that the effect of the anisotropy is rising according to the position in table (3.3) where the effect for changing only the tangential conductivity is lowest and the effect for changing only the radial conductivity is highest. Therefore in the here used sphere model the radial and tangential conductivities of the skull are set by varying only the tangential conductivity. Radii and conductivities of the four layer sphere model with anisotropic skull can be seen from table (3.4).

	scalp	**skull**		**CSF**	**brain**
radius	92.0 mm	86.0 mm		80.0 mm	78.0 mm
conductivity		radial	tangential		
	0.33 S/m	0.0042 S/m	0.042 S/m	1.79 S/m	0.33 S/m

Table 3.4: The four layer sphere model with anisotropic skull used in the EEG studies.

Volume Conductor for the MEG Studies

As, due to symmetry effects in the sphere, the magnetic fields outside of the head are not depending on the radii and the conductivities of a multilayer sphere model [21], only one volume conductor model is used for the MEG studies. The accuracy of the FEM for the MEG is studied only in a one layer sphere model which radius and conductivity can be found in table (3.5).

	brain
radius	80.0 mm
conductivity	0.33 S/m

Table 3.5: Radius and conductivity of the one layer sphere model used in the MEG studies.

3.1.2 The Sensor Configurations

For the EEG studies the electric potential was computed for 134 electrodes which were distributed in a most regular way on the surface of the model. Figure (3.1(a)) illustrates the electrode sensor configuration.

For the MEG studies the magnetic flux was simulated at 3 sets of 258 magnetometers each. The centres of the sensors were distributed on a sphere with the radius 110 mm in a most regular way. For the first set of sensors the magnetometers were radially orientated relative to the sphere model. The magnetometers of the other two sets were orientated

tangentially. The radial and one of the tangential MEG sensor configurations are shown in figures (3.1(b)) resp. (3.1(c)).

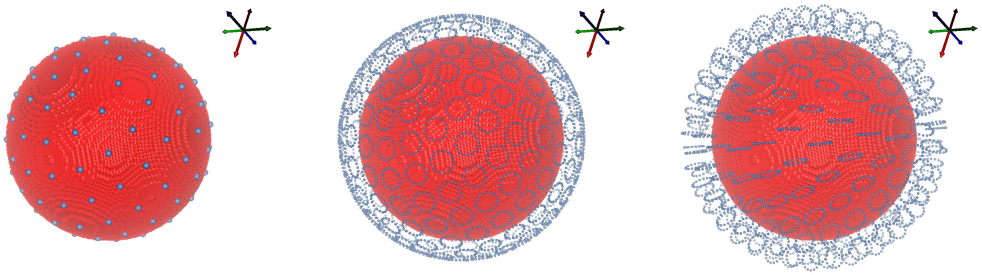

(a) The used electrode configuration.

(b) The used radial magnetometer configuration.

(c) One of the used tangential magnetometer configurations.

Figure 3.1: EEG and MEG sensor configurations used for the multilayer sphere studies. The magnetometers in the MEG configurations are represented by the FEM nodes with which the sensor coils are modeled.

3.1.3 Generation of the FEM and BEM Meshes

Generation of the FEM Meshes

When the electric potential or the magnetic flux is to be computed using the finite element method a FEM mesh of the volume conductor has to be built. This FEM mesh represents the discretised geometry and conductivity of the volume conductor. The geometry of the volume conductor can be discretised using different element types. Here tetrahedra and regular and nodeshifted hexahedra are used.

The first step for the generation of both, the tetrahedra and hexahedra, FEM meshes of the multilayer sphere models is to create a synthetic magneto resonance image of the sphere. In this MR image the different compartments are represented by voxels with a different grey value.

For the creation of the tetrahedra meshes the MRI is then read into the commercial software *CURRY* [9]. CURRY then segments the different compartments of the volume conductor by their grey values in the MR image. Tetrahedra meshes with elements of varying edge lenth were created as described in section (2.6.1). Table (3.6) lists the used tetrahedra FEM meshes.

The regular and nodeshifted hexahedra meshes are generated using the software *Vgrid*[27] as described in section (2.6.1). Hexahedra meshes with varying element width were created. Details on the regular and nodeshifted cube meshes can be seen from table (3.6).

The geometry of the FEM meshes used for the simulations in the four layer, isotropic and anisotropic volume conductor is identical to those used for the simulations in the three layer, isotropic volume conductor. The FEM meshes of the three layer sphere models were derived from the FEM meshes of the four layer, isotropic sphere models

by simply assigning all CSF elements the conductivity of brain tissue. Furthermore the FEM meshes for the four layer anisotropic volume conductor were derived from the meshes for the isotropic four layer sphere by assigning all skull elements an anisotropic conductivity. Figures (3.1.3) to (3.1.3) show cuts through the tetrahedra, regular hexahedra and nodeshifted hexahedra FEM meshes.

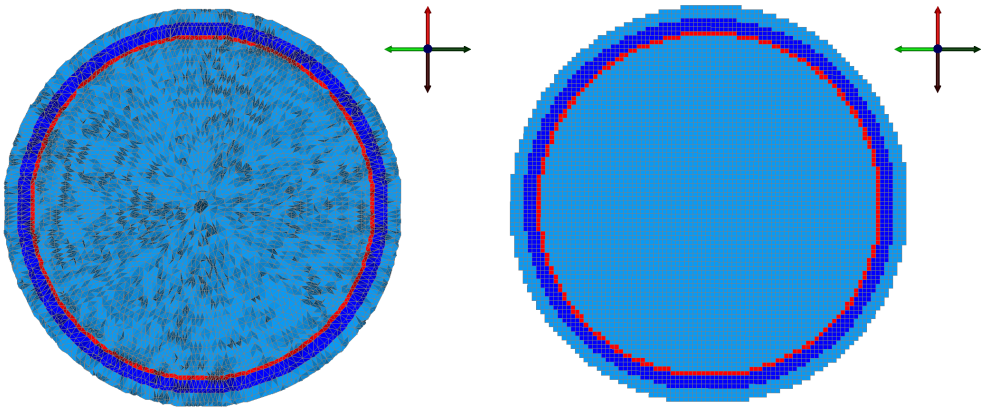

(a) Tetrahedra mesh.

(b) Regular hexahedra mesh.

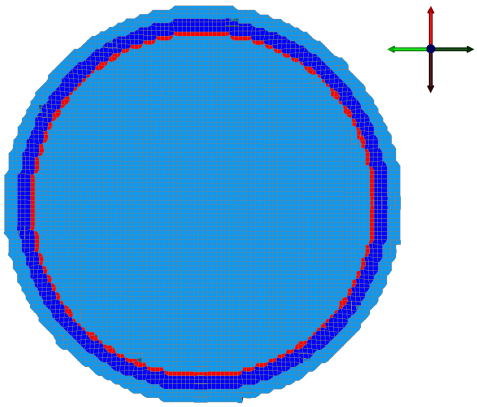

(c) Nodeshifted hexahedra mesh.

For the four layer, anisotropic sphere an additional FEM mesh was used (table (3.6)). This FEM mesh was built using the constrained Delaunay tetrahedralisation employing the software tool *TetGen*[24]. It has got high quality, that is very regular, tetrahedra and local mesh refinements in the areas where it is important for a good accuracy of the FEM solution. A small region of a cut through the tetrahedra meshes tet229k_4layer_aniso and tet719k_4layer_aniso can be seen in figures (3.2(d)) resp. (3.2(e)).

For the MEG studies only the one layer sphere model had to be meshed. Furthermore for the MEG the influence of element width on the accuracy is not studied. Therefore only tetrahedra and hexahedra meshes with an average 2 mm edge length were created. The FEM meshes used for the MEG studies can also be found in table (3.6).

	element type	width	# nodes	# elements	nodeshift
EEG					
3 layer, isotropic					
tet229k_3layer_iso	tetrahedra	2.0 mm	228993	1378159	n.a.
tet174k_3layer_iso	tetrahedra	3.0 mm	173533	1045555	n.a.
tet70k_3layer_iso	tetrahedra	4.0 mm	69582	418816	n.a.
cube426k_3layer_iso	hexahedra, regular	2.0 mm	425631	418816	no
cube130k_3layer_iso	hexahedra, regular	3.0 mm	129781	120741	no
cube56k_3layer_iso	hexahedra, regular	4.0 mm	56043	50918	no
cubens426k_3layer_iso	hexahedra, nodeshifted	2.0 mm	425631	418816	yes
cubens130k_3layer_iso	hexahedra, nodeshifted	3.0 mm	129781	120741	yes
cubens56k_3layer_iso	hexahedra, nodeshifted	4.0 mm	56043	50918	yes
4 layer, isotropic					
tet229k_4layer_iso	tetrahedra	2.0 mm	228993	1378159	n.a.
cubens426k_4layer_iso	hexahedra, regular	2.0 mm	425631	418816	no
cubens426k_4layer_iso	hexahedra, nodeshifted	2.0 mm	425631	418816	yes
4 layer, anisotropic					
tet229k_4layer_aniso	tetrahedra	2.0 mm	228993	1378159	n.a.
cube426k_4layer_aniso	hexahedra, regular	2.0 mm	425631	418816	no
cubens426k_4layer_aniso	hexahedra, nodeshifted	2.0 mm	425631	418816	yes
tet716k_4layer_aniso	tetrahedra	n.a.	715721	4504002	n.a.
MEG					
1 layer, isotropic					
tet649k_1layer_iso	tetrahedra	2.0 mm	648523	4104089	n.a.
cube282k_1layer_iso	hexahdra, regular	2.0 mm	281591	266389	no
cubens282k_1layer_iso	hexahdra, nodeshifted	2.0 mm	281591	266389	yes

Table 3.6: The FEM meshes used for the EEG and MEG studies.

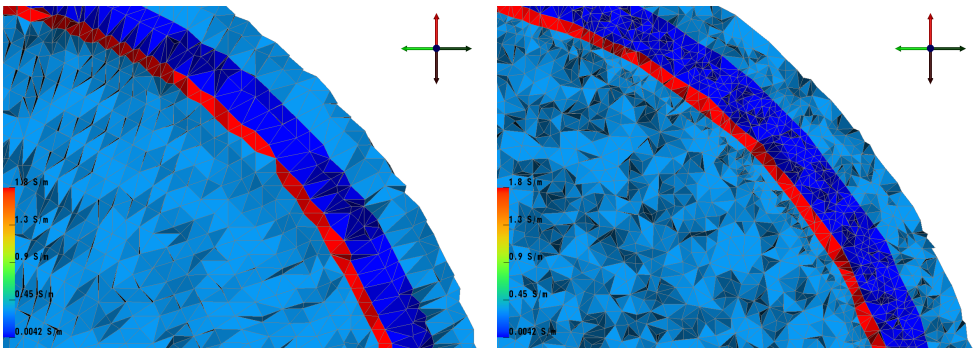

(d) tet229k_4layer_aniso (e) tet716k_4layer_aniso

Figure 3.2: Small region of the cut through the tetrahedra FEM meshes for the four layer, anisotropic sphere model.

Generation of the BEM meshes

The simulation of the electric potential or magnetic flux using the boundary element method also needs a mesh representing the interfaces between the compartments with constant conductivity.

For the EEG studies in this section we generated BEM meshes of a three layer spherical volume conductor with varying element size and therefore a varying number of elements and nodes. The mesh generation was done in CURRY in a very similar way as the generation of the tetrahedra FEM meshes was done in CURRY. A synthetic MR image of the three layer sphere was segmented. The interfaces were then meshed with triangles as described in section (2.6.2). The generated BEM meshes with varying triangle size are listed in table (3.7). For the studies in the MEG one layer sphere model only one BEM mesh was used (see table (3.7)).

	width				
	scalp	**outer skull**	**inner skull**	**# nodes**	**# elements**
EEG					
3 layer, isotropic					
fine3700_3layer_iso	10.0 mm	9.5 mm	8.0 mm	3727	7462
standard2600_3layer_iso	12.5 mm	11.5 mm	9.5 mm	2589	5166
coarse2000_3layer_iso	14.5 mm	13.5 mm	10.5 mm	2015	4018
MEG					
1 layer, isotropic					
fine1400_1layer_iso	n.a.	n.a.	8.0 mm	1374	2744

Table 3.7: The used BEM meshes.

3.1.4 Error Measures

To quantify the errors between the numerical solutions, Phi^{num}, and the (quasi-)analytical reference solutions, Φ^{ref}, three different error measures were used. In the following equations the norm is defined as $\|x\|_2 = \sqrt{\sum_{i=1}^{n} x_i^2}$, where n is the number of sensors.

The first error measure is the *relative error* (RE).

$$RE = \frac{\left\|\Phi^{\text{ref}} - \Phi^{\text{num}}\right\|_2}{\left\|\Phi^{\text{ref}}\right\|_2} \tag{3.1}$$

The RE is always positive and the best value for the RE is 0. The RE is not bounded above.

A simple scaling of the electric potential effects the RE in the same way as a difference in the topography of the electric potential or the magnetic flux does. Therefore Meijs proposed in [14] two new error measures.

The first error measure he introduced is the *relative difference measure* (RDM).

$$RDM = \left\| \frac{\Phi^{\text{ref}}}{\left\|\Phi^{\text{ref}}\right\|_2} - \frac{\Phi^{\text{num}}}{\left\|\Phi^{\text{num}}\right\|_2} \right\|_2 \tag{3.2}$$

It indicates differences in the topograpy of the potential respectively the flux and it is not affected by a mere scaling of the values with a constant value. The RDM is always positive an its best value is 0. The maximum value for the RDM is 2.

Finally there is the *magnification error* (MAG).

$$MAG = \frac{\left\|\Phi^{\text{num}}\right\|_2}{\left\|\Phi^{\text{ref}}\right\|_2} \tag{3.3}$$

It indicates a constant scaling between the reference and the numerical solutions. The best value for the MAG is 1. It is not bounded above.

3.2 Results and Discussion

This section presents the results of the studies in the multilayer sphere models. First the accuracy of the FEM solution for the EEG for spherical volume conductors of varying complexity is investigated and compared to the accuracy of a BEM solution with comparable computational complexity. Then the accuracy of the FEM solution for the MEG is studied. Furthermore the contribution of the primary current and the volume currents to the total magnetic flux will be discussed for synthetic and a realistic sensor configurations.

3.2.1 Results of the EEG Studies

The first volume conductor used in this work is the most simple one used to model the human head: the three layer sphere model with isotropic conductivities. (See table (3.1)

for details on the volume conductor.) The electric potential at the 134 surface electrodes in the three layer model was calculated for radial and tangential dipoles at positions from the centre of the spheres in 1 mm steps along the z-axis until 4 mm below the interface between the brain and skull compartment. As realistic sources in the human brain are situated in the middle of the approx. 4 mm thick cortex layer and as the thickness of the CSF layer can be estimated to be 2 mm it is reasonable to assume that realistic sources do not come closer to the inner skull than 4 mm. The eccentricity of the dipoles was defined to be 1 for the most superior dipole.

To generate a reference solution the electric potential for these dipoles was calculated using de Munck's formula described in section (2.3.1). The electric potential for the set of dipoles was then calculated using the finite element method and the meshes for the three layer, isotropic volume conductor described in table (3.6). The current dipole was modelled using Venant's approach. Furthermore the potential was calculated employing the boundary element method using the meshes listed in table (3.7). To quantify the errors of the numerical methods the RDM and the MAG between the numerical and the analytical solutions is calculated.

Figures (3.3), (3.4) and (3.5) show the RDM and MAG against the dipole eccentricity of the FEM solutions for tetrahedra, regular cube and nodeshifted cube meshes respectively with different element sizes.

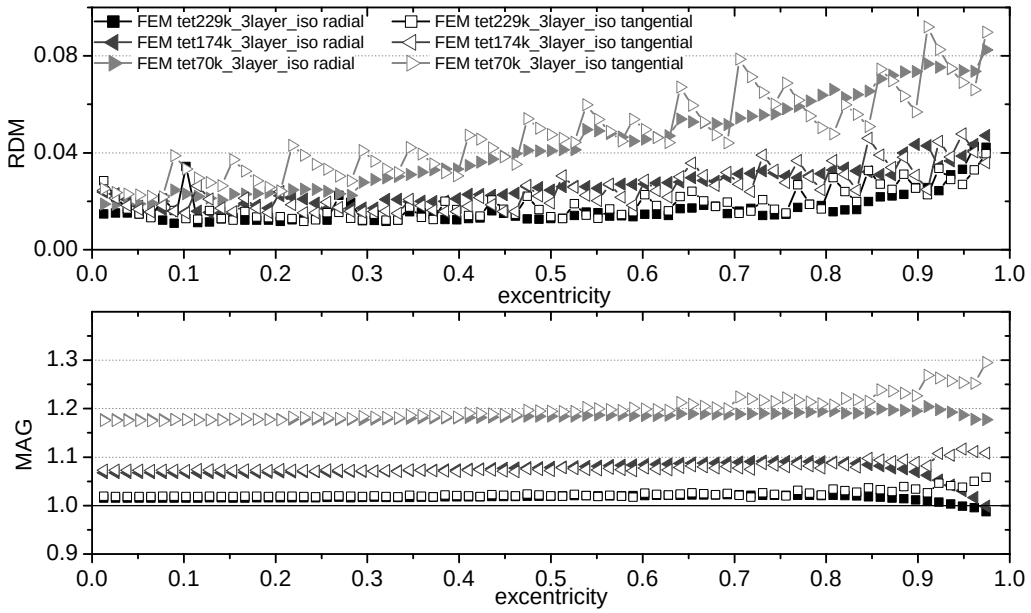

Figure 3.3: RDM and MAG for the FEM solutions in tetrahedra meshes of the three layer, isotropic sphere model with varying element size.

In figure (3.6) the RDM and MAG for the BEM solution in meshes with varying element size is presented.

The error curves for the FEM solutions in meshes with varying element size show that

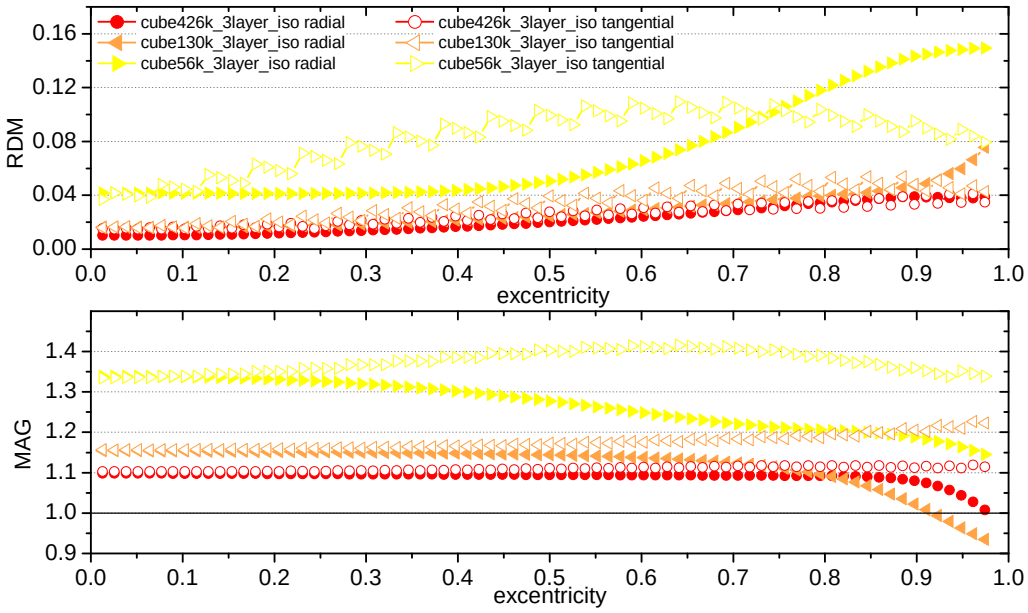

Figure 3.4: RDM and MAG for the FEM solutions in regular cube meshes of the three layer, isotropic sphere model with varying element size.

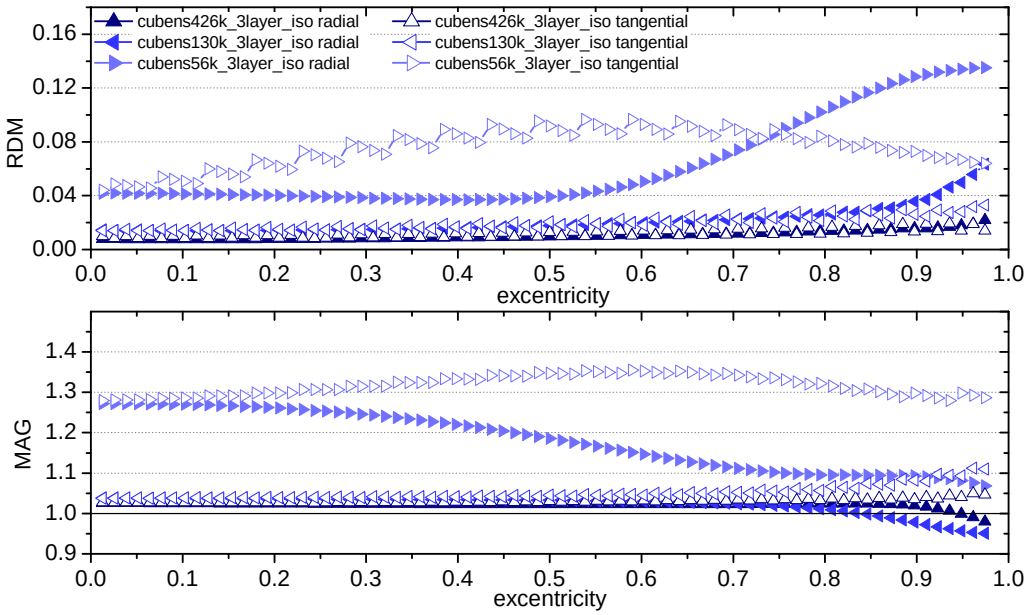

Figure 3.5: RDM and MAG for the FEM solutions in nodeshifted cube meshes of the three layer, isotropic sphere model with varying element size.

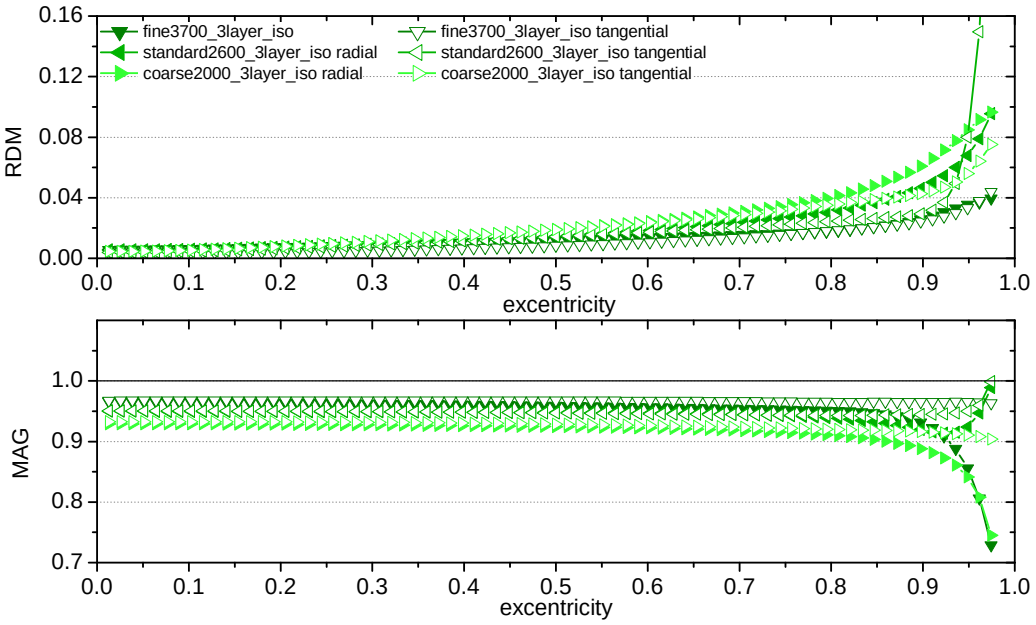

Figure 3.6: RDM and MAG for the BEM solutions in meshes of the three layer, isotropic sphere with varying element size.

the FEM solution is converging towards the analytical solution. The errors decrease for all element types when decreasing the element width throughout the whole mesh, that is when globally refining the mesh. Convergence towards the analytical solution is also found for the BEM solutions in meshes with decreasing element size.

In figure (3.7) the accuracy of the FEM solutions for the different element types is compared to the accuracy of BEM for a standard BEM mesh. The computational effort needed for the BEM solution is comparable to the computational effort for the FEM solutions in the meshes with 2 mm element size.

The RDM for the FEM solutions in the 2 mm meshes is below 0.04 and the MAG lies between 0.95 and 1.15 for the whole range of dipole eccentricities. It can be observed, that the RDM for all meshes increases for increasing eccentricity. In addition the plots show that oscillations are superimposed on the error curves, especially for tangential dipoles. In the error curves a decrease of the MAG for high eccentricities can be noticed for radial dipoles, but not for tangential ones. Comparing the element types the FEM solution in the nodeshifted hexahedra meshes is most accurate, followed by the solution in the tetrahedra mesh, which is only for high eccentricities less accurate. The regular hexahedra mesh delivers the worst results.

The RDM for the BEM solution is everywhere below 0.05 and the MAG lies between 0.7 and 1.0. For high eccentricities the RDM strongly increases and the MAG decreases away from the ideal value of the MAG.

When comparing the accuracy of the potentials calculated using BEM and FEM one can find that the FEM solution for the three layer, isotropic sphere model is, for dipoles

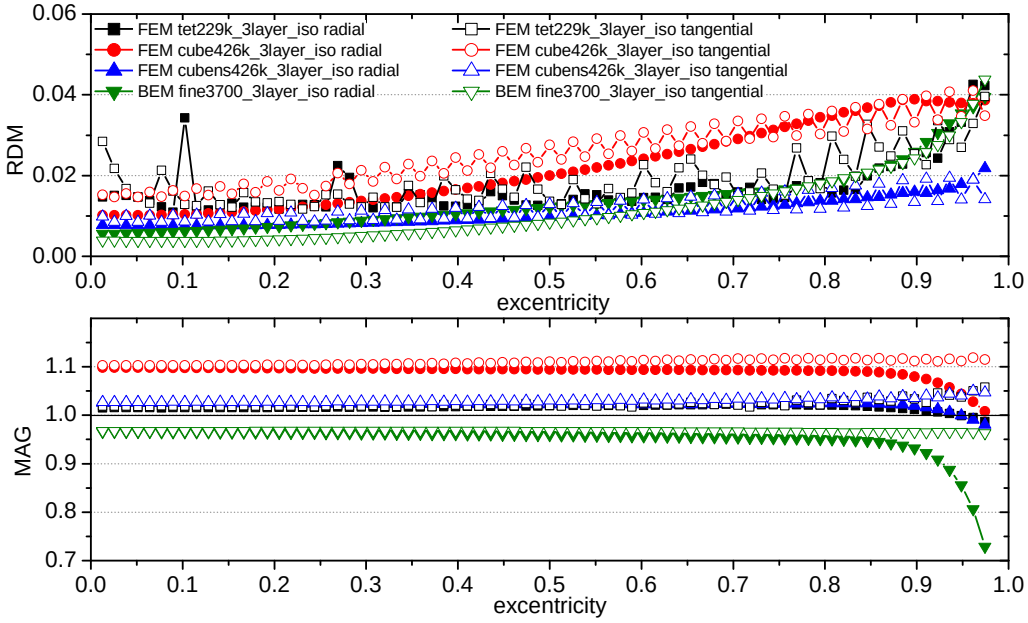

Figure 3.7: RDM and MAG for the BEM solution and for the FEM solutions for different element types in the three layer, isotropic sphere model.

at realistic eccentricities $\gtrapprox 0.7$, more accurate than the BEM solution, when nodeshifted hexahedra meshes are used. But BEM performs better, when compared to FEM in the regular hexahedra mesh.

As discussed above the three layer sphere model reflects the head compartments scalp, skull and brain, but it ignores the highly conducting CSF layer between the skull and the brain. Therefore very often the four layer sphere model is used to model the human head. Details about the radii and the conductivities of the sphere shells can be found in table (3.2). The reference solution was generated using the (quasi-)analytical solution for a four layer spherical volume conductor. The electric potential was simulated for the same set of dipoles as for the three layer sphere model. The FEM meshes of the four layer isotropic sphere model can be found in table (3.6). As before the current dipole for the finite element method was modelled using Venant's approach.

The BEM calculations were performed only for meshes with three compartments. In general it is possible to model a four layer volume conductor in BEM, but for realistic models this cannot be done with reasonable computational effort. This is because the surface of the cortex with its deep sulci has to be meshed with very fine triangles. That would strongly increase the number of nodes and therefore the computation time needed.

To compare the accuracy of the BEM and the FEM solution for the different element types RDM and MAG error curves for the numerical solutions are presented in figures (3.8) for radial dipoles and (3.9) for tangential dipoles. The figures furthermore show the error between the analytical solution in the three layer sphere and the analytical solution in the four layer sphere. This curve indicates the error which is caused by ignoring the

CSF layer.

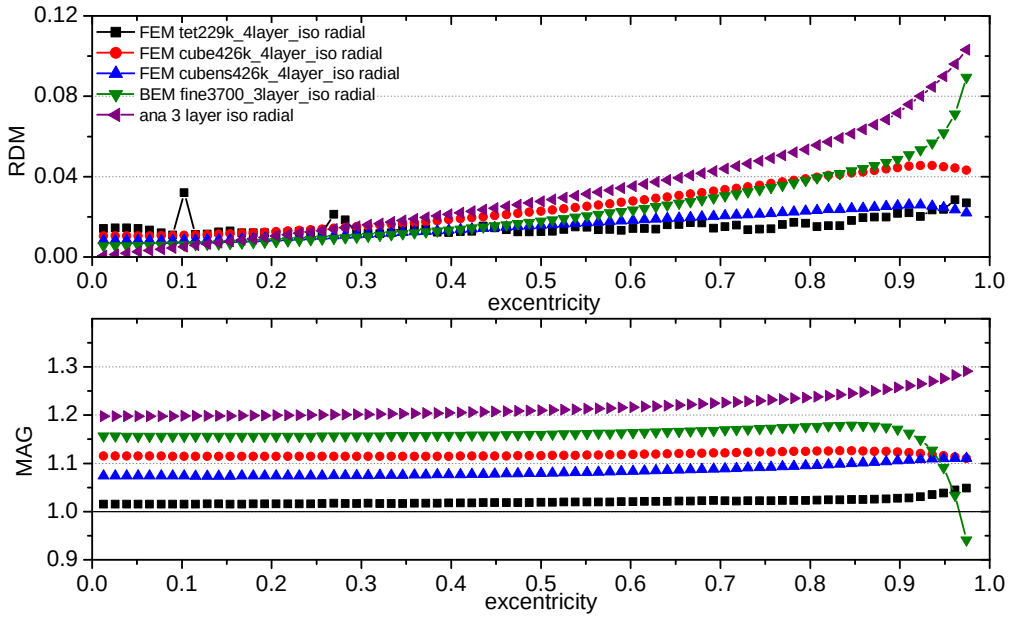

Figure 3.8: RDM and MAG for the BEM solution in the three layer, isotropic sphere model and for the FEM solutions for different element types in the four layer, isotropic sphere model. Radial Dipoles.

The RDM for the FEM solutions for the four layer, isotropic sphere model is everywhere below 0.05 and the MAG lies between 1.0 and 1.15. The RDMs are again increasing for higher eccentricities. Comparing the accuracies for the different element types it can be observed, that the regular hexahedra as in the three layer sphere are least accurate. Using nodeshifted hexahedra meshes yields slightly larger errors for the four layer sphere model than for the three layer sphere model. So in the four layer sphere model the tetrahedra mesh performs best.

The RDM for the BEM solution in a three layer sphere model reaches 0.09 for radial dipoles and 0.06 for tangential dipoles. One can observe that the RDM for the BEM solution is nearly everywhere below the error caused by ignoring the CSF layer.

Comparing BEM and FEM one can see that the errors of the FEM solution in the nodeshifted hexahedra and the tetrahedra mesh are, for realistic dipole eccentricities, less than the errors for the BEM solution. For the FEM solution in the regular hexahedra mesh this is only true for eccentricities higher than 0.9.

In section (3.1.1) it was already mentioned that the conductivity of the skull is anisotropic. This anisotropy is taken into account for the four layer, anisotropic sphere model described in detail in table (3.2). The reference solution was created using de Munck's formula, which allows radial to tangential anisotropy in each of the layers. In the FEM solution the anisotropy of the skull was taken into account using anisotropic FEM meshes. Venant's approach was used to model the current dipole in FEM. As BEM is only able to handle one isotropic conductivity value per compartment the BEM

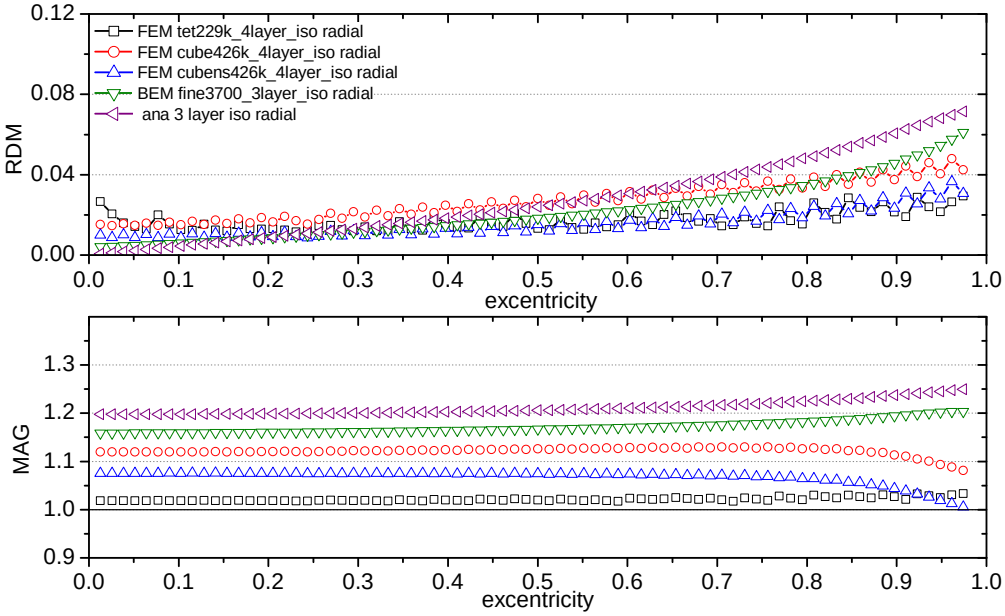

Figure 3.9: RDM and MAG for the BEM solution in the three layer, isotropic sphere model and for the FEM solutions for different element types in the four layer, isotropic sphere model. Tangential Dipoles.

solutions were calculated for the three layer, isotropic head models already used above.

Figures (3.10) and (3.11) show the error curves for the FEM solutions for different element types and the BEM solution for radial resp. tangential dipoles. Additionally the RDMs and MAGs between the analytical solution in a three layer, isotropic sphere and the quasi-analytical solution in a four layer, anisotropic sphere are shown. This last curve indicates the effect of neglecting the CSF layer and the anisotropy of the skull.

The RDM errors of the FEM solutions are everywhere less than 0.09 and the MAG lies between 1.0 and 1.3. Compared to the errors in the isotropic four layer sphere the errors here are nearly twice as large. Looking at the differences in the errors between the element types a similar finding as for the three layer sphere can be made. The nodeshifted hexahedra mesh performs best, followed by the tetrahedra and the regular hexahedra mesh.

For the BEM solution the RDM gets as large as 0.17 for radial dipoles and as large as 0.10 for tangential dipoles. As in the four layer sphere it can be observed, that the BEM errors are less than the model error caused by ignoring the CSF layer and the anisotropy of the skull.

The comparison of BEM and FEM errors shows that the errors for FEM are clearly less than the BEM errors for radial dipoles at eccentricities higher than 0.85. For tangential dipoles the FEM errors are less than the BEM errors only for eccentricities larger than approx. 0.9.

As the RDM for the tetrahedra mesh tet229k_4layer_aniso in the four layer, anisotropic sphere reaches values of up to 0.08, the FEM solution was calculated for the additional

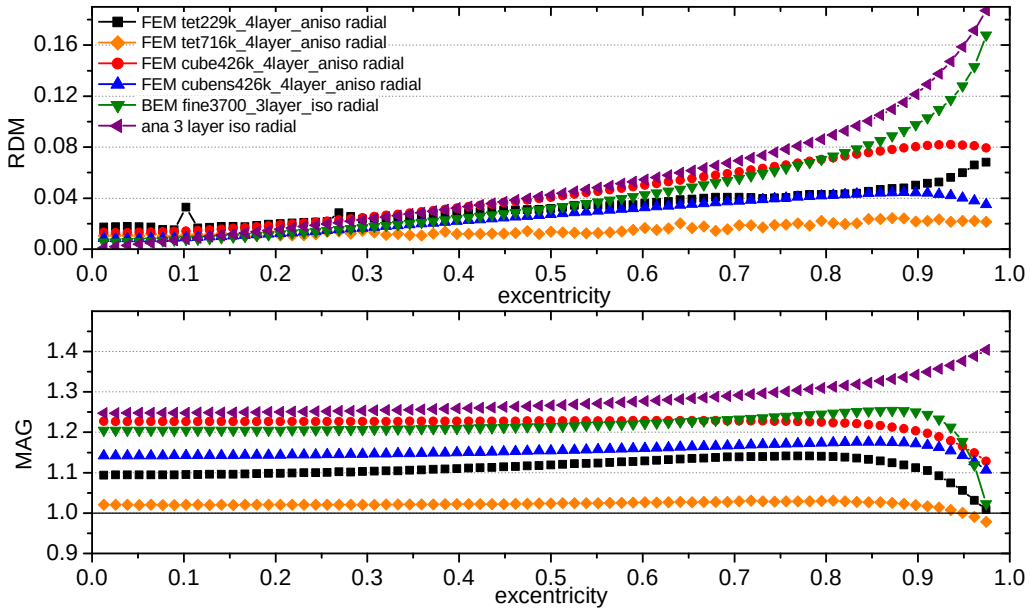

Figure 3.10: RDM and MAG for the BEM solution in the three layer, isotropic sphere model and for the FEM solution for different element types in the four layer, anisotropic sphere model. Radial Dipoles.

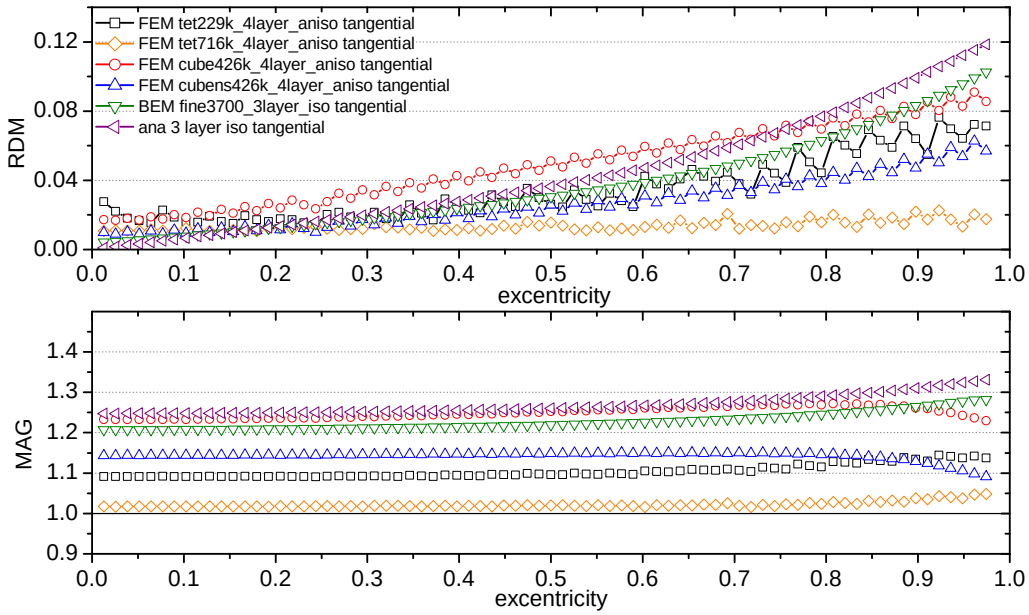

Figure 3.11: RDM and MAG for the BEM solution in the three layer, isotropic sphere model and for the FEM solution for different element types in the four layer, anisotropic sphere model. Tangential Dipoles.

tetrahedra mesh tet716k_4layer_aniso. It can be seen from figures (3.2(d)) and (3.2(e)) that the tet716k_4layer_aniso mesh is finer in the skull, the brain compartment and below the surface of the brain and that the tetrahedra in the tet229k_4layer_aniso mesh are less regular than those in the tet716k_4layer_aniso mesh. In addition figure (3.2(d)) shows that the only 2 mm thick CSF layer is not closed in the tet229k_4layer_aniso mesh. There are tetrahedra from the brain compartment which are directly connected to elements from the skull compartment. Although the new tetrahedra mesh has more nodes it is with regard to the computation time need for solving the inverse problem still comparable with the BEM mesh. (3.12) shows how this differences in the FEM meshes affect the accuracy of the FEM simulation in a four layer, anisotropic sphere.

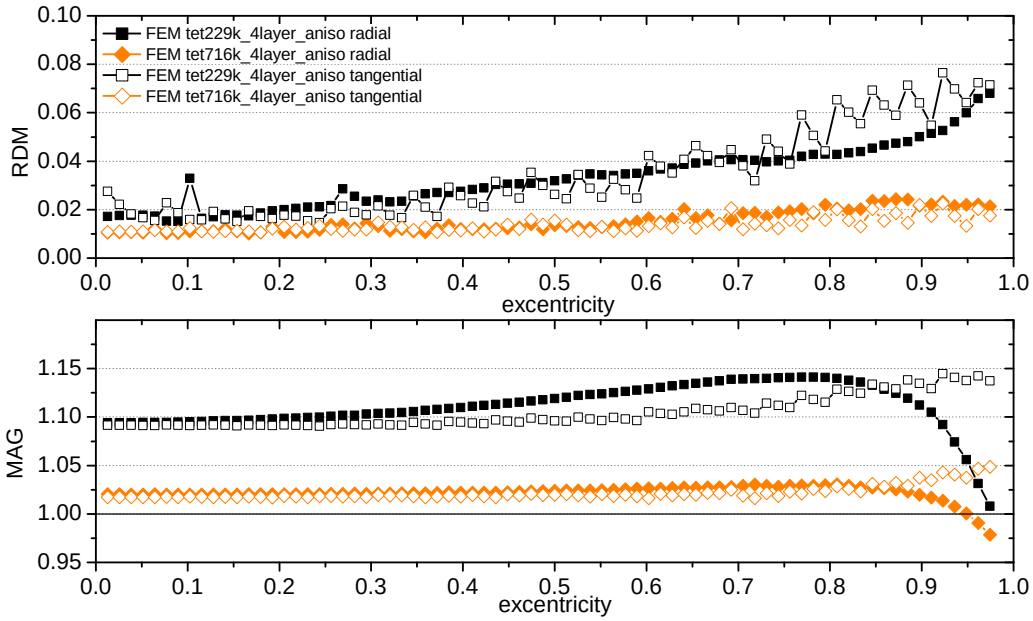

Figure 3.12: RDM and MAG for the FEM solution in two different tetrahedra meshes.

It can be observed that the new, locally refined tetrahedra mesh is much more accurate than the previously used one. The errors of the new mesh are now also clearly less than the errors of the BEM solution.

As the last study in this section the accuracies of the Venant approach, which was used for all FEM simulations up to this point, shall be compared to the accuracies of the subtraction approach. The comparison of the accuracies of both approaches for the tet716k_4layer_aniso-mesh can be seen in figure (3.13). The most obvious difference between the RDM curves is that the error curve for the subtraction approach is smooth and does not oscillate. For most eccentricities the RDMs of Venant's approach and subtraction approach do not differ much, but for high eccentricities the errors of the subtraction approach rise stronger than that of Venant's approach.

For a reasonable comparison of BEM and FEM the computational effort of both methods must be comparable. In table (3.8) the computation times for the BEM solution

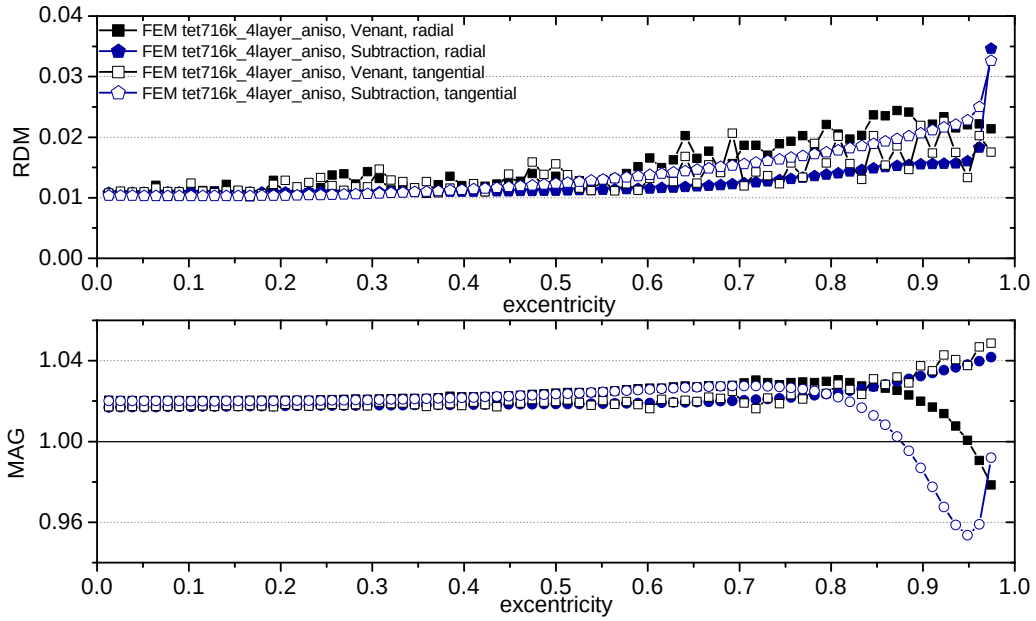

Figure 3.13: Accuracies of the FEM solution for the electric potential using Venant's approach and the subtraction approach.

and for the most accurate FEM solutions are shown.[1] BEM and FEM both need a constant time, listed in the first column, for setting up the simulations. In this time for BEM the inverse electric system matrix and for FEM the electric lead field basis is computed. After that one forward computation of the electric potential can be done quite fast. In the last column the times for calculating a typical lead field matrix are presented. The time for the computation of the lead field matrix is equal to the sum of the set-up time and the time needed for 30000 forward computations.

	setup	**one forward computation**	**lead field, 30000 sources**
fine3700_3layer_iso	70 min 59.62 s	26.6 ms	84 min 16.40 s
cubens426k_3layer_iso	29 min 14.30 s	1.1 ms	30 min 28.14 s
tet716k_4layer_aniso	56 min 31.64 s	2.6 ms	57 min 50.15 s

Table 3.8: Computation times for BEM and the most accurate FEM meshes.

[1] The computations were performed on a workstation equipped with a Intel Xeon 5130 CPU running at 2.0 GHz and 8 GB of memory.

3.2.2 Discussion of the Results of the EEG Studies

The results for FEM meshes with varying element size show that the FEM solution converges towards the analytical solution. The 2 mm meshes produce the best results. So global mesh refinement is one method to improve the accuracy of the FEM solution. This was also found e.g. in [18].

The increase of the FEM errors when the dipole approaches a compartment boundary can be explained by the large potential gradient of a dipole close to a discontinuity of the conductivity, which cannot be represented by the finite element ansatz functions when there are only a few finite elements between the source and the discontinuity. Increasing the number of elements in the vicinity of a conductivity jump can therefore increase the accuracy.

That the accuracy of the FEM solution using nodeshifted hexahedra meshes is better than the accuracy using regular hexahedra is due to the better approximation of the smooth sphere surfaces with the nodeshifted hexahedra and has also been shown in [37].

For the FEM solutions it was noticed that oscillation overlaid the error curves. These oscillations are characteristic for the Venant approach. When using Venant's approach the accuracy of the FEM solution depends on the position of the dipole relative to the next FE node. The solutions are most accurate when the source is lying on a node. For the BEM solution a strong increase of the errors was found, when the dipole comes close to the surface of the innermost sphere, which was also confirmed in e.g. [6]. Due to the numerical problems of BEM with sources close to a discontinuity of the conductivity the FEM solutions in nodeshifted hexahedra and tetrahedra meshes are more accurate for realistic sources at higher eccentricities.

The accuracies of the FEM simulations in the four layer, isotropic sphere models are comparable to those in the three layer, isotropic sphere model. Only for the nodeshifted hexahedra meshes the errors are slightly larger. This is probably because it is very hard to model the only 2 mm thin CSF layer with hexahedra elements of 2 mm size. Figure (3.1.3) shows that the CSF layer is not well approximated in the nodeshifted hexahedra mesh.

It is at first sight surprising that the error between the three layer BEM mesh and the analytical solution for the four layer, isotropic and anisotropic sphere model is less than the model error caused by ignoring the CSF layer respectively the CSF layer and the anisotropy of the skull. The reason for this is that the numerical errors of the boundary element method and the model error by accident do not add up, but partly cancel each other. One can not expect that this will always be the case when modelling a four layer, isotropic or anisotropic sphere model using a three layer, isotropic BEM mesh.

From the study in the four layer, anisotropic sphere one can see, that the errors of the FEM simulations with an anisotropic skull are nearly twice as large as the errors for an isotropic skull. This is most likely due to the not fine enough discretisation of the skull. The comparison between the tet229k_4layer_aniso tetrahedra mesh and the tet716k_4layer_aniso tetrahedra mesh, where the skull, was locally refined, confirms this. In addition the area close to the border of the brain compartment was refined in the new mesh. As already above discussed small elements in this region are necessary for an

accurate simulation of eccentric dipoles. It can be seen in figure (3.12) that the errors for a four layer, anisotropic sphere model can be reduced by a factor 3 to 4 by locally refining the skull and the area below the interface between the brain and the CSF compartment. For realistic head models it can be expected that a FEM mesh which was refined in a similar way will produce similar accuracies, because the accuracy of the finite element method does not depend on the geometry[36]. So for the studies of FEM in a realistic volume conductor the FEM solution for such a locally refined mesh can be taken as a very accurate reference solution.

Regarding the errors of the tet716k_4layer_aniso mesh one can state that it is possible to simulate the EEG in a four layer, anisotropic sphere model much more accurate using the finite element method than using the boundary element method.

For high eccentricities near the border of the brain compartment the subtraction approach is not as good as the Venant approach. In [36] it was proven, that the subtraction approach gets less accurate when a dipole comes close to a discontinuity of the conductivity. It is nevertheless suspected that the higher errors of the subtraction approach for high excentricities are partly caused by a not optimal implemenation of the method. In the implementation of the subtraction approach used here the analytically computed potential ϕ^{∞} is approximated with linear finite element ansatz functions. This does not seem to be sufficient for sources close to conductivity jumps. In an improved implementation it was already shown that approximating ϕ^{∞} with higher order polynomials increases the accuracy for these sources.

The computation times needed for the most accurate FEM meshes are comparable to the computation time needed for the BEM solution. Even for a large number of forward computations the set-up time is dominating the overall time needed. With regard to the application the set-up time is not very critical, because the computations for the set-up only have to be done once for each mesh. The results, that is the inverted system matrix for BEM and the lead field basis for FEM, can be stored and reused for a fast solution of the inverse problem. The time for one forward computation is for FEM shorter than for BEM. In BEM and FEM after the set-up the electric potential can be computed by multiplying the source vector to the inverted electric system matrix respectively the electric lead field matrix. Both matrices have s rows, where s is the number of sensors. So the time for the matrix-vector-multiplication is determined by the number of multiplications needed for multiplying a row vector of the matrix to the source vector. For BEM this number is equal to the number of nodes of the BEM mesh. Using the Venant approach for FEM the source vector is not fully populated, but there are only as many non-zero entries in the source vector as there are neighbouring nodes to the node, which is closest to the current dipole. Typically the source vector has, depending on the element type, around 30 non-zero entries. So using FEM only around 30 multiplications are needed for the multiplication of the row vector of the lead field matrix and the source vector instead of a few thousand using BEM.

3.2.3 Results of the MEG Studies

The MEG studies were carried out using the one layer, isotropic volume conductor described in table (3.5). The magnetic flux was calculated for each of the three sets of magnetometers described in section (3.1.1) and for 79 dipoles at the same positions as in the EEG studies. Because radial dipoles in a sphere do not produce any magnetic field outside[21], only tangentially orientated dipoles were used. The analytical solution was computed using Sarvas formula[21] and the numerical solutions were computed using BEM and FEM with Venant's approach.

It was pointed out before, that the magnetic flux due to brain activity can be separated into two parts. The first one, here called the primary magnetic flux, describing the contribution of the primary or impressed current and the second part, the secondary magnetic flux, describing the contribution of the secondary or volume currents. In the numerical methods BEM and FEM the two contributions are treated in a very different way. The primary flux can always be computed analytically, that is nearly exact. Whereas the secondary flux is computed numerically. That is why below the errors not only for the total magnetic flux, but also for the primary and secondary magnetic flux were calculated.

Radial Magnetometers

First radially orientated magnetometers will be discussed. Figure (3.14) shows the L_2-norm of the primary and secondary magnetic flux relative to the L_2-norm of the total magnetic flux for the set of radial magnetometers and for the 79 dipoles with varying eccentricity. Primary, secondary and total magnetic flux were computed analytically.

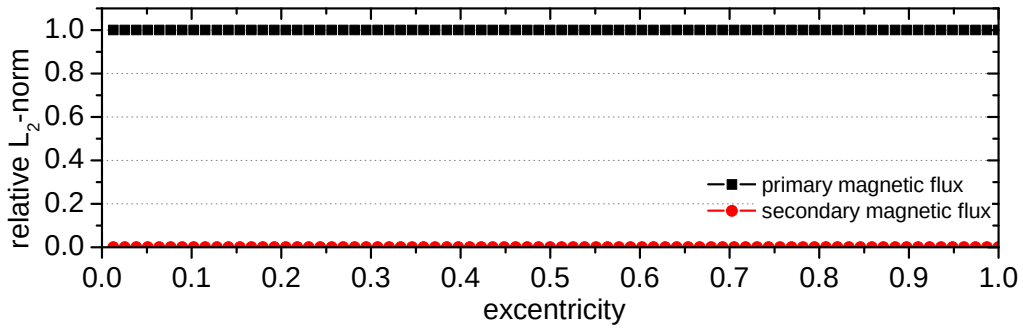

Figure 3.14: The L_2-norm of the primary and secondary magnetic flux relative to the L_2-norm of the total magnetic flux for radial magnetometers.

The relative L_2-norm of the primary magnetic flux is everywhere 1, whereas the relative L_2-norm of the secondary magnetic flux is everywhere 0.

The total strength of the magnetic flux depending on the dipole eccentricity can be seen in figure (3.15) where the L_2-norm of the total magnetic flux is plotted against the dipole eccentricity. It can be seen that the strength of the magnetic flux which can be measured outside the head decreases when the dipole approaches the centre of the spheres. A dipole in the centre of the sphere would not generate any magnetic flux

outside of the sphere.

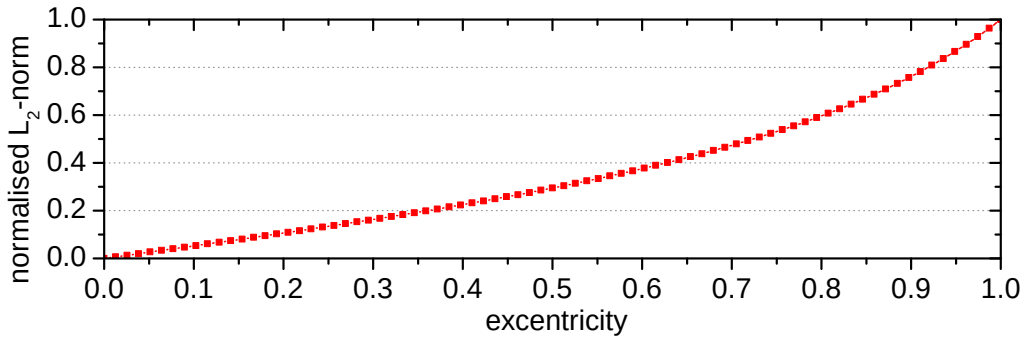

Figure 3.15: The L_2-norm of the total magnetic flux for radial magnetometers normalised to its maximum.

For the errors between the numerically and analytically computed primary magnetic flux, values that were less than 10^{-4} for the RDM and for $|MAG - 1|$ were found. The errors of the primary magnetic flux are always very small not depending on whether FEM or BEM was used, not depending on the meshes used for FEM and BEM and not depending on the orientation of the magnetometers.

The errors of the numerically computed secondary magnetic flux measured with radial magnetometers are very large. The RDM reaches values of more than 1 and the MAG is always larger than 100.

Figure (3.16) shows the error curves of the FEM and BEM solutions for the total magnetic flux for radial magnetometers.

For reasonable eccentricities $\gtrapprox 0.3$ the RDM of the FEM and BEM solutions is less than 0.25 and the MAG lies between 0.98 and 1.05. For lower eccentricities, that is when the dipole comes closer to the centre of the spheres, the errors sharply rise.

Tangential Magnetometers

The contribution of the primary and secondary magnetic flux to the total magnetic flux for the second set of tangentially orientated magnetometers is shown in figure (3.17). The plot for the second set of tangential magnetometers looks very similar and is omitted.

The dependence of the total strength of the magnetic flux on the dipole eccentricity is for the tangential magnetometers very similar to that for the radial magnetometers. Therefore the plot for the L_2-norm of the total magnetic flux for the tangential magnetometers is not shown here. In addition the errors for the primary magnetic flux can be neglected for the tangential magnetometers, too.

In figures (3.18) and (3.19) the RDM and MAG of the numerically computed secondary magnetic flux for the first respectively second set of magnetometers is presented.

The RDM for the FEM solutions is nearly everywhere and for both magnetometer configurations below 0.04 and the MAG lies between 0.98 and 1.03. As for the EEG the error curves are oscillating, but here the amplitudes of this oscillations especially for the tetrahedra mesh are larger.

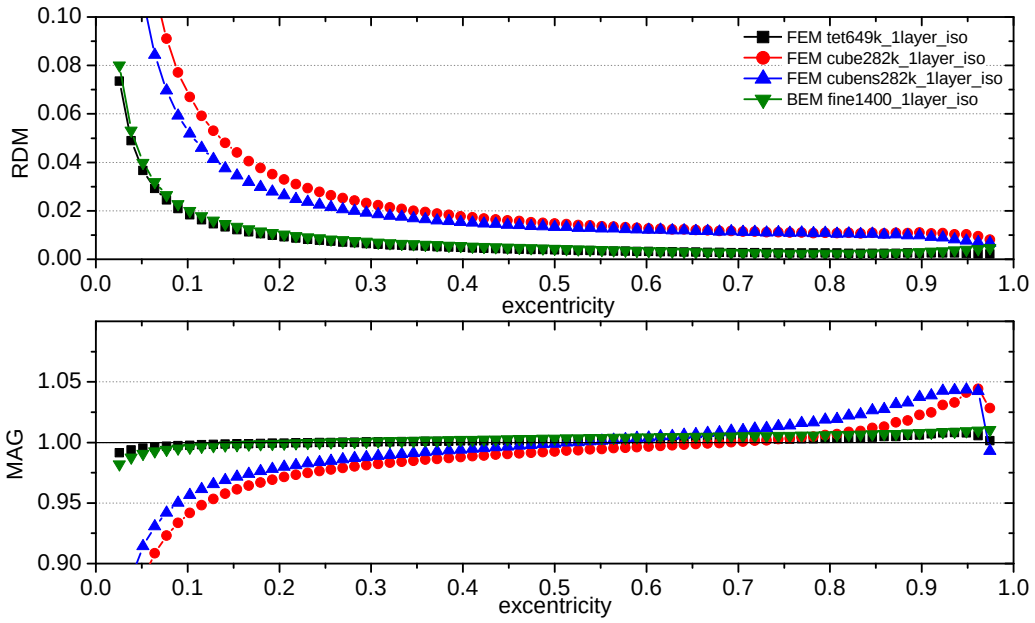

Figure 3.16: RDM and MAG of the BEM and FEM solutions for the total magnetic flux for the radial magnetometers.

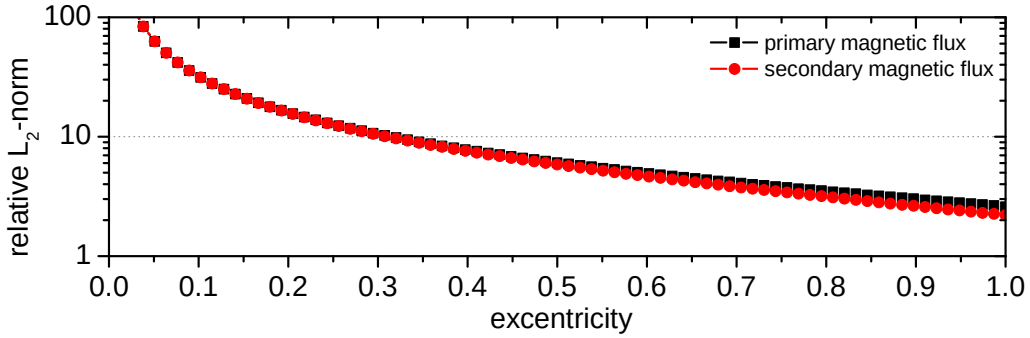

Figure 3.17: The L_2-norm of the primary and secondary magnetic flux relative to the L_2-norm of the total magnetic flux for the first set of tangential magnetometers.

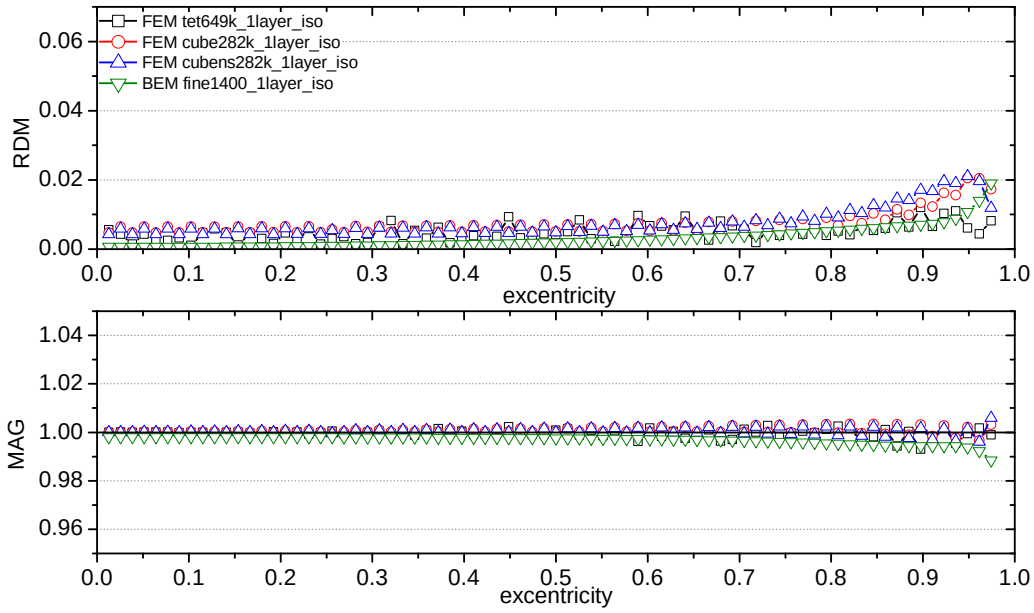

Figure 3.18: RDM and MAG for the BEM and FEM solutions of the secondary magnetic flux for the first set of tangential magnetometers.

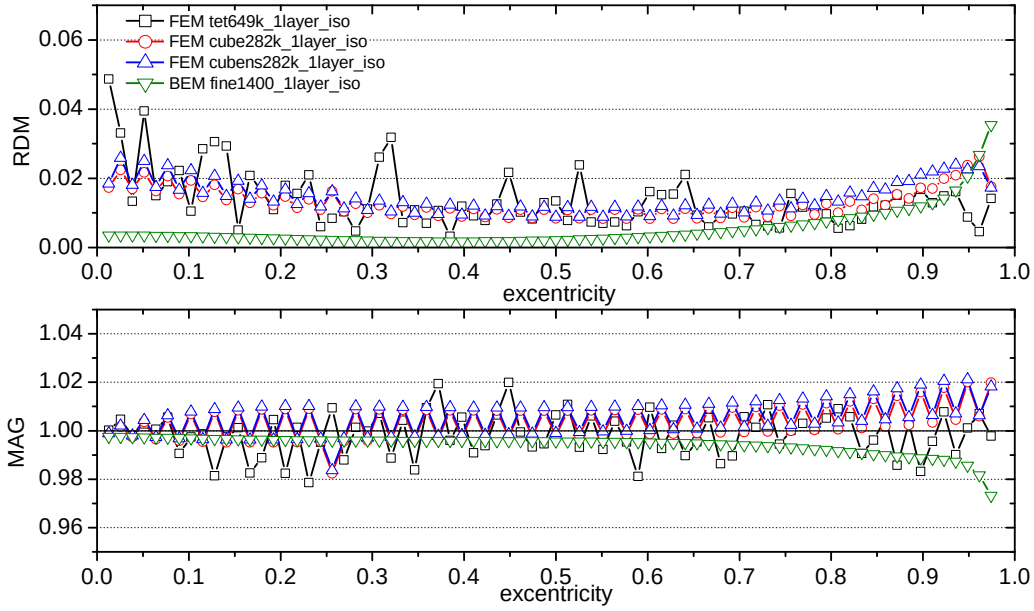

Figure 3.19: RDM and MAG for the BEM and FEM solutions of the secondary magnetic flux for the second set of tangential magnetometers.

When comparing the element types one can see, that the hexahedra models are approx. equally accurate. Due to the large oscillations the tetrahedra model performs worse for a few dipoles.

For the BEM solution for eccentricities up to 0.9 the RDM is below 0.02 and the MAG is between 0.98 and 1.0, but for higher eccentricities the RDM rises towards a value of ≈ 0.04 and the MAG decreases until 0.97.

Finally figures (3.20) and (3.21) show the errors of the total magnetic flux.

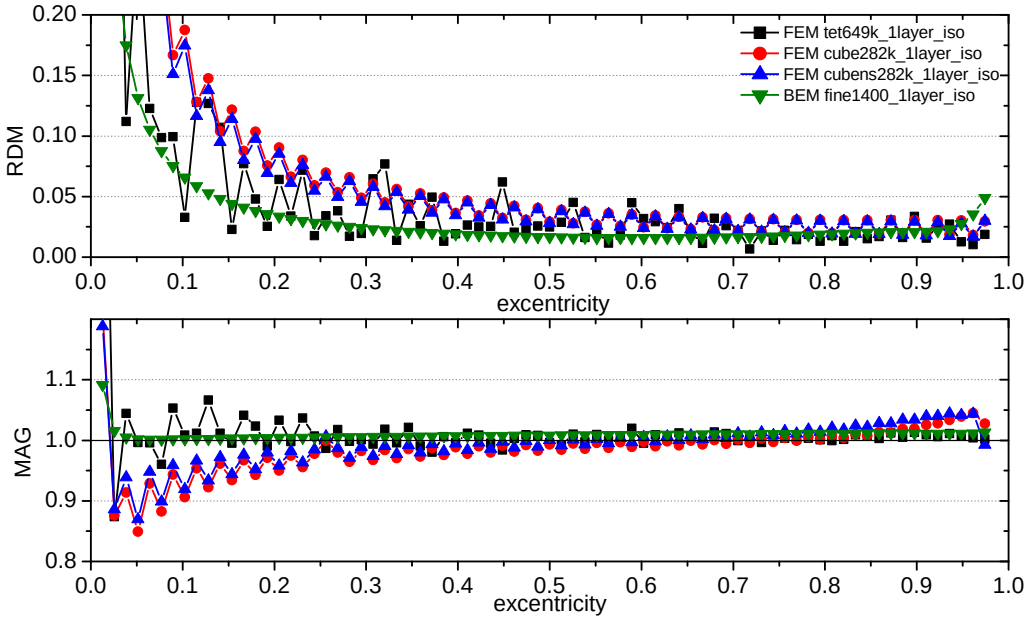

Figure 3.20: RDM and MAG for the BEM and FEM solutions for the total magnetic flux for the first set of tangential magnetometers.

As for the secondary magnetic flux the hexahedra meshes produce better results with higher accuracies. For the FEM simulations in hexahedra meshes the maximum RDM for reasonable eccentricities is below 0.05 and the MAG lies between 0.95 and 1.05. The error curves for the tetrahedra mesh are strongly oscillating, so that the maximum RDM for reasonable eccentricities is 0.10 and the MAG lies approx. between 0.95 and 1.05. Just like seen before, for dipoles close to the centre of the spheres the errors for all numeric methods get worse. The RDM for the BEM solution is at the maximum ≈ 0.08 and the MAG lies between 0.97 and 1.03.

For the second set of tangential magnetometers, where the volume currents significantly contribute to the total magnetic flux and where the errors for the secondary magnetic flux are getting important, the secondary and total magnetic flux are also computed using the subtraction approach. In figure (3.22) the accuracies of the subtraction approach for the secondary and total magnetic flux are compared to the accuracies of Venant's approach. It is here even more obvious than for the EEG that the accuracies of the subtraction approach do not oscillate. In addition the subtraction approach is

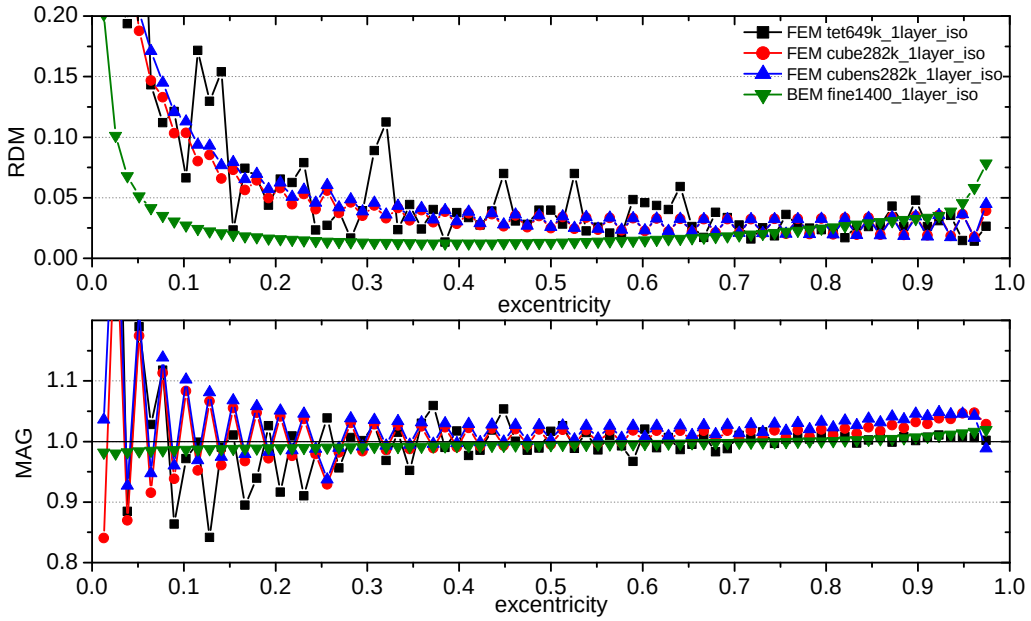

Figure 3.21: RDM and MAG for the BEM and FEM solutions for the total magnetic flux for the second set of tangential magnetometers.

everywhere more accurate than Venant's approach.

As for the EEG studies the computation times needed for BEM and for the most accurate FEM meshes are compared. Again both methods first need some time for setting up the simulations. Using BEM for the MEG in this time the inverted electric system matrix and the magnetic system matrix are computed. In the set-up for the MEG simulations using FEM first the secondary magnetic flux integration matrix and then the magnetic lead field matrix has to computed. The table (3.9) in addition shows the time for one forward computation and the time for the computation of a typical lead field, which is the set-up time plus the time needed for 30000 forward computations.

	setup	**one forward computation**	**lead field, 30000 sources**
fine1400_1layer_iso	2 min 48.26 s	21.1 ms	13 min 22.06 s
cubens282k_1layer_iso	24 min 54.96 s	1.0 ms	25 min 26.31 s
tet649k_1layer_iso	122 min 6.10 s	2.8 ms	125 min 10.44 s

Table 3.9: Computation times for BEM and the most accurate FEM meshes.

Realistic Sensor Configuration

In the sections above the strength of the total magnetic flux and the contribution of the primary and secondary magnetic flux were already studied, but only for synthetic sensor

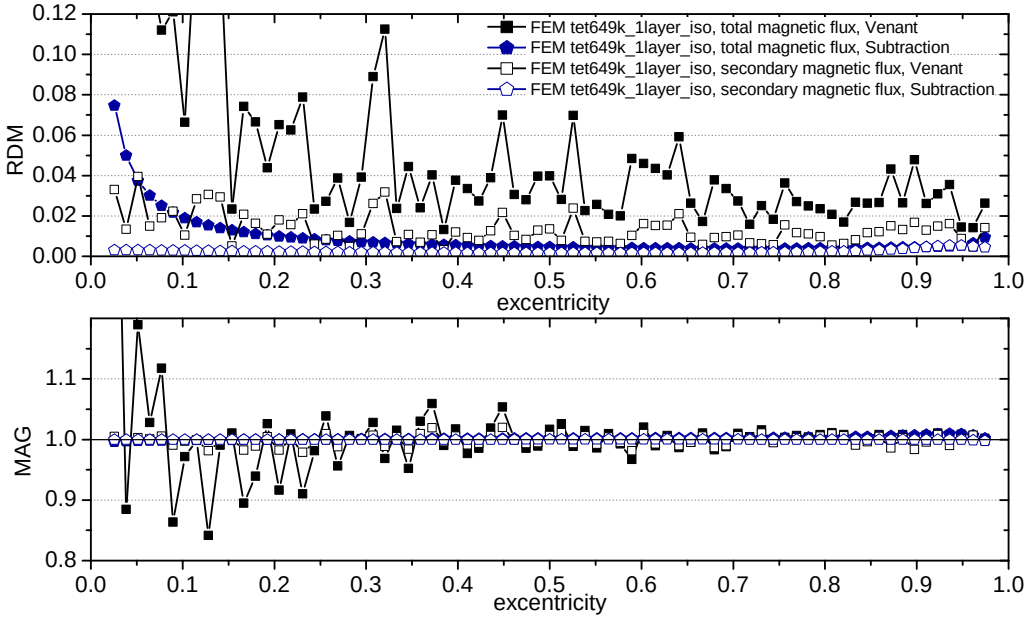

Figure 3.22: Accuracies of the FEM solution for the secondary and total magnetic flux using Venant's approach and the subtraction approach.

configurations with completely radial respectively completely tangential sensors. In this section these two points will be studied for the realistic sensor configuration of the MEG machine at the Institute for Biomagnetism and Biosignalanalysis (IBB). Primary, secondary and total magnetic flux generated by tangential dipoles distributed regularly on the surface of a concentric sphere with radius 76 mm were calculated using FEM and the Venant approach in the cubens282k_1layer_iso mesh. Simulations were performed using no noise rejection by means of higher order synthetic gradiometers. Figures (3.23(a)) and (3.23(b)) show the strength of the total magnetic flux respectively the difference between the L_2 norm of the primary and secondary magnetic flux depending on the location of the source.

The total magnetic flux is maximal for dipoles on the left or the right of the sphere and on top of the sphere. For dipoles at the bottom of the sphere the flux is weakest. When looking at the relative difference between the strength of the primary magnetic flux and the secondary magnetic flux it can be observed that the primary flux is for all dipoles stronger. Especially on the left and on the right of the sphere. The contribution of the secondary magnetic flux is largest for dipoles at the bottom of the sphere.

3.2.4 Discussion of the Results of the MEG Studies

Radial Magnetometers

From figure (3.14) one can see, that the secondary magnetic flux is exactly zero and does not contribute to the total magnetic flux for the case of radial magnetometers. This is

(a) L_2 norm of total magnetic flux normalized to the maximum of all dipoles.

(b) Difference of L_2 norms of primary and secondary magnetic flux relative to L_2 norm of total magnetic flux.

Figure 3.23: On the strength of the total magnetic flux and the contribution of primary and secondary magnetic flux produced by tangential dipoles distributed on a concentric sphere with radius 76 mm. No noise rejection was applied.

consistent with [21], where it is shown that, for a sphere, the radial magnetic field is produced exclusively by the primary currents. The secondary currents in a sphere do not contribute to the radial component of the magnetic field outside.

Very small errors were observed for the primary magnetic flux and radial sensors. These can be explained by the fact that the primary magnetic flux is computed analytically even when using BEM or FEM.

For the secondary magnetic flux very large errors were observed. This is because the numerically computed magnetic flux for radial magnetometers is not exactly zero, but still has a very small absolute value. When comparing this very small secondary magnetic flux to the analytically computed secondary magnetic flux, which is nearly exactly zero, this results in large relative errors.

The small, absolute errors of the numerically computed secondary magnetic flux also influence the error of the total magnetic flux. These small, absolute errors of the secondary magnetic flux get especially important for sources close to the centre of the spheres. For these deep sources the strength of the total magnetic flux decreases and the small, absolute error of the secondary magnetic flux gets more important and causes a larger, relative error.

Tangential Magnetometers

In figure (3.17), showing the relative strength of the primary and secondary magnetic flux, it can be observed that the strength of the primary and secondary magnetic flux is larger than the strength of the total magnetic flux. In addition it can be noticed that the strength of the contributions from the primary currents and secondary currents are nearly equal. These facts indicate that the primary and secondary magnetic flux nearly cancel out each other. The total magnetic flux is then the small difference between primary and secondary magnetic flux. This is important for the way the small absolute errors affect the relative error of the total magnetic flux.

Oscillations in the error curves for the secondary magnetic flux calculated using FEM were observed. These have the same reason as in the EEG. In general it can be said that because of equation (2.37) the accuracy of the secondary magnetic flux is directly related to the accuracy of the electric potentials.

As the primary flux can be calculated analytically and therefore exact also for tangential magnetometers, the errors of the total magnetic flux are dominated by the errors of the secondary magnetic flux. The peaks of the RDM for the tetrahedra mesh are, for example, for the total magnetic flux at the exact same position as for the secondary magnetic flux. But there is a difference in the magnitude of the errors. The small absolute errors of the secondary magnetic flux get more significant relative to the total magnetic flux, which has especially for deep dipoles a small total strength. The BEM solution is except for the most superficial sources at least as accurate as the FEM solution.

For the MEG the subtraction approach can clearly improve the RDM and the MAG for the whole range of eccentricities.

Comparing the computation times for BEM and FEM for the MEG yields a different picture as for the EEG. The lead field computation is faster using BEM than using FEM. This is due to the fact that the setup of the BEM simulations is very fast for a

one layer BEM model. Calculating the secondary magnetic flux integration matrix and the magnetic lead field does not depend on the number of layers, but on the number of nodes. And the number of nodes for the one layer models is not much less than the number of nodes for the three or four layer models used in the EEG studies. As for the EEG it can still be observed that the main time for the computation of a lead field using FEM is needed for the set-up, which is not a problem in the application.

4 The Phantom Study

In this chapter the MEG forward computation using FEM shall be validated by solving the inverse problem for measured data, where the underlying current distribution is known. Therefore the MEG for a set of current dipoles in a phantom head is measured. The positions and orientations of the dipoles are then reconstructed by solving the inverse problem using FEM for the forward computations. The reconstruction results are compared to the real position and orientation of the dipole, which can be measured directly at the phantom. Furthermore the reconstruction results are compared to the reconstruction results of a well tested software, which uses an analytical solution to solve the forward problem.

4.1 Methods

In this section the methods of the phantom study shall be presented. This includes the description of the head phantom, the MEG machine and the details on the measurement procedure. In addition details on the used FEM meshes and the inverse procedures are provided.

4.1.1 Head Phantom

The head phantom consists of a plastic sphere, which is filled with NaCl solution. The measures of the sphere can be seen in figure (4.1). The concentration of NaCl in the solution is known to be $c = 0.14\,\mathrm{mol/l}$. Therefore the conductivity of the solution can be estimated as $\sigma = 1.73\,\mathrm{S/mm}$. To measure the position of the phantom relative to the

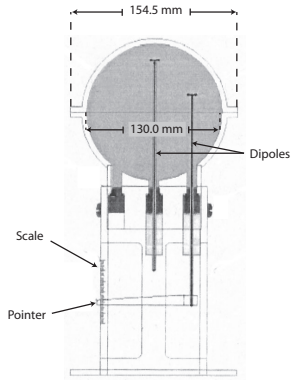

Figure 4.1: The phantom head model. From [30].

dewar of the MEG machine, fiducial coils have to be attached to the phantom. The coils can be attached to the four mounts which are equally distributed along the equatorial line of the phantom model.

The electric activity of the brain is simulated in the phantom with current dipoles. These dipoles consist of two gold globes at a distance of 9 mm to each other. The dipole is attached to a plastic rod which is inserted into the phantom through one of several holes in the lower area of the plastic sphere. By choosing different holes the position of the dipole in x and y direction can be varied. The position of the dipole in z direction can be varied continuously by sliding the rod in or out of the sphere. A electric potential between the two globes of the dipole is applied by the data acquisition software and controlled in such a way that a given dipole moment is met.

4.1.2 MEG Machine

The MEG machine is a *Omega 2005* from the manufacturer *VSM Medtech Ltd.*. It is equipped with 275 measurement sensors. The measurement sensors are axial gradiometers with a baseline of 50 mm. The coils of the gradiometers have a radius of 9 mm. For the noise rejection technique described in section (2.8) the magnetic flux is furthermore measured at 29 reference sensors which are situated in the dewar above the measurement sensors. The reference sensors are magnetometers and axial and planar gradiometers. The radii of the coils differ between 7.76 and 17.27 mm. The baseline of the reference gradiometers is always 78.74 mm. Figure (4.2) shows the FEM nodes which are used to model the measurement and reference sensors.

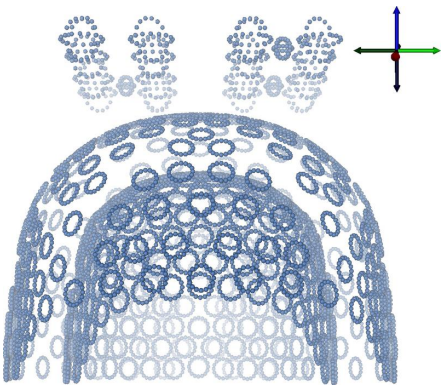

Figure 4.2: FEM nodes that were used to model the CTF MEG sensor configuration. Including measurement and reference sensors.

4.1.3 Measurement Procedure

During the measurement an sinusoidal electric potential at a frequency of $\nu = 5\,\mathrm{Hz}$ is applied between the two globes of the dipole. The amplitude of the potential is chosen in such a way that the amplitude of the resulting electric current between the globes

is $I = 100\,\mu$A. As the distance of the globes is $d = 9\,$mm the resulting moment of the dipole is $M = I \cdot d = 900\,$nAm.

The MEG was recorded for dipoles at 5 positions along an axis parallel to the z-axis, but 3.61 cm displaced in direction of the y-axis. The dipoles were placed on that axis in steps of 1 cm whereas the lowest dipole is at the same height as the centre of the sphere. The dipoles were orientated in x-direction.

The signal at the sensors is sampled at a frequency of $f = 600\,$Hz. The measurement of the magnetic flux generated by the dipole is divided into 100 trials. Each trial lasts 1 s. The start of each trial is fixed to the phase of the sinusoidal dipole current. Already during acquisition, i.e. on-line, a baseline correction, a low pass filter at 40 Hz, a notch filter at the frequency of the electrical system, 50 Hz, and noise rejection with synthetic 3rd order gradiometers is applied to the data. Finally, to improve the signal to noise ratio the 100 trials are averaged.

4.1.4 Generation of the FEM Meshes

For the computation of the electric potentials and the magnetic flux, a FEM mesh has to be created, which represents the geometry and the electric conductivity of the volume conductor.

As the phantom is a sphere the FEM meshes can be created as they were used to be created in the multilayer sphere validation studies (chapter (3)). First a synthetic MR image of a sphere with the measures of the phantom is created. For the tetrahedra meshes this image is then segmented in CURRY[9]. The creation of the tetrahedra FEM mesh is also done in CURRY (see section (2.6.1)). Furthermore a regular and a nodeshifted cube mesh were generated by segmenting the synthetic MR image and building the mesh with VGRID[27] as explained in section (2.6.1). Because the phantom as a volume conductor is homogeneous and isotropic the isotropic conductivity $\sigma_{\text{iso}} = 1.73\,$S/m is assigned to all elements of the FEM meshes. Details on the three used FEM meshes can be found in table (4.1).

	element type	**element size**	**# nodes**	**# elements**
tet131k_phantom	tetrahedra	2.0 mm	131902	795245
cube153k_phantom	hexahedra, regular	2.0 mm	153104	143017
cubens153k_phantom	hexahedra, nodeshifted	2.0 mm	153104	143017

Table 4.1: The FEM meshes used for the phantom study.

4.1.5 Inverse Methods

To find the current distribution which caused the magnetic flux measured in the phantom study two inverse methods were applied to the data: a goal function scan and a moving

dipole fit (2.9).

The grid on which the goal function scan was performed was identical to the respective FEM mesh used for the forward computations. As the grid contains several thousand nodes the lead field basis approach is used to speed up the simulation of the magnetic flux. As reference data for the goal function scan the data with and without applied noise rejection by means of higher order synthetic gradiometers was used.

The second inverse method that was used is the moving dipole fit. The initial source position was arbitrarily fixed for all dipoles to $(x, y, z) = (0.0, 37.0, 0.0)\,\mathrm{mm}$. For the optimization of the dipole position a simplex optimizer was used. The optimizer was given a very low final residue of 0.1 to aim for and the maximum number of iterations was set to 1000. The dipole was fitted to data with and without applied noise rejection technique.

When applying the goal function scan or the moving dipole fit to the data with applied noise rejection the noise rejection was of course taken into account in the forward computations.

The reconstruction results of the goal function scans and the moving dipole fits are compared to two sets of reference dipole parameters. The first reference is the position and orientation of the dipole measured directly at the phantom head model. During the measurements a slackness in the guideway of the dipole was observed. Due to this imperfection of the phantom the directly measured x- and y-coordinates of the dipole have got a quite large uncertainty of 3 mm.

Because of this uncertainty in the directly measured dipole position, the reconstruction result of the commercial software from *CTF*, the manufacturer of the MEG machine, was chosen as another reference. The software uses the exact analytical solution in a sphere for the forward computations. As the phantom model has a spherical geometry and as the inverse algorithms implemented in this commercial software were thoroughly tested, it can be assumed, that the reconstruction results of this software are the most accurate results, that can be achieved for the phantom data.

4.2 Results and Discussion

In this section the results of the phantom study, first the reconstruction results of the goal function scans and then the reconstruction results of the moving dipole fits, are presented.

4.2.1 Results of the Goal Function Scans

In each of the three FEM meshes and for all five dipole positions a goal function scan was performed. As the reference data for the goal function scan the measured data with and without noise rejection by means of 3rd order synthetic gradiometers was chosen. As a result of the scan one goal function value for each node of the mesh is obtained. An example of the result of a goal function scan can be seen in figure (4.3).

The position of the node with the highest goal function value is then chosen as the reconstructed dipole position. Figures (4.4) and (4.5) show the reconstruction results

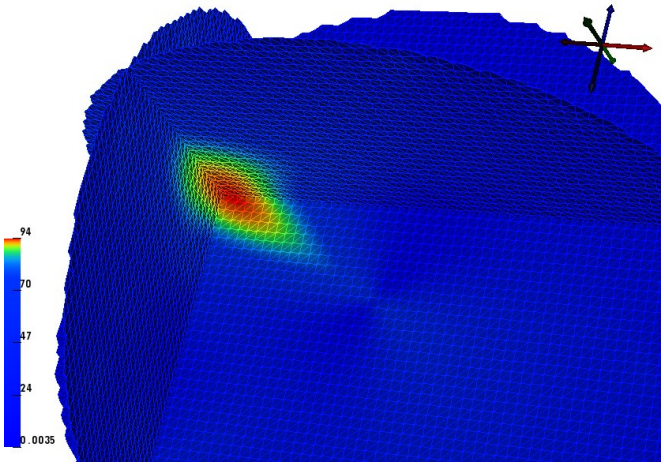

Figure 4.3: The result of a goal function scan in the cube153k_phantom FEM mesh for the dipole at $z = 20\,\text{mm}$. The goal function values are displayed on three orthogonal planes which intersect in the dipole position, which was directly measured at the phantom. Note that the colour scale is shifted.

of the goal function scan on data with and without noise rejection projected on the x-z-plane respectively the y-z-plane in comparison to the two reference solutions.

To quantify the mislocalisations the euclidean distance between the reconstructed positions from the goal function scan and the reference positions is calculated. In figure (4.6) the distance between the reconstructed dipole positions and the directly measured dipole position is presented. And in figure (4.7) the localisation errors of the goal function scans relative to the CTF reconstruction results are shown. From these figures one can observe that the maximum distance of the reconstruction results from the goal function scan to the directly measured dipole positions is below 6.0 mm and the maximum distance to the CTF reconstruction results is even below 5.0 mm. The average mislocalisation across all dipoles is approx. 3.0 to 4.0 mm relative to the directly measured dipole position and in the range between 1.5 and 3.0 mm relative to the CTF reconstruction results.

4.2.2 Discussion of the Goal Function Scan Results

The localisation errors of the goal function scans for all FEM meshes and for data with and without noise rejection are very low. When comparing finite element types no significant differences can be found for the localisation errors relative to the directly measured dipole positions. For the localisation errors relative to the CTF reconstruction results the nodeshifted hexahedra mesh performs slightly better than the tetrahedra and the regular hexahedra. This is consistent with the accuracies of the different element types in the multilayer sphere studies in chapter (3).

The noise rejection technique obviously does only improve reconstruction accuracy for deep dipoles. For more superficial dipoles using 3rd order synthetic gradiometers slightly impairs the localisation errors. This is due to the fact, that for 3rd order synthetic gradiometers the contribution of the secondary magnetic flux is larger, because the

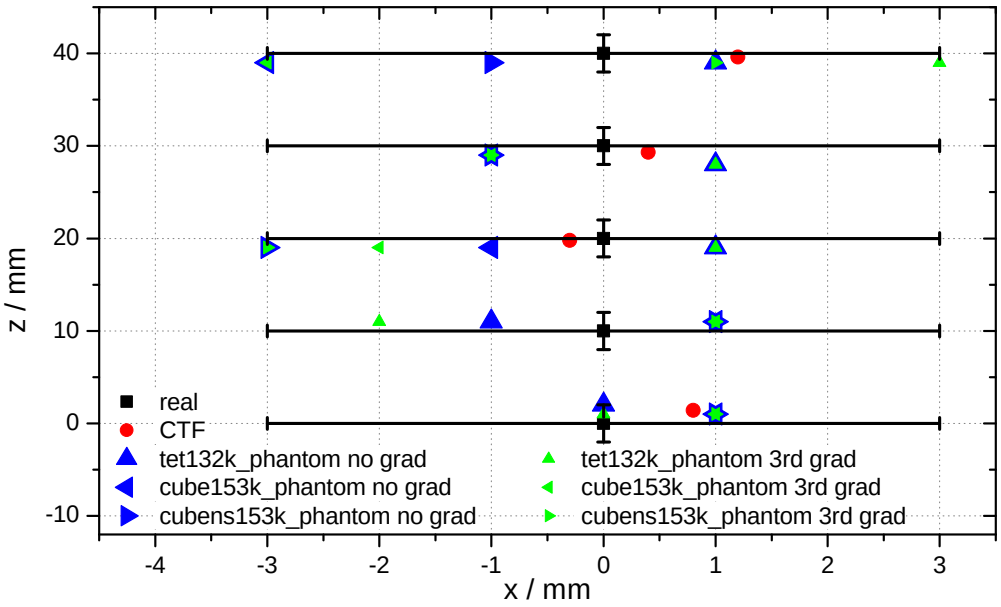

Figure 4.4: Localisation results for the goal function scans on data with and without applied noise rejection in the three FEM meshes projected on the x-z-plane. The label *real* marks the directly measured dipole positions. The label *CTF* marks the CTF reconstruction results.

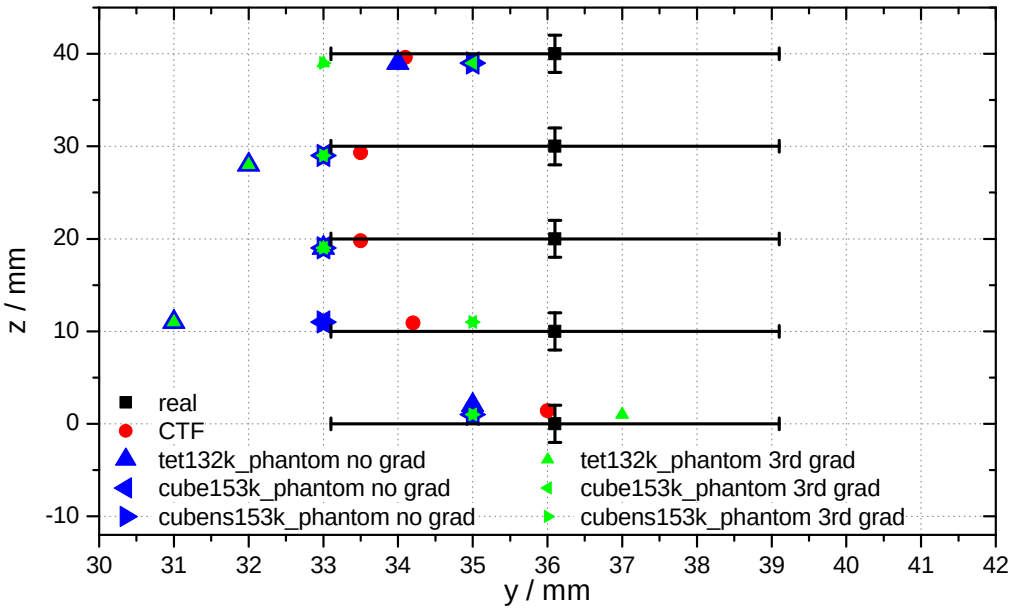

Figure 4.5: Localisation results for the goal function scans on data with and without noise rejection in the three FEM meshes projected on the y-z-plane. The label *real* marks the directly measured dipole positions. The label *CTF* marks the CTF reconstruction results.

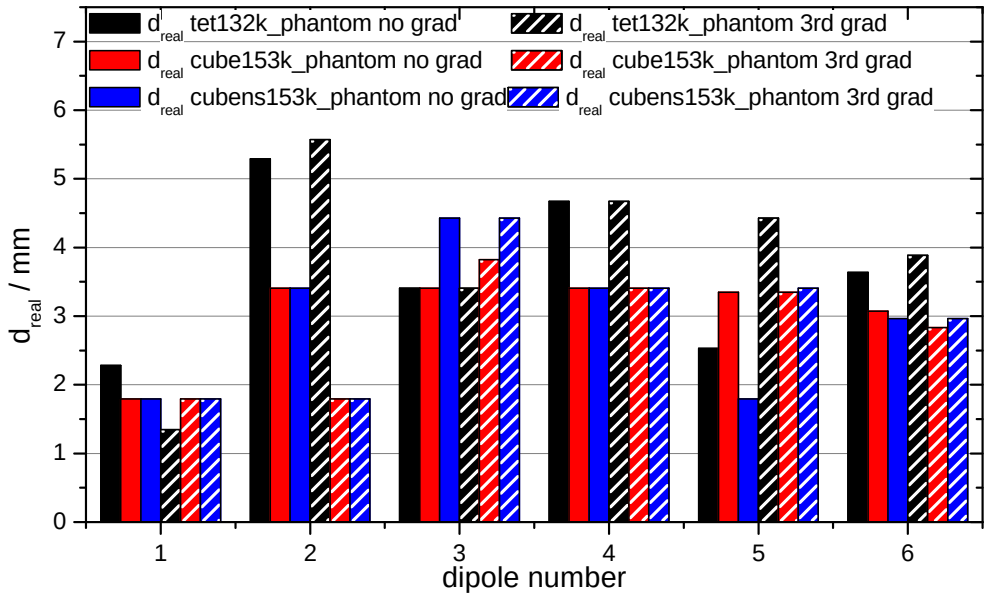

Figure 4.6: Euclidean distance between the reconstruction results from the goal function scans and the directly measured dipole position.

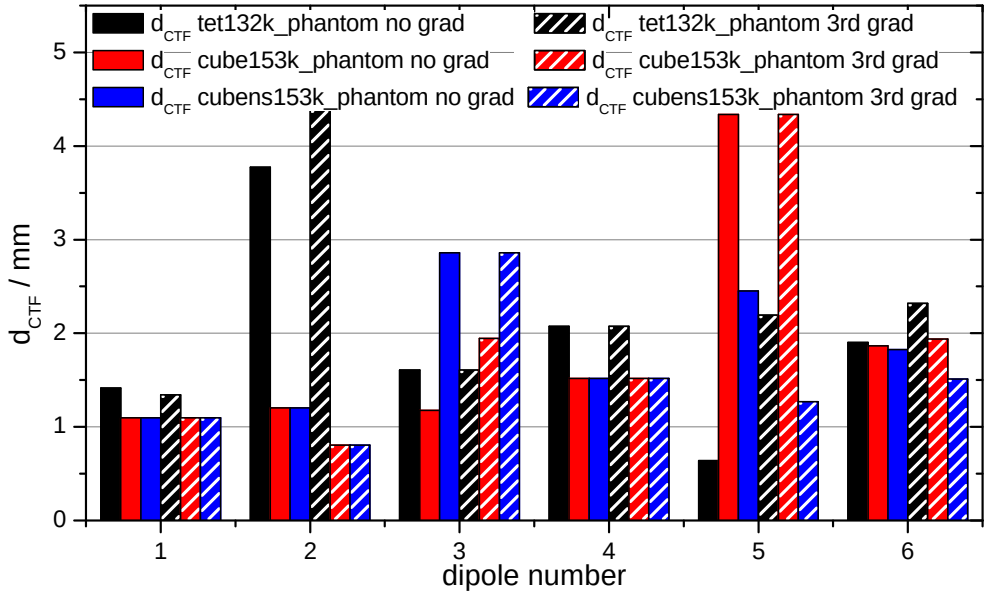

Figure 4.7: Euclidean distance between the reconstruction results from the goal function scans and the reconstruction results from the CTF software.

reference sensors also measure the tangential component of the magnetic field outside the head. In this way the numerical error of the secondary magnetic flux contributes more to the error of the total magnetic flux. And the higher numerical error causes larger localisation errors. In the average across all five dipoles there is no significant difference in the accuracies with and without noise rejection.

4.2.3 Results of the Moving Dipole Fits

The second inverse method applied to the phantom data is the moving dipole fit. As reference data the measured data with and without noise rejection by means of 3rd order synthetic gradiometers is used. To use an inverse method on data with applied noise rejection this noise rejection has to be taken into account in the forward computation of the magnetic flux. Therefore the CTF noise rejection technique first had to be implemented into the FEM forward computation in NeuroFEM, which was part of the work for this diploma thesis.

The projections on the x-z-plane and the y-z-plane of the reconstruction results for the moving dipole fit with and without applied noise rejection in comparison to the two reference dipole positions are shown in figures (4.8) respectively (4.9).

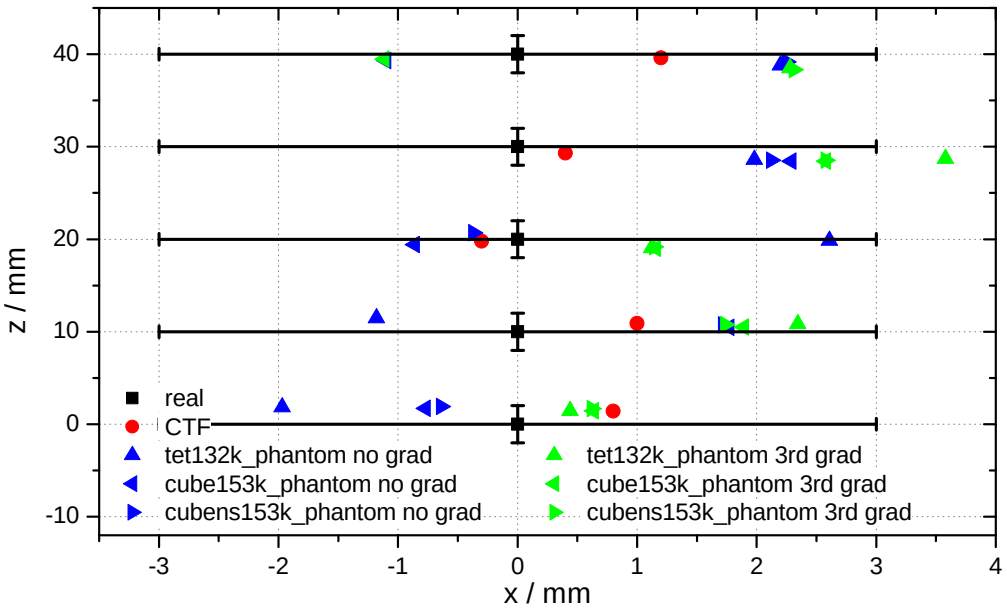

Figure 4.8: Localisation results for moving dipole fits on data with and without noise rejection in the three FEM meshes projected on the x-z-plane. The label *real* marks the directly measured dipole positions. The label *CTF* marks the CTF reconstruction results.

Again, to quantify the localisation results, the euclidean distance to the references is calculated. These mislocalisations relative to the directly measured dipole positions are presented in figure (4.10). The distances between the FEM reconstruction results and the CTF reconstruction results can be found in figure (4.11). The maximum distance

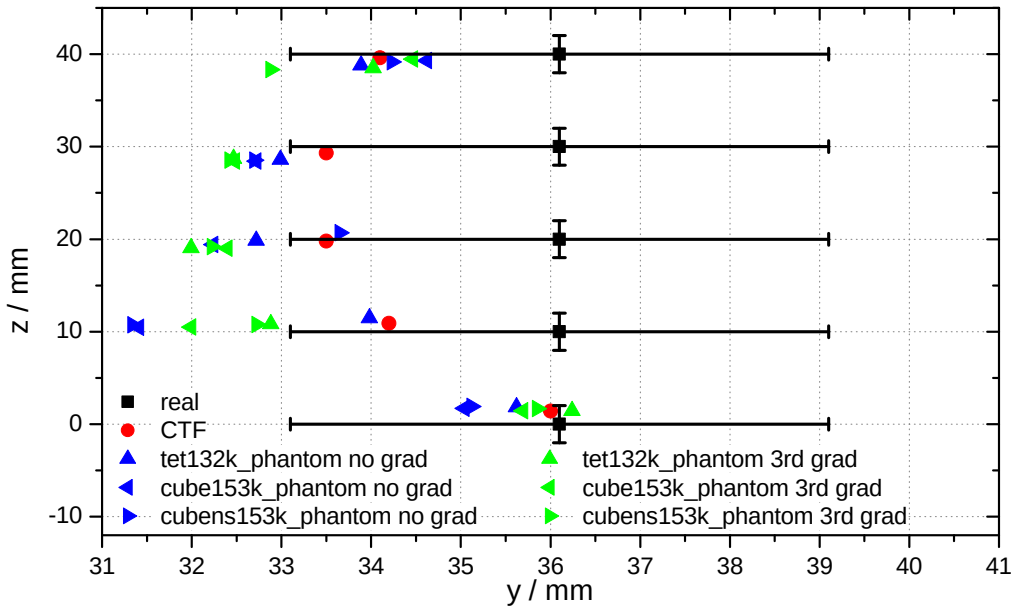

Figure 4.9: Localisation results for the moving dipole fits on data with and without noise rejection in the three FEM meshes projected on the y-z-plane. The label *real* marks the directly measured dipole positions. The label *CTF* marks the CTF reconstruction results.

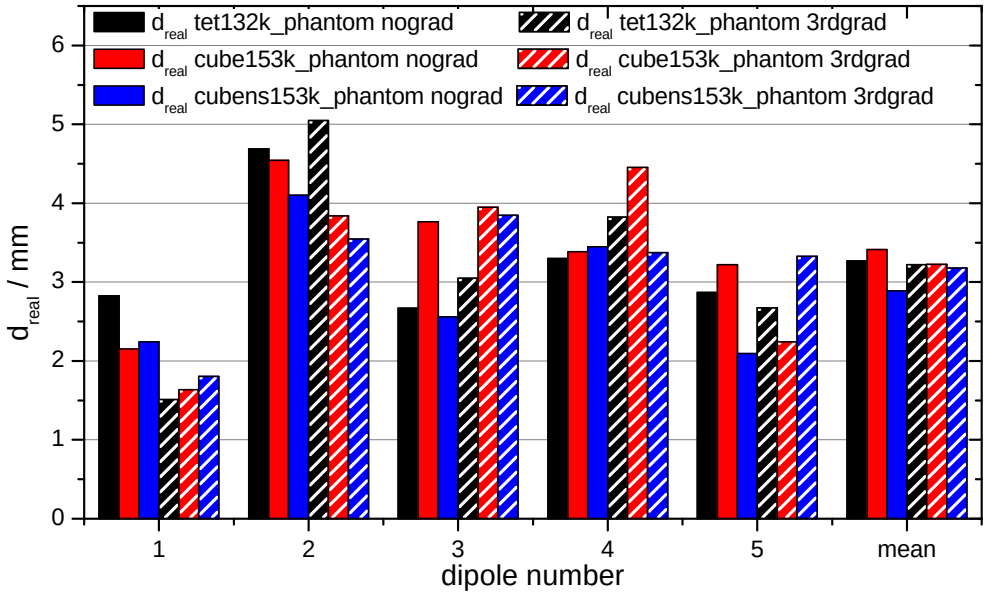

Figure 4.10: Euclidean distance between the reconstruction results from the moving dipole fits and the directly measured dipole position.

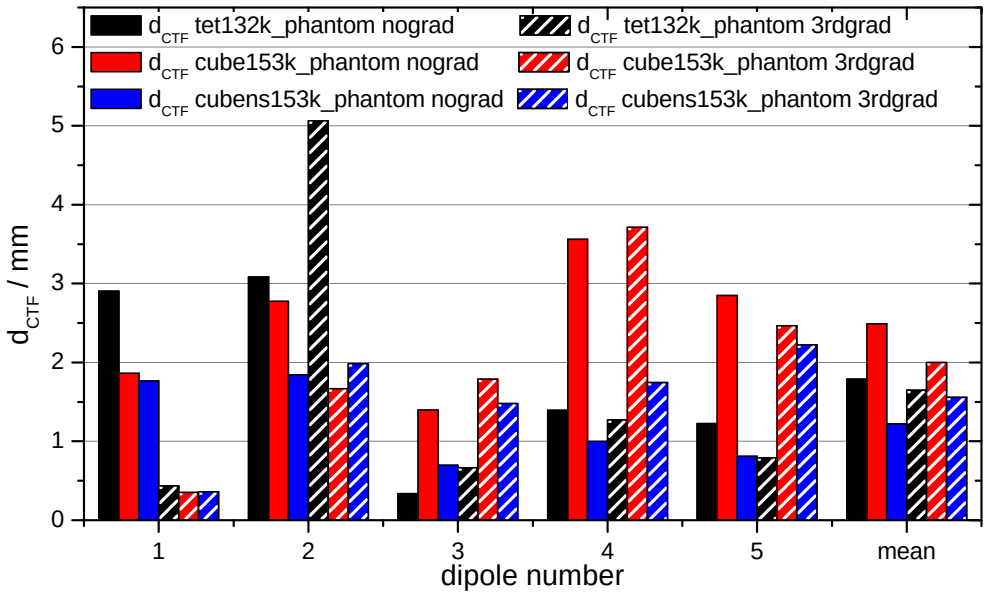

Figure 4.11: Euclidean distance between the reconstruction results from the moving dipole fits and and the reconstruction results from the CTF software.

between the reconstruction results from the moving dipole fits and the directly measured dipole positions is below 5.0 mm. The maximum distance to the CTF results is, except for one outlier, even below 4.0 mm. The mean localisation errors are around 3.0 mm relative to the directly measured dipole positions and below 2.5 mm relative to the CTF reconstruction results.

For the moving dipole fits not only the reconstructed positions of the dipoles, but also the reconstruction results for the dipole orientations will be presented. The orientation is given by the two angles φ and ϑ. φ is the angle between the projection of the dipole orientation vector on the x-y-plane and the x-axis. And ϑ is the angle between the dipole orientation vector and the z-axis. Figures (4.12) and (4.13) show the absolut values of the differences between the angles from the moving dipole fit and the angles measured directly at the phantom. Again, the reconstruction results from the commercial and well tested software from CTF is used as another reference for the moving dipole fit results. In figures (4.14) and (4.15) the absolute values of the differences between the by CTF reconstructed results and the angles from the moving dipole fits are shown. The maximum of the difference between the moving dipole fit reconstruction results for φ and the directly measured angle φ is approx. 6°, the difference to the CTF result is except for an outlier at 8° even below 5°. The mean values for the differences to the directly measured angle φ is below 3.5° and to the CTF results below 2.5°.

For the angle ϑ the maximum of the differences to the directly measured angle is around 6.5° and the difference to the CTF result is less than 3°. The average value of the differences of ϑ to the directly measured angle is around 3.5° and the average value

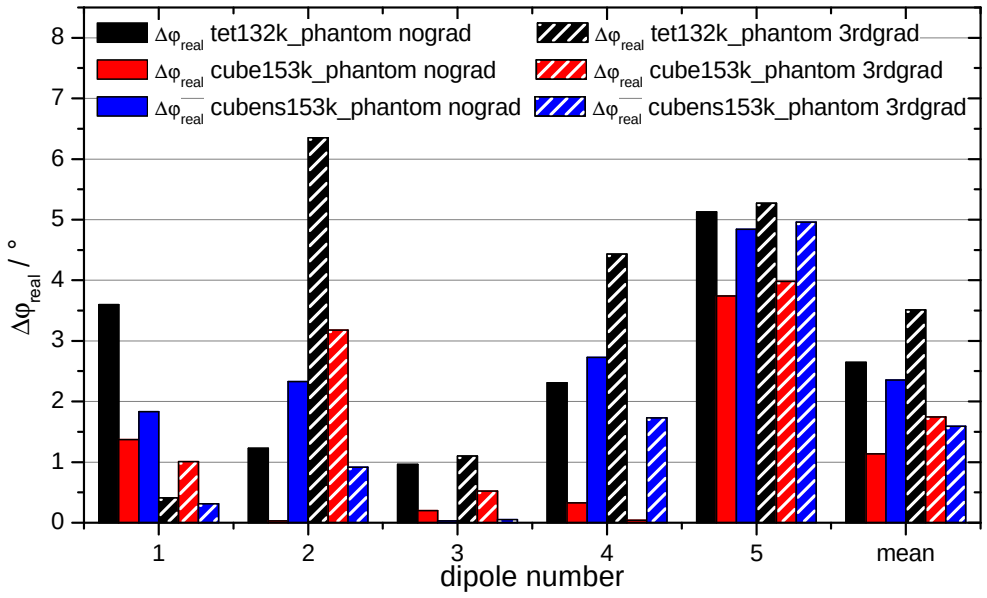

Figure 4.12: Absolute values of the differences between the directly measured angles φ and the moving dipole fit results for φ.

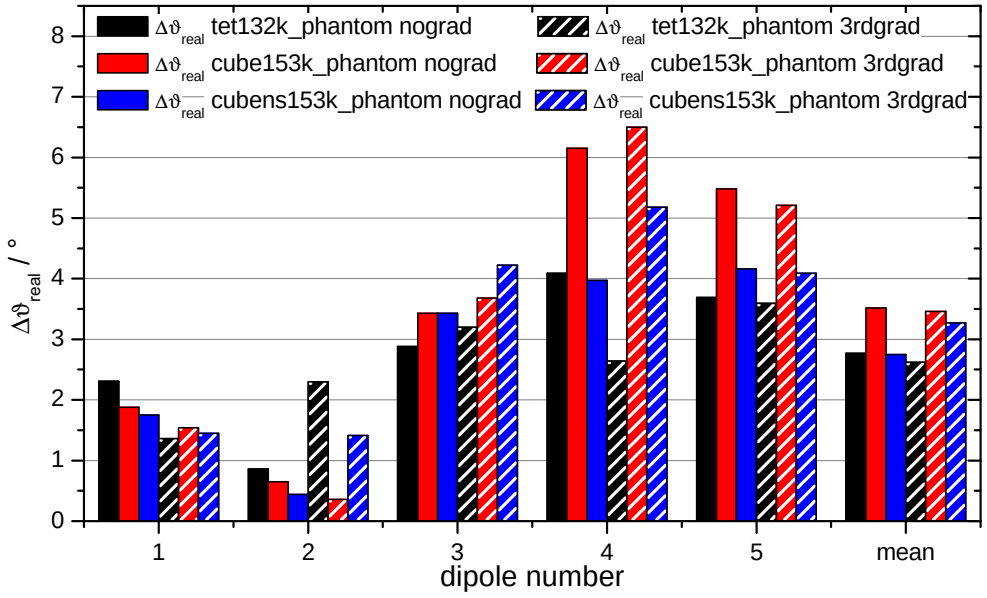

Figure 4.13: Absolute values of the differences between the directly measured angles ϑ and the moving dipole fit results for ϑ.

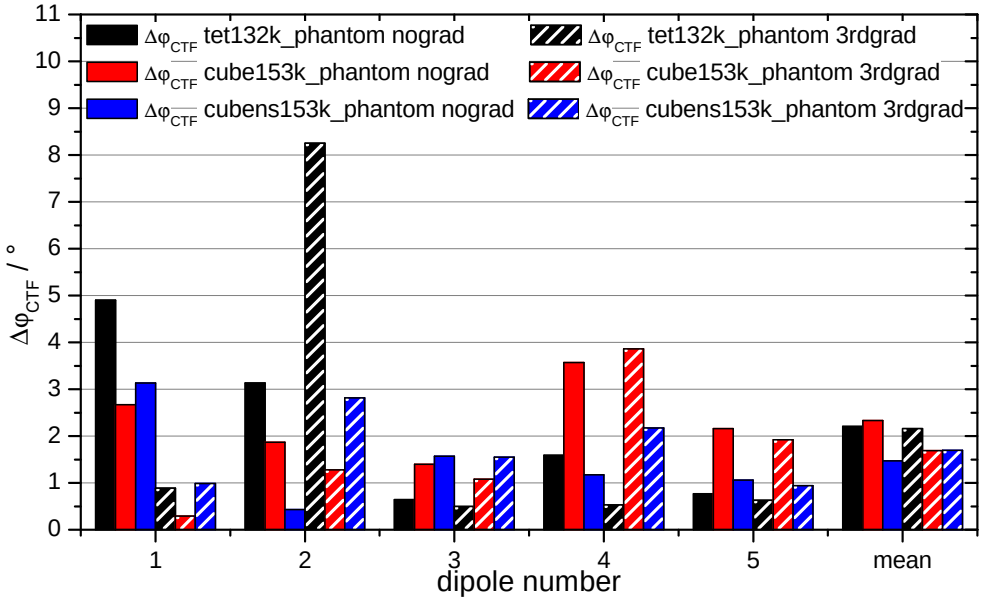

Figure 4.14: Absolute values of the differences between the CTF reconstruction results for φ and the moving dipole fit results for φ.

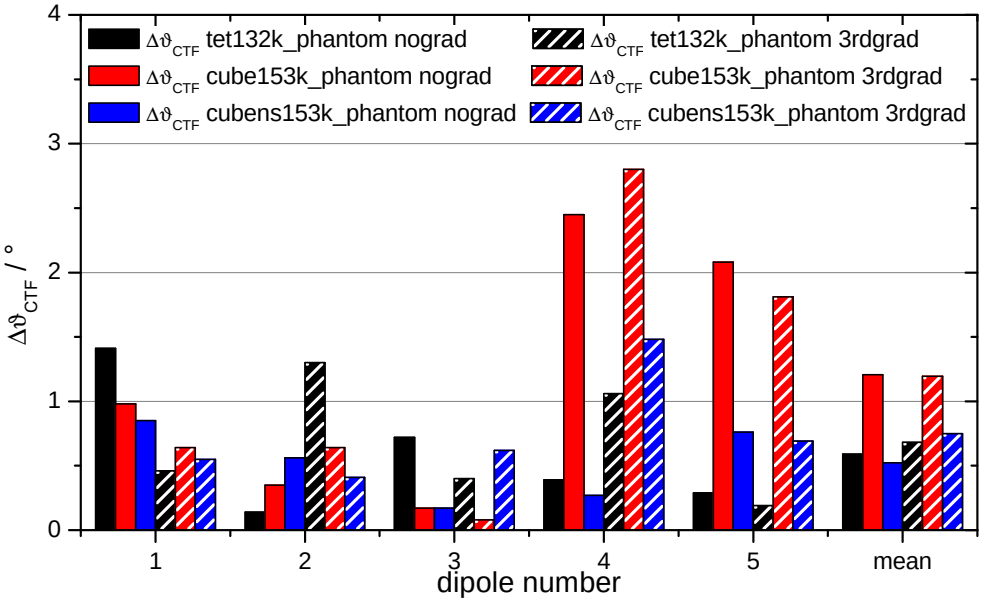

Figure 4.15: Absolute valuse of the differences between the CTF reconstruction results for ϑ and the moving dipole fit results for ϑ.

of the differences to the reconstruction results by CTF is below 1.5°.

4.2.4 Discussion of the Moving Dipole Fit Results

The localisation errors for the moving dipole fits are even lower than the errors of the goal function scans. One reason for this is that the resulting dipole positions for a goal function scan can only lie on a node of the finite element mesh. For the moving dipole fit the position of the dipole is continously optimized. In agreement with the results of the multilayer sphere studies the nodeshifted hexahedra mesh allows the most accurate results for the moving dipole fits. But tetrahedra and regular hexahedra perform only slightly worse.

As for the results of the goal function scans using 3rd order synthetic gradiometers does only improve the localisation errors for deep dipoles. The average localisation errors across all five dipoles are nearly the same with and without noise rejection. This result, that the noise rejection using 3rd order synthetic gradiometers does not improve the localisation accuracy, can hardly be transfered to realistic measurements. Realistic measurements are affected by brain noise and other noise generated by the human body. Furthermore often only a few trials, much less than the 100 trials of the phantom study, can be recorded and averaged. So for a realistic measurement the higher noise level when not using noise rejection with 3rd order synthetic gradiometers could cause higher localisation errors than the location errors caused by higher numerical error in the forward computation of the signal for the synthetic 3rd order gradiometers.

The orientations of the current dipoles could be accurately reconstructed in the moving dipole fits, although it is widely known that the reconstruction of the dipole orientation is hard using only MEG data, because a radial dipole in a nearly spherical volume conductor generates only a very small field[3].

5 Validation in a Realistic Head Model

In chapter (3) the forward computations in a multilayer sphere model using the finite element method were validated and compared to another numerical solution, the boundary element method. In the application of EEG and MEG source reconstruction the forward problem has to be solved for more complex volume conductors than only spheres. The big advantage of FEM is that it is not limited to simple geometries, but it can handle arbitrary complex volume conductors. That this can be done with high accuracy will be shown in this chapter by applying the finite element method to the forward and the inverse problem in a realistic volume conductor. In addition the accuracy of the FEM solutions will be compared to the accuracy of the competing boundary element method.

5.1 Methods

This section describes the methods used for the validation of FEM on forward and inverse computations in the realistic head model. The dipoles, chosen for the simulations, and the sensor configurations will be presented briefly. In addition it is described how the FEM and BEM meshes were generated.

5.1.1 Current Dipoles and Sensor Configurations

For the finite element validation studies in the realistic volume conductor dipole sources at 16 locations were used. The locations were chosen manually in different anatomical regions of the brain. Dipoles were placed in the frontal, the temporal, the parietal and the occipital lobe of both hemispheres. For every lobe one dipole was in a gyrus and another one was placed in a sulcus. The dipoles were lying on a surface approx. 3 mm below the surface of the cortex. In the multilayer sphere studies the dipole orientations were chosen radially and tangentially to the surface of the volume conductor.

For a realistic volume conductor in general no radial or tangential direction can be defined. So the orientations of the dipole were chosen in another way. First the magnetic flux density at the 275 measurement sensors was simulated for 3 orthogonal dipoles orientated along the coordinate axes with unit strength at one of the 16 locations. The simulations were performed using FEM and the Venant approach in the tet802k_4layer_aniso mesh. A lead field matrix $\mathbf{L}$ can now be constructed from the simulated magnetic flux. The element L_{ij} of the lead field matrix is the flux simulated at the i-th sensor for the j-th dipole. A singular value decomposition (SVD) is then applied to the lead field matrix. This yields singular values σ_i and main axes $\mathbf{u}_i$. A current dipole orientated in the direction of the main axis $\mathbf{u}_j$ which belongs to the smallest singular value σ_j produces the weakest signal at the sensors compared with all other directions. Whereas a dipole pointing in the direction of the main axis with the highest singular value generates the

strongest magnetic flux at the sensors. For the MEG it is known that a radial dipole in a spherical volume conductor produces the weakest field outside of the sphere, that is none at all. So the direction of the main axis with the smallest eigenvalue is defined as quasi-radial. The directions of the other two orthogonal axes are then called quasi-tangential. In the validation studies for the realistic head model a quasi-radial dipole and two quasi-tangential dipoles at each of the above described 16 locations were used. All the dipoles are shown in figure (5.1).

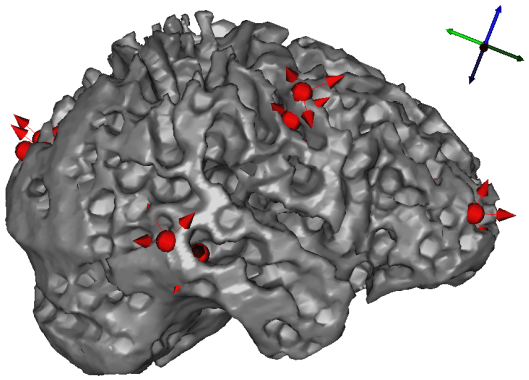

Figure 5.1: The dipoles used for the validation studies in the realistic head model. View on the right hemisphere. Some dipoles are hidden in the sulci.

The realistic volume conductor which is used for this study was taken from the experiment on somatosensory evoked potentials respectively fields (SEP respectively SEF) described in chapter (6). Therefore the EEG and MEG configuration for this study was also taken from that experiment. In figure (5.2(a)) the 63 electrodes are shown together with the potential distribution on the scalp of the realistic head model simulated for a dipole in the left occipital lobe. In figure (5.2(b)) the centres of the inner coils of the measurement gradiometers of the used MEG configuration can be seen. Isopotential lines indicate the magnetic flux density simulated for a dipole in the left occipital lobe. As for the EEG the realistic MEG configuration was taken from the SEP/SEF experiment.

5.1.2 Generation of the FEM and BEM Meshes

The realistic volume conductor used in this study is assumed to consist of four compartments with different conductivities: the scalp, the skull, the liquor and the brain. Scalp, liquor and brain are modelled with the isotropic conductivity values 0.33 S/m, 1.79 S/m and 0.33 S/m respectively. According to recent measurements[1] the tangential conductivity of the skull is chosen ten times larger than the radial skull conductivity. So the radial conductivity of the skull is 0.0042 S/m and the tangential conductivity is 0.042 S/m.

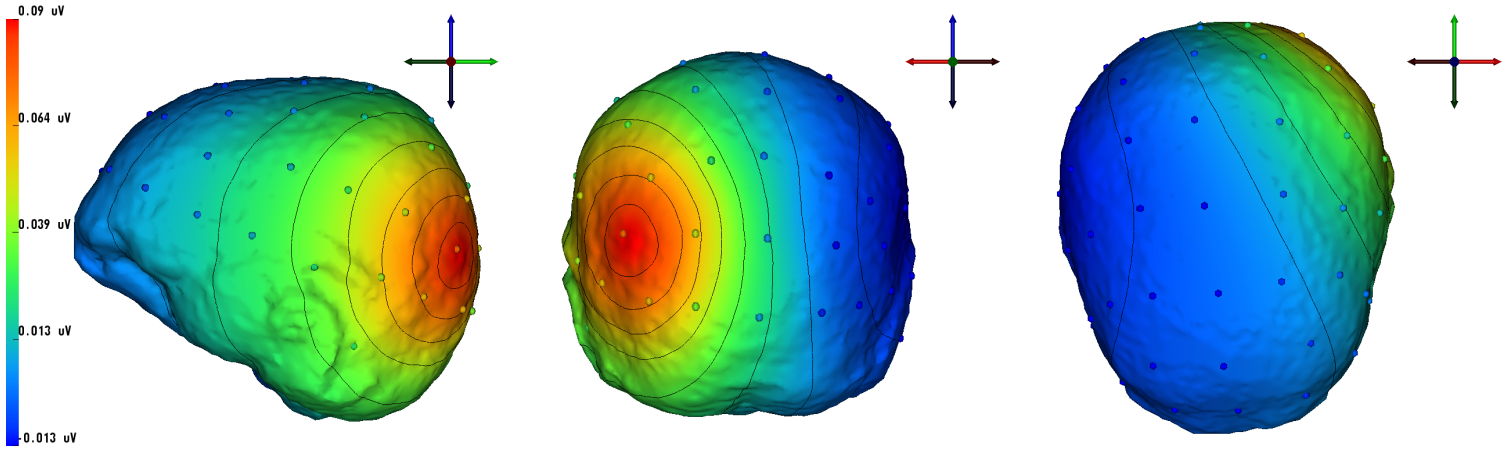

(a) EEG sensor configuration.

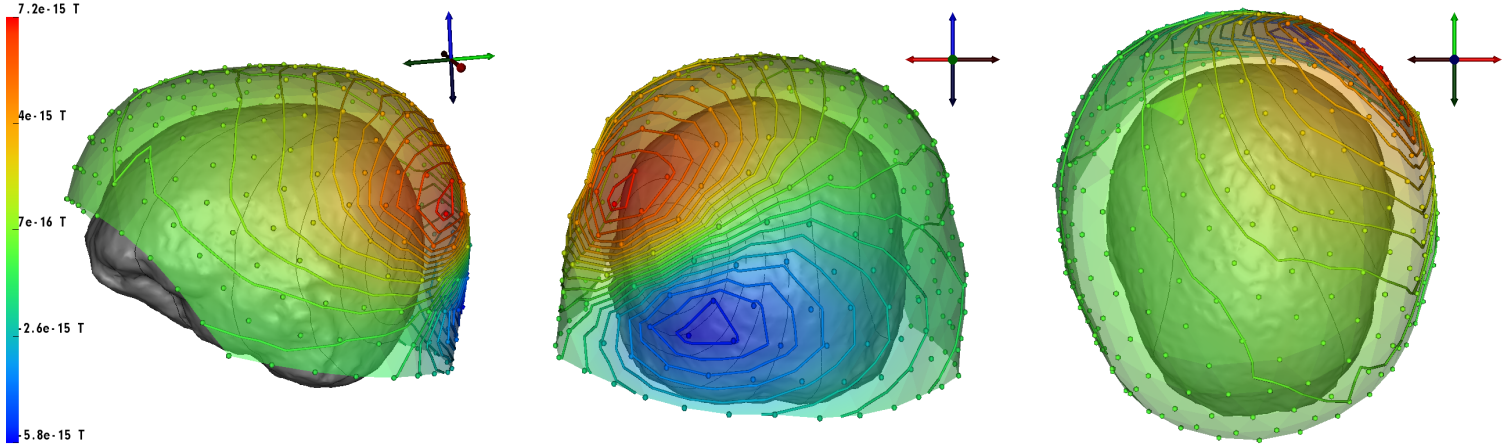

(b) MEG sensor configuration.

Figure 5.2: The sensor configurations used for simulations in the realistic volume conductor.

To simulate the electric potential and the magnetic flux for sources in the realistic head model using FEM first the geometry of the volume conductor was discretised. As in the previous studies different element types were used.

To create the tetrahedra model tet178k_4layer_aniso first a real subjects MR image was segmented in CURRY. Then a tetrahedra mesh with tetrahedra of an average edge length of approx. 2 mm was generated using a ordinary Delaunay tetrahedralisation which was described in section (2.6.1). A regular, cube386k_4layer_aniso, and a nodeshifted hexahedra mesh, cubens386k_4layer_aniso, were built using VGRID. As for the tetrahedra mesh the first step for the hexahedra mesh generation is to segment a MR image. The cube meshes are then built using the procedure explained in section (2.6.1).

It was shown in the validation studies for the multilayer sphere models that in a locally refined mesh with high quality tetrahedra elements more accurate FE simulations can be performed. This is why also for the realistic head model such a mesh was built. The mesh, tet802k_4layer_aniso, was generated by first segmenting the MR image and creating triangle meshes of the compartment boundaries in CURRY. With the software tool TetGen then a tetrahedra mesh was constructed employing the constrained Delaunay tetrahedralisation (see section (2.6.1)). The simulation results for the in this way generated mesh using FEM and the Venant approach can be expected to be most accurate and are therefore chosen as the reference solution for this section.

A difficult point in the generation of all FEM meshes is the determination of the anisotropic conductivity tensors of the skull[35]. To determine the conductivity tensor for a skull element first the directions (quasi-)radial and (quasi-)tangential to the skull surface have to be known. These are calculated as follows: A smooth and fine triangle surface mesh lying in-between the inner and the outer skull surface is constructed. For each of the skull elements then the triangle of the mesh is searched which barycentre is closest to the barycentre of the skull element. The (quasi-)radial direction at the location of the finite element is then defined as the normal of this closest triangle. The (quasi-)tangential directions are chosen to form a right handed coordinate system. The diagonal conductivity tensor can finally be transformed into this coordinate system.

For the EEG and MEG simulations the same FEM meshes were used. Details on all the used FEM meshes can be found in table (5.1). In addition cuts through the FEM meshes are presented in figures (5.3(a)) to (5.3(d)).

The simulation of the electric potential and the magnetic flux using the boundary element method needs triangle meshes representing the compartment interfaces. For the EEG a three layer isotropic BEM model, with the boundaries scalp, outer skull and inner skull, was built to approximate the volume conductor. From the outside to the inside the conductivities 0.33 S/m, 1.79 S/m and 0.33 S/m are assigned to the three BEM compartments. Anisotropy cannot be modelled with BEM. Furthermore with common BEM simulators it is, due to the computational effort which would be needed, not possible to simulate the EEG or MEG in a four layer BEM model. The MEG was simulated with BEM using a one layer model. The surface of the one layer model is the inner skull surface and the conductivity of the brain is chosen to be 0.33 S/m.

For the BEM mesh generation CURRY was used to first segment the MR image and then build the triangle surface meshes using the procedure outlined in section (2.6.2).

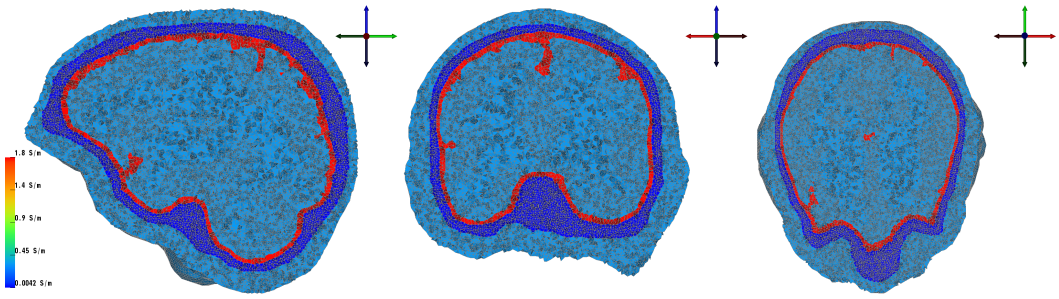

(a) tet802k_4layer_aniso

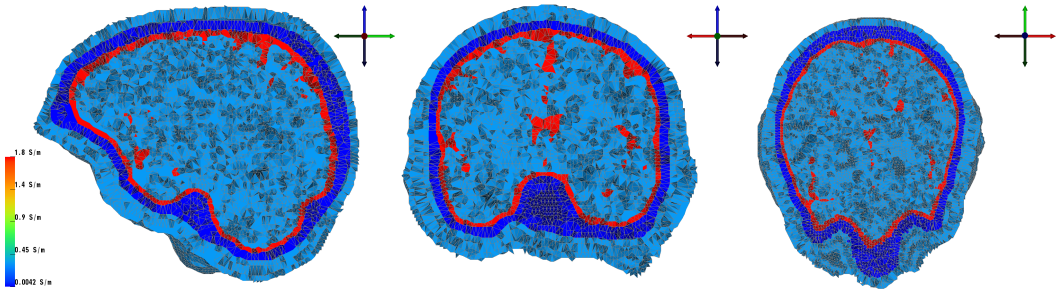

(b) tet178k_4layer_aniso

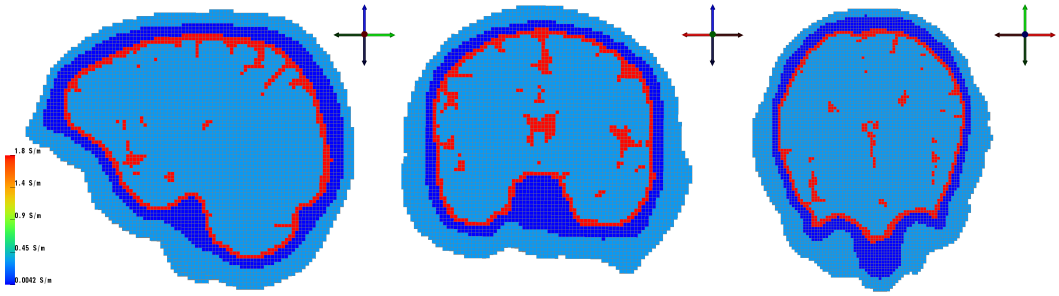

(c) cube386k_4layer_aniso

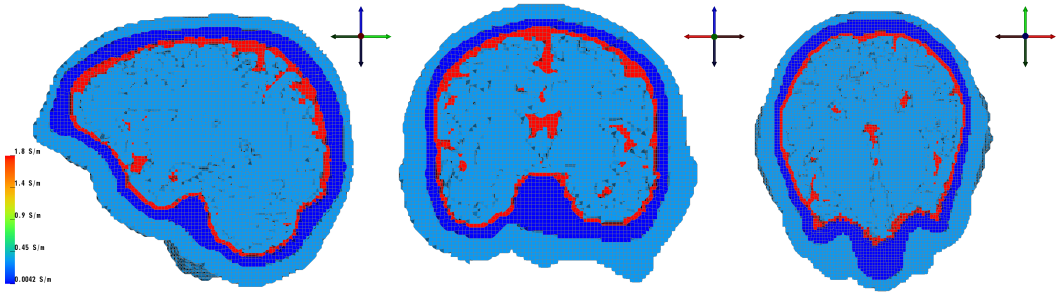

(d) cubens386k_4layer_aniso

Figure 5.3: Cuts through the FEM meshes. Figures show x-, y- and z-section from left to right.

	element type	element size	# nodes	# elements
EEG/MEG				
tet802k_4layer_aniso	tetrahedra	n.a.	802480	5073061
tet178k_4layer_aniso	tetrahedra	2.0 mm	177762	1084103
cube386k_4layer_aniso	hexahedra, regular	2.0 mm	385901	366043
cubens386k_4layer_aniso	hexahedra, nodeshifted	2.0 mm	385901	366043

Table 5.1: The FEM meshes of the realistic head model.

	element width			# nodes	# elements
	scalp	outer skull	inner skull		
EEG					
BEM4000_3layer_iso	10.0 mm	9.0 mm	7.0 mm	3970	7982
MEG					
BEM1600_1layer_iso	n.a.	n.a.	7.0 mm	1596	3188

Table 5.2: The BEM meshes of the realistic head model.

Details on the used BEM meshes can be found in table (5.2).

5.2 Validation on the Forward Problem

To validate the FEM solutions for a realistic head model the electric potential and the magnetic flux is simulated for the different FEM meshes using Venant's approach. The simulated fields and potentials are then compared to a reference solution. Unlike for the multilayer sphere validation studies for the realistic head model no real reference solution exists. For this reason the solution which proved to be most accurate in the multilayer sphere studies, that is the FEM solution in a locally refined mesh with high quality tetrahedra, is chosen as the reference solution. In addition BEM simulations were performed using BEM models that are similar fine as the BEM models which delivered the most accurate results in the multilayer sphere models.

5.2.1 Results and Discussion of the Validation on the Forward Problem

Figures (5.4) and (5.6) show the RDMs and figures (5.5) and (5.7) show the MAGs between the reference solution in the tet802k_4layer_aniso mesh and the solutions for

the other FEM meshes and BEM. The errors are not shown separately for all 48 dipoles. First the errors of the solutions for the two tangential dipoles at one location were averaged. And in addition the errors of the solutions for dipoles at symmetrical positions were averaged. So only the influence of the placement of a dipole on a gyrus or in a sulcus and of the used element types and numerical methods on the RDM and MAG are studied.

Obviously the errors of the numerical forward simulations in a realistic head model are larger than the errors that were found for the multilayer sphere models at a comparable eccentricity. One reason for this is that for the realistic head model no exact reference solution exists. It is clear that there is a error between the here used reference solution and the unknown real solution. So the RDM and MAG values have to be interpreted carefully. This even gets more obvious when looking at the cuts through the FE meshes in figures (5.3(a)) to (5.3(d)). The figures indicate that the deep sulci of the cortex are not accurately described by the tet802k_4layer_aniso reference mesh, which could cause additional errors between the reference solution and the other FEM solutions. An influence of this error in modelling the CSF can especially be observed in the RDMs and MAGs for the EEG.

When comparing the RDMs and MAGs of the EEG solutions for dipoles located in a gyrus and in a sulcus then it can be observed that for the vast majority of dipoles the errors are larger for dipoles lying on a gyrus. This is because these dipoles are closer to the conductivity jump between the CSF and the skull. As seen in the multilayer sphere studies for dipoles close to a discontinuity of the conductivity the errors increase.

For the comparison of the different FEM and BEM EEG solutions it can be stated that FEM, not depending on the element type, is more accurate. This is very obvious when looking at the average magnitude error. The larger errors for BEM result from the fact that for the BEM simulations the CSF layer and the anisotropy of the skull is ignored. It was already shown in the multilayer sphere studies that this causes errors at approximately the same level as observed here. From all FEM solutions the solution in the nodeshifted hexahedra model delivers the best results. This, too, is consistent with the results from the simulations in the spherical volume conductors.

The errors for the MEG are in general lower than those observed for the EEG and at approx. the same level as in the multilayer sphere MEG studies. Apparently the primary magnetic flux, which does not depend on the shape or conductivity profile of the volume conductor, still dominates the total magnetic flux simulated at the gradiometers which is understandable as it was shown in section (3.2.3) for the here used MEG sensor configuration that the primary magnetic flux still contributes more to the total magnetic flux than the secondary magnetic flux. Like for the EEG the errors for dipoles in sulci and in gyri can be compared. But unlike for the EEG there is no significant difference between the errors for dipoles at the two locations. Again this can be explained by the dominating primary magnetic flux which is not sensitive for the conductivity profile of the volume conductor. For the MEG simulations in the realistic head model it can be noticed that the errors of the FEM simulations are at an equal level. The BEM solution is less accurate, but the difference is not as large as for the EEG.

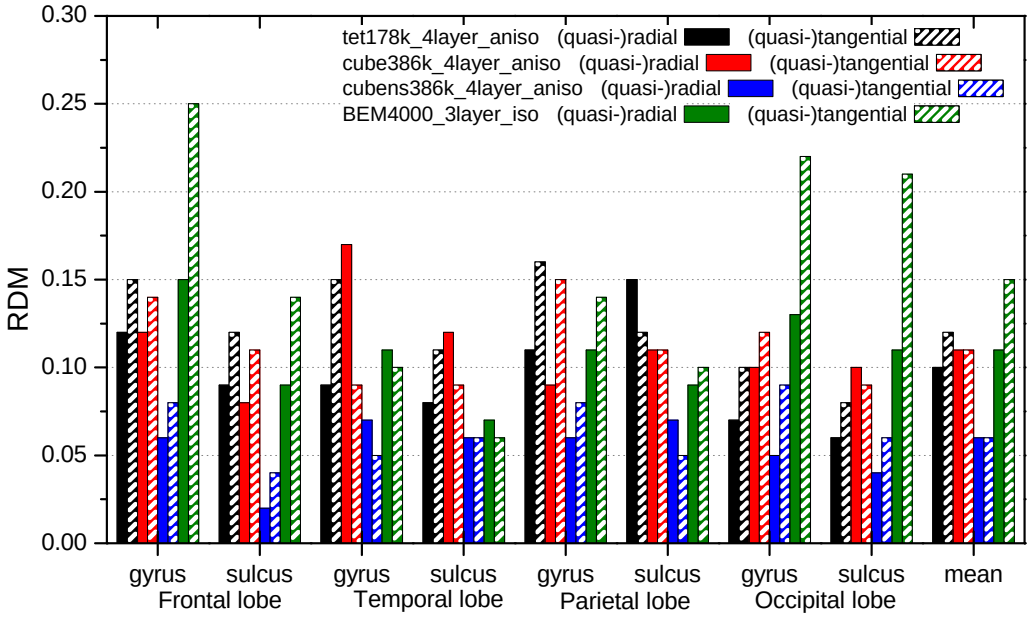

Figure 5.4: The RDMs of the FEM and BEM EEG solutions.

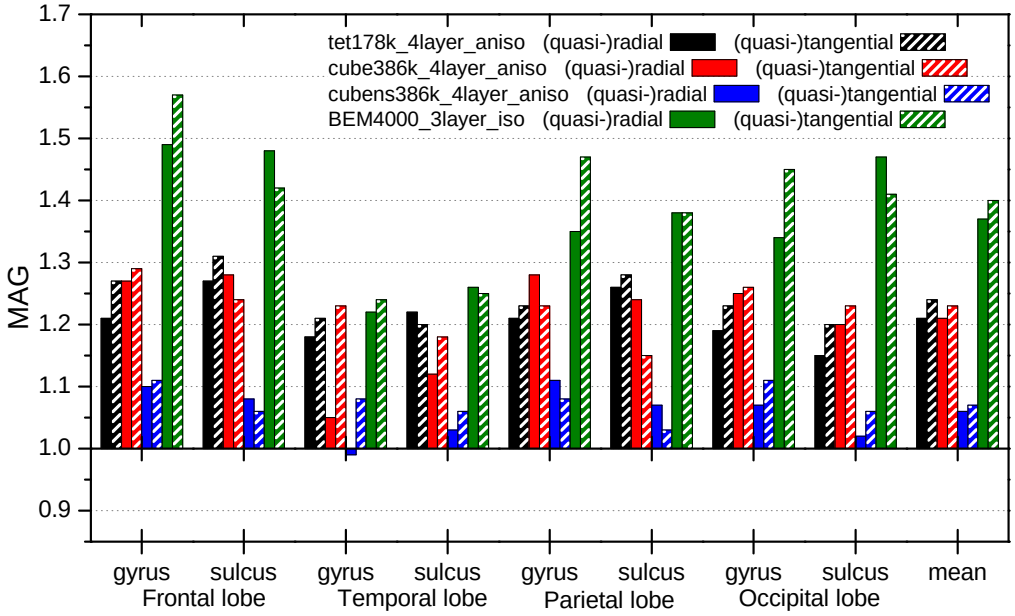

Figure 5.5: The MAGs of the FEM and BEM EEG solutions.

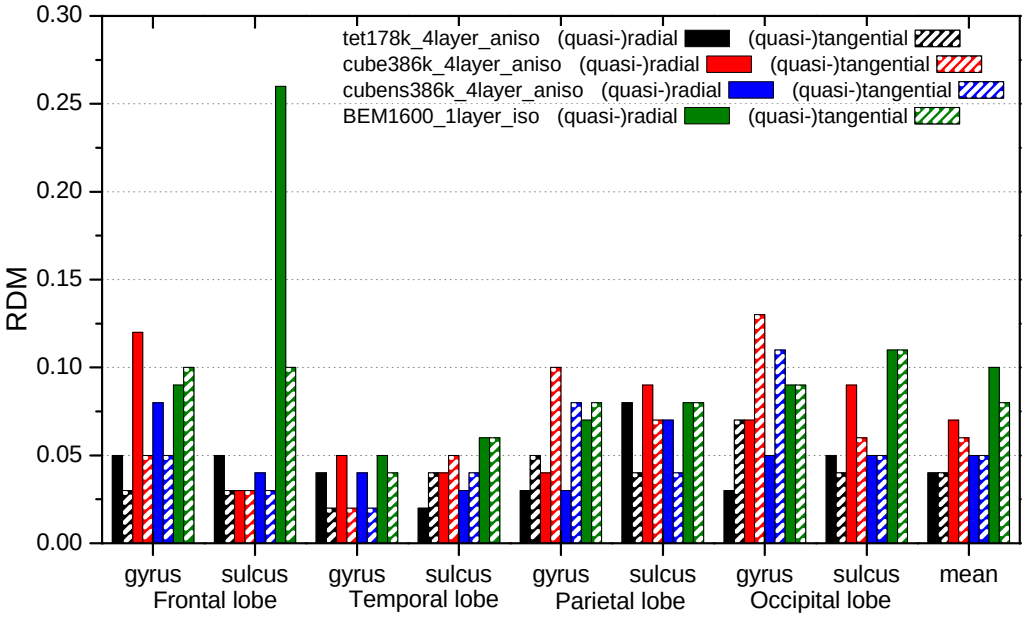

Figure 5.6: The RDMs of the FEM and BEM MEG solutions.

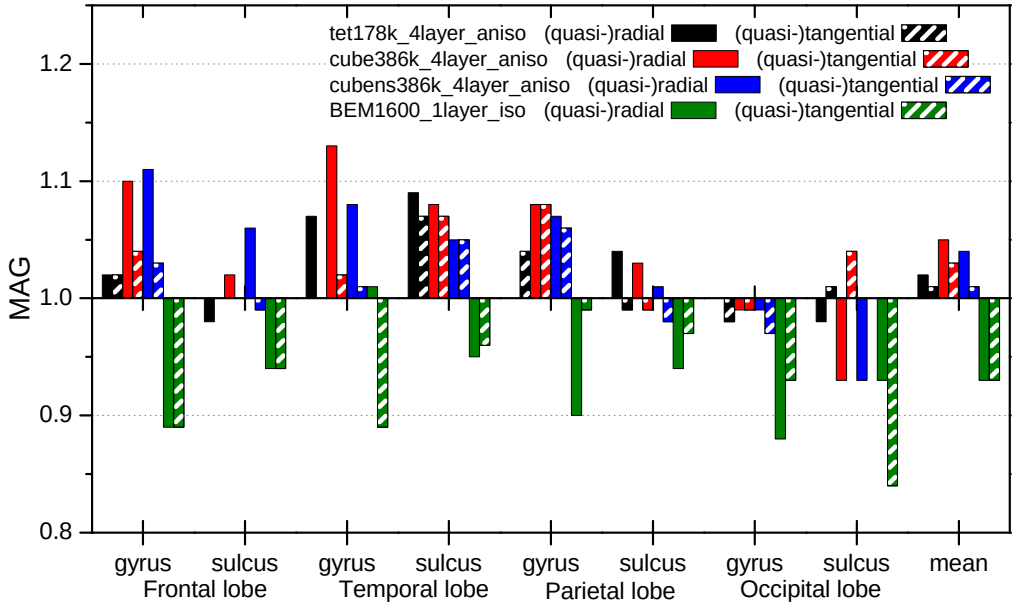

Figure 5.7: The MAGs of the FEM and BEM MEG solutions.

5.3 Validation on the Inverse Problem

For the realistic head model not only the errors of the forward solutions are studied. But also moving dipole fits using the FEM solutions in the different meshes and the BEM solution were applied to synthetic reference data. The synthetic reference data was produced by simulating the electric potential and the magnetic flux for the 48 dipoles at 16 locations presented above using the finite element method and Venant's approach in the locally refined, high quality tetrahedra mesh tet802k_4layer_aniso.

The moving dipole fits were performed as described in section (2.9). To reliably find the source distribution which best explains the measured data the moving dipole fit for each dipole was repeated using four different sets of initial parameters, i.e. locations, for the optimizer. These starting points were distributed in the left and right hemisphere and in the front and back of the brain. The result of the moving dipole fits which best explains the measured data is then chosen as the reconstruction result.

5.3.1 Results and Discussion of the Validation on the Inverse Problem

As above the reconstruction results are not discussed separately for all 48 dipoles. But the results for the (quasi-)tangential directions and symmetrical positions in the brain are averaged. The solution of the inverse problem with FEM and BEM in the different meshes is then validated by looking at the euclidean distance between the reconstructed dipole position and the reference dipole position. The reference dipole position is the position of the dipole the synthetic reference data was simulated for. Figures (5.8) and (5.9) show the localisation errors of the moving dipole fits that were found for the EEG respectively the MEG.

When comparing the errors of the reconstruction results for the MEG and the EEG it can be observed, that the localisation errors for the MEG are 2 to 3 times smaller than the localisation errors for the EEG. This is consistent with the results of the studies on the forward problem in the realistic head model. There it could be seen that the RDMs for the EEG are larger than those for the MEG.

For the EEG the comparison between the localisation errors of the FEM solutions using different element types and the BEM solution shows that the FEM solution in the nodeshifted hexahedra mesh is able to most accurately reconstruct the dipole position. The mislocalisations of the other solutions are at least twice as large. BEM produces for the EEG localisation errors that are comparable to those of the FEM solution in the tet178k_4layer_aniso mesh.

Looking at the results of the moving dipole fits on the MEG data one can see that the three FEM solutions perform at a similar level of accuracy. Only the BEM solution estimates the dipole location around twice as far away from the reference position.

All these findings for the comparison of the element types and BEM and FEM very well confirm what was observed for the RDMs in the forward simulations for the realistic head model. This indicates that the RDM of the forward simulations is correlated to the localisation errors of the moving dipole fits.

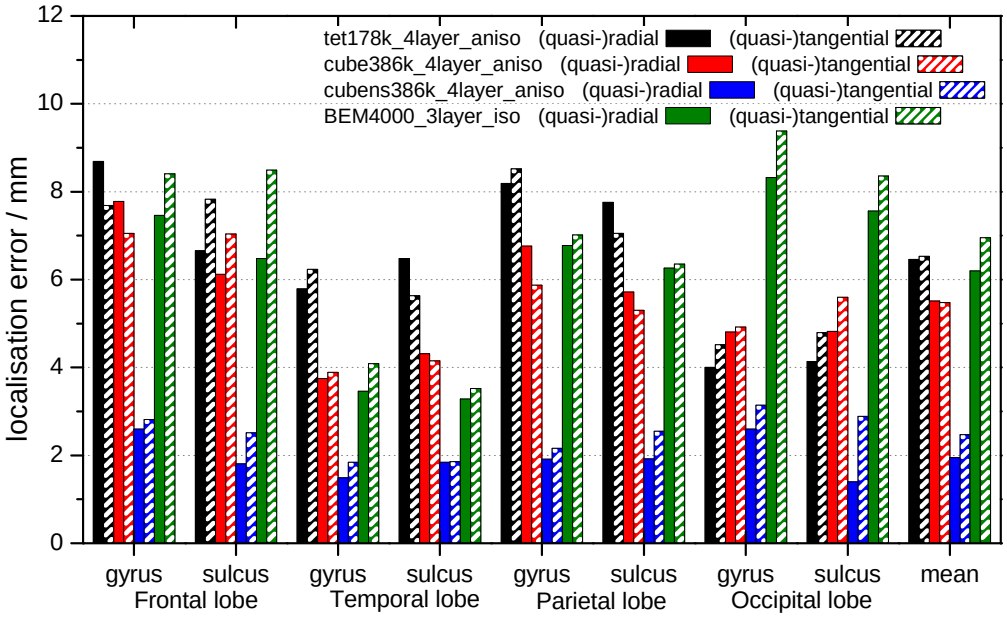

Figure 5.8: The localisation errors for the moving dipole fits on the synthetic EEG reference data.

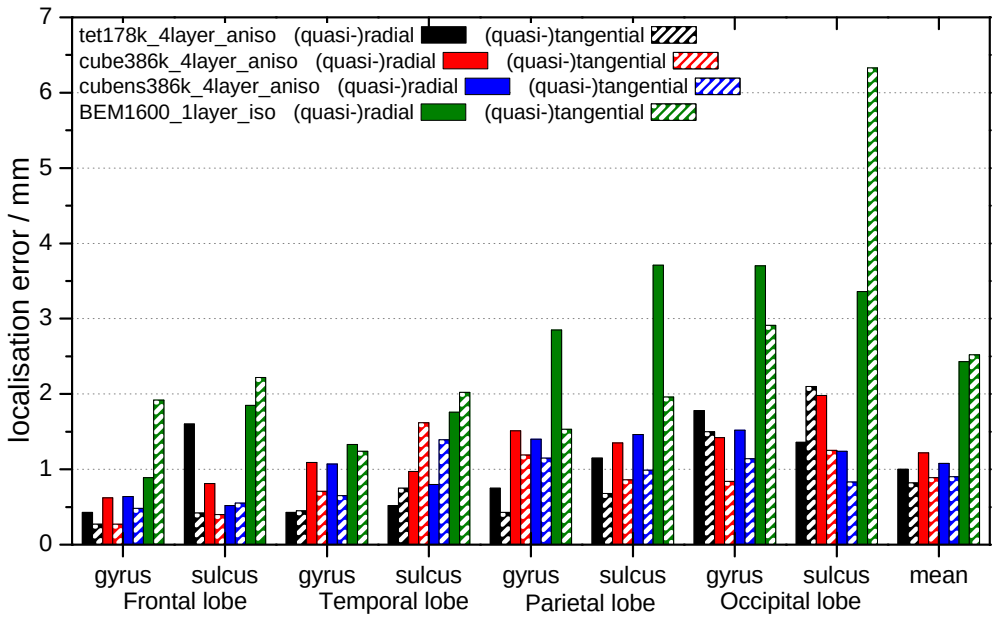

Figure 5.9: The localisation errors for the moving dipole fits on the synthetic MEG reference data.

6 Application of the Finite Element Method to a SEP/SEF Experiment

After having the finite element method validated on more or less artificial data in the previous chapters, now the method is applied to data recorded for a real neurophysiological experiment. Moving dipole fits on the EEG and MEG measured during a somatosensory experiment using the finite element method for the forward computations are used to solve the inverse problem. It is then evaluated if the reconstructed current density distributions are anatomically reasonable to see if the finite element method can be used to solve the inverse problem for realistic data.

6.1 Methods

First of all in this section the somatosensory experiment will be described. Then data acquisition and preprocessing will be explained. Finally information on the used sensors and FEM meshes will be given.

6.1.1 The Somatosensory Experiment

In the somatosensory experiment the index finger of the subject's right hand was stimulated. This stimulation was done by a pneumatically driven membrane which pressed the finger when triggered. While the stimulation was delivered to the subject the EEG and MEG were recorded with a sampling rate of 1.2 kHz. In addition the time when the stimulation was triggered was recorded. One measurement run consisted of 62 trials, i.e. 62 repetitions of the stimulus. For the MEG one and for the EEG three runs were done.

A problem in EEG measurement are movements of the eyes. The muscles moving the eyes cause large artefacts. For this reason the activitiy of the eye muscles is measured with two additional electrodes which are placed on the skin directly above the muscled responsible for the horizontal and vertical movement of one eye. The signal of these electrodes was then monitored for eye movements and trials contaminated with artifacts were rejected.

All the trials of one run were then averaged to get a EEG and MEG signal with a good signal to noise ratio. For the EEG the signal was in addition averaged across the three recorded runs. After the averaging a lowpass filter at 45 Hz was applied. Furthermore a constant baseline correction is applied. In this way a EEG and MEG dataset with a signal to noise ratio of 19.9 respectively 16.6 are obtained. These averaged and filtered signals are shown in figures (6.1(a)) and (6.1(b)).

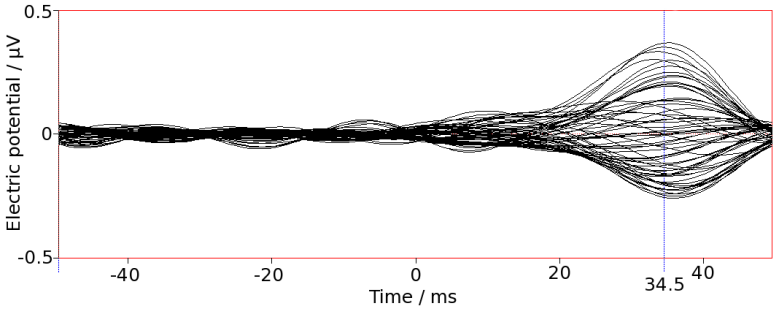

(a) EEG

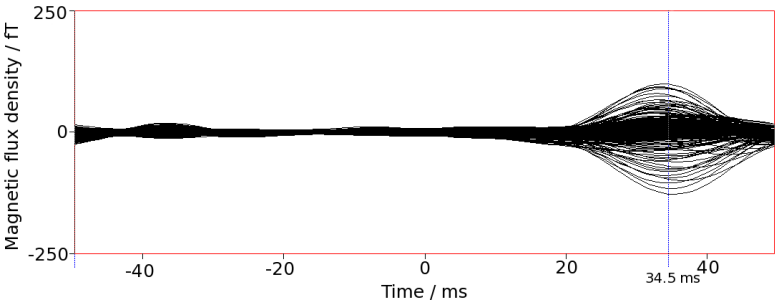

(b) MEG

Figure 6.1: The averaged and filtered EEG and MEG signals from the somatosensory experiment.

6.1.2 Sensor Configurations and FEM Meshes

The 63 channel EEG and the 275 channel MEG sensor configurations can be seen in figures (6.2(a)) and (6.2(b)). The electric potential resp. the magnetic flux measured at 34.5 ms, when the signal is at a maximum, are also shown in the figures.

6.1.3 Solving the Inverse Problem

For the SEP/SEF data it is assumed that the source distribution in the brain can be described by only one current dipole. Then a moving dipole fit is used to estimate the position, the moment and the magnitude of the dipole. The dipole fits were performed for four different starting points. From the four sets of dipole parameters that are obtained by the four fits the one set of parameters is chosen that best explains the data. The search volume for the fits was not constrained and the moving dipole fits on the EEG and MEG data were treated separately. The fits were used on the one sample of the data at 34.5 ms where the signal of the EEG and MEG is at a maximum.

6.2 Results and Discussion

The positions and orientations obtained from the moving dipole fits on the EEG data and the MEG data are illustrated in figure (6.3(a)) resp. (6.3(b)). It can be observed

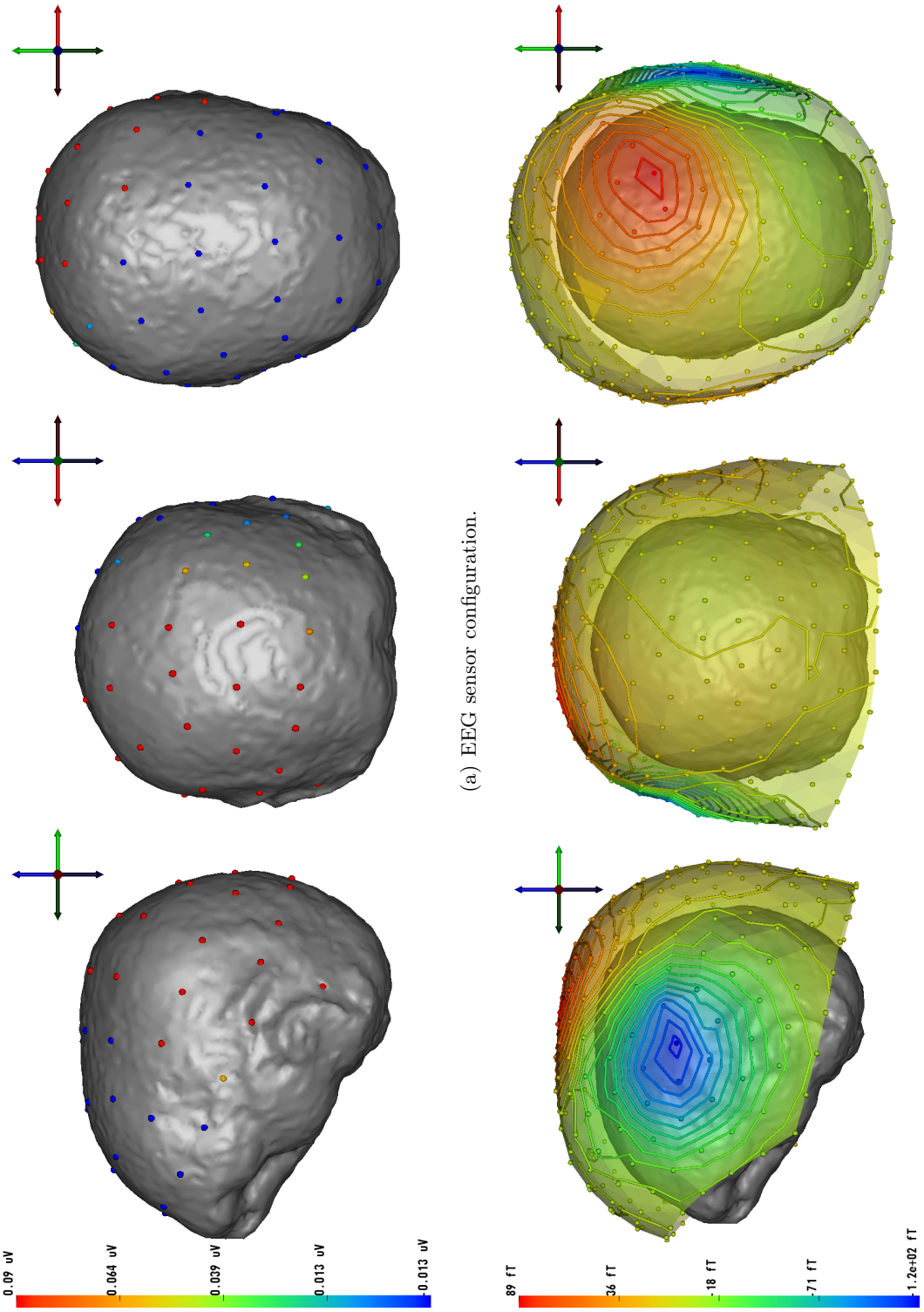

(a) EEG sensor configuration.

(b) MEG sensor configuration.

Figure 6.2: EEG and MEG sensor configurations displayed together with the electric potential respectively the magnetic flux at 34.5 ms

that the fits for all the FEM meshes yield plausible locations for the current dipoles. Although the search volume for the moving dipole fits was not constrained the dipoles are all lying inside the brain. In addition their locations are very close to or even in the cortex, where the activity of the brain for processing a somatosensory stimulus is expected.

When comparing the reconstruction results obtained from using the different FE meshes it can be noticed that there is a maximum mutual distance of 10.6 mm between the FEM EEG reconstruction results. For the MEG this maximum mutual distance between the reconstruction results is only 1.2 mm. Furthermore it is obvious for the EEG that the dipole location delivered by the fit using FEM in the nodeshifted hexahedra mesh is closest to the fit result using the locally refined, high quality tetrahedra mesh. These two observations are confirmed by the findings in the previous chapter. There it was shown that the localisation errors for the synthetic EEG data were higher than those for the MEG. And it was observed in the same study that the localisation error in the nodeshifted hexahedra mesh were smallest.

In figures (6.4(a)) and (6.4(b)) the localisation results for the EEG and the MEG using FEM in the cubens386k_4layer_aniso mesh respectively the tet802k_4layer_aniso mesh are compared. It is obvious that the moving dipole fits for the EEG and MEG do not reconstruct the current dipole at the same position. Between the two reconstruction results there is distance of 4.7 mm for the locally refined tetrahedra mesh and 3.9 mm for the nodeshifted hexahedra mesh. A possible reason for this could be an error in the modelling of the conductivity profile of the volume conductor. This will have a larger effect on the EEG than on the MEG, as the MEG is only weakly affected by small conductivity variations.

All in all it can be stated that from the data from the somatosensory experiment very well a resonable current density distribution could be reconstructed.

(a) EEG. Left, rear and top view.

(b) MEG. Left, rear and top view.

Figure 6.3: Localisation results of the moving dipole fits on the SEP and SEF data projected on a slice of the subject's MR image. Black arrow: tet178k_4layer_aniso. Red arrow: cube386k_4layer_aniso. Blue arrow: cubens386k_4layer_aniso. Orange arrow: tet802k_4layer_aniso.

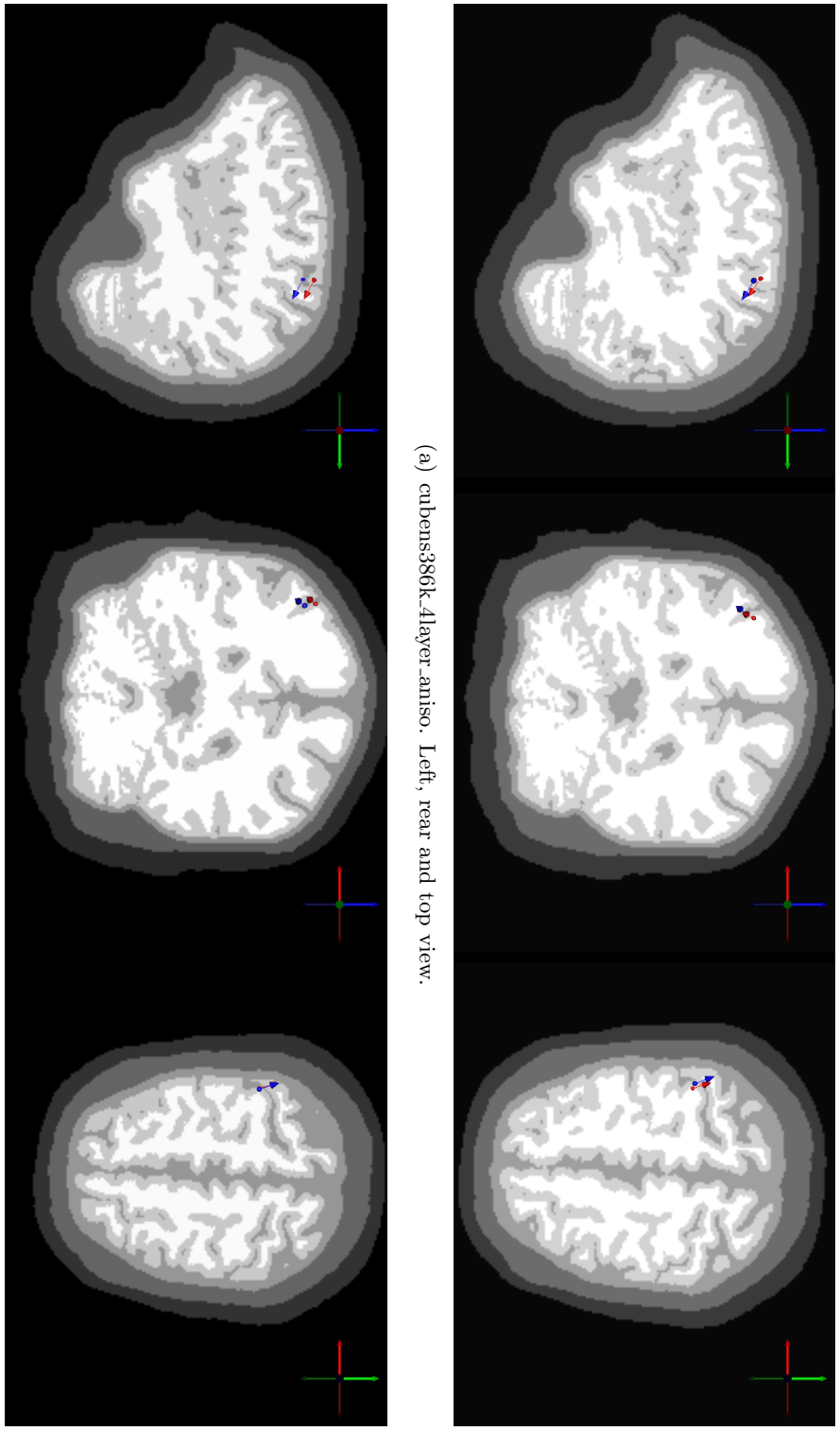

(a) cubens386k_4layer_aniso. Left, rear and top view.

(b) tet802k_4layer_aniso. Left, rear and top view.

Figure 6.4: Comparison of the EEG and MEG localisation results. Read arrow: EEG, Blue arrow: MEG.

7 Conclusion

In chapter (3) it was first shown that for the simulation of the EEG the FEM and BEM solutions converge with decreasing element width towards the exact solution. In general very low errors between the FEM solutions and the reference solutions were found for the EEG. The accuracies of the FEM solution for different element types were compared and it was found that nodeshifted hexahedra meshes and locally refined, high quality tetrahedra meshes are most accurate when simulating the electric potentials. Regarding the comparison to BEM FEM proved to be more accurate especially for multilayer sphere models with four layers and an anisotropic skull. In addition it can be stated from the results of the EEG multilayer sphere studies that the subtraction approach can be used to eliminate the oscillations of the errors which were observed for the Venant approach.

In the MEG studies it was confirmed that the secondary magnetic flux does not contribute to the radial component of the magnetic field produced by a dipole in a sphere. But it was shown that it does contribute to the tangential components. The errors of the numerical solutions for the secondary magnetic flux were studied and found to be very low. Furthermore it was shown that for tangential mangetometers primarily the errors of the secondary magnetic flux are responsible for the errors of the total magnetic flux. So especially for sensors which measure tangential components of the magnetic field it is important to accurately simulate the secondary magnetic flux. For the MEG the subtraction approach showed to significantly improve the accuracy of the FEM solution for the secondary magnetic flux and therefore the accuracy of the total magnetic flux.

Finally it can be concluded that the computation times needed for both numerical methods are comparable and acceptable short for an application in EEG and MEG source reconstruction.

In the study on the source reconstruction from MEG data recorded for current dipoles in phantom head model in chapter (4) the dipole locations and orientations could be accurately, that is with an average error around 3 mm resp. 3.5°, reconstructed using the finite element method. For the solution of the inverse problem both inverse methods, the moving dipole fit and the goal function scan, proved to be capable. It was furthermore shown that the noise rejection with 3rd order synthetic gradiometers is able to improve the source reconstruction for deep sources.

The same high accuracies for the EEG and MEG forward computations with FEM as in the multilayer sphere study could also be observed in the realistic head model (chapter 5). And comparing the accuracy for the different element types it was here, too, found that FEM in the nodeshifted hexahedra mesh delivers the best results. The low errors of the simulated electric potentials and magnetic fields directly translated to small localisation errors of the moving dipole fits on synthetic data in the realistic volume conductor. For the comparison between BEM and FEM it was again obvious that BEM

because its limitation on only three compartments and isotropic conductivities cannot be as accurate as FEM.

The results from chapter (6) finally showed that the finite element method can be applied to realistic data from neurophysiological experiments to realiably solve the inverse problem. The moving dipole fits on the realistic data using FEM for the forward computations delivered resonable locations and orientations of the current dipole source.

It can be concluded from all the studies that the finite element method can be employed to accurately solve the forward and therefore the inverse problem of EEG and MEG source reconstruction. It even outperforms other today still widely used numerical methods like the boundary element method. Using the subtraction approach for modelling the mathematical current dipole and using high quality and locally refined tetrahedra meshes can greatly improve the accuracy. For neurophysiological experiments FEM could help to more accurately determine the brain regions which are responsible for a certain task and in the epilepsy research, e.g., defective areas could be located more precisely.

Bibliography

[1] M. Akhtari, H. Bryant, A. Marmelak, E. Flynn, L. Heller, J. Shih, M. Mandelkern, A. Matlachov, D. Ranken, E. Best, M. DiMauro, R. Lee, and W. Sutherling. Conductivities of three-layer live human skull. *Brain Top.*, 14(3):151–167, 2002.

[2] M. Akhtari, H. Bryant, A. Marmelak, L. Heller, J. Shih, M. Mandelkern, A. Matlachov, D. Ranken, E. Best, and W. Sutherling. Conductivities of three-layer human skull. *Brain Top.*, 13(1):29–42, 2000.

[3] S. Baillet, L. Gernero, G. Marin, and J.-P. Hugonin. Combined MEG and EEG source imaging by minimization of mutual information. *IEEE Trans. on Biomed. Eng.*, 1998.

[4] H. Berger. Über das Elektrenkephalogramm des Menschen. *Arch.Psychiat.Nervenkr.*, 87:527–570, 1929.

[5] H. Buchner, G. Knoll, M. Fuchs, A. Rienäcker, R. Beckmann, M. Wagner, J. Silny, and J. Pesch. Inverse localization of electric dipole current sources in finite element models of the human head. *Electroenc. Clin. Neurophysiol.*, 102:267–278, 1997.

[6] M. Clerc, R. Keriven, O. Faugeras, J. Kybic, and T. Papadopoulo. The fast multipole method for the direct E/MEG problem. In *Proceedings of ISBI'2002*, 2002.

[7] D. Cohen. Magnetoencephalography: Evidence of magnetic field produced by alpharythm currents. *Science*, 161:784–786, 1968.

[8] P. Cohen, E. A. Edelsack, and J. E. Zimmerman. Magnetocardiograms taken inside a shielded room with a superconducting point-contact magnetometer. *Appl. Phys. Lett.*, 16:278–280, 1972.

[9] 2000. CURrent Reconstruction and Imaging, http://www.neuro.com.

[10] J. de Munck. The potential distribution in a layered anisotropic spheroidal volume conductor. *J. Appl. Phys.*, 64:465–469, 1988.

[11] N. Gencer and C. Acar. Sensitivity of EEG and MEG measurements to tissue conductivity. *Phys.Med.Biol.*, 49:701–717, 2004.

[12] D. B. Geselowitz. On bioelectric potentials in an inhomogeneous volume conductor. *Biophys J*, 7:1–11, 1967.

[13] R. S. Hosek, A. Sances, R. W. Jodat, and S. J. Larson. The contributions of intracerebral current to the EEG and evoked potentials. *IEEE Trans. Biomed. Eng.*, 25:405–413, 1987.

[14] J. Meijs, O. Weier, M. Peters, and A. van Oosterom. On the numerical accuracy of the boundary element method. *IEEE Trans Biomed. Eng.*, 36:1038–1049, 1989.

[15] J. Mosher, P. Lewis, and R. Leahy. Multiple dipole modeling and localization from spatio-temporal MEG data. *IEEE Trans Biomed. Eng.*, 39(6):541–557, 1992.

[16] J. Nelder and R. Mead. A simplex method for function minimization. *Comp.J.*, 7:308–313, 1965.

[17] C. R. Noback, N. L. Strominger, R. J. Demarest, and D. A. Ruggiero. *The human nervous system.* Humana Press, sixth edition, 2005.

[18] J. Pesch. Überprüfung inverser Feldberechnungen im Modell am Beispiel des Elektroencephaologramms. Diplomarbeit in Physik, Rheinisch-Westfälische Technische Hochschule Aachen, 1995.

[19] R. Pohlmeier. Lokalisation elektrischer Gehirnaktivität durch inverse Analyse des Magnetoenzephalogramms (MEG) mit Finite-Elemente-Modellen des Kopfes. Diplomarbeit in Elektrotechnik, RWTH Aachen, 1996.

[20] A. C. Rose-Innes and E. H. Rhoderick. *Introduction to Superconductivity.* Pergamon Press, 2nd edition, 1968.

[21] J. Sarvas. Basic mathematical and electromagnetic concepts of the biomagnetic inverse problem. *Phys.Med.Biol.*, 32(1):11–22, 1987.

[22] H. P. Schwan and C. F. Kay. The conductivity of living tissues. *Ann. N. Y. Acad. Sci.*, 65:1007–1013, 1975.

[23] H. R. Schwarz. *Methode der finiten Elemente*, volume 47 of *Leitfäden der angewandten Mathematik und Mechanik.* Teubner Studienbücher, 3rd edition, 1991.

[24] H. Si. Tetgen. http://tetgen.berlios.de.

[25] H. Si. *TetGen User's Manual*, 2006.

[26] 2000-2003. SimBio: A Generic Environment for Bio-Numerical Simulation, IST-Program of the European Commission, Project No.10378, http://www.simbio.de.

[27] U.Hartmann and G.Berti. Vgrid: A fast and robust octree-based 3d mesh generator for unstructured grids. [26], 2000-2003.

[28] J. Vrba. Multichannel squid biomagnetic systems. In H. Weinstock, editor, *Applications of Superconductivity*, pages 61–138. Kluwer Academic Publishers, Dordrecht, 2000.

[29] J. Vrba and S. E. Robinson. Signal processing in magnetoencephalography. *Methods*, 25(2):249–271, October 2001.

[30] VSM MedTech System Inc. *Phantom Manual*, 2006. VSM part number PN900-0018.

[31] M. Wagner. *Rekonstruktion neuronaler Ströme aus bioelektrischen und biomagnetischen Messungen auf der aus MR-Bildern segmentierten Hirnrinde*. PhD thesis, Shaker-Verlag Aachen, ISBN 3-8265-4293-2, 1998.

[32] Y. Wang, D. Haynor, and Y. Kim. An investigation of the importance of myocardial anisotropy in finite-element modeling of the heart: Methodology and application to the estimation of defibrillation efficacy. *IEEE Trans Biomed. Eng.*, 48(12), 2001.

[33] D. Weinstein, L. Zhukov, and C. Johnson. Lead-field bases for electroencephalography source imaging. *Annals of Biomed.Eng.*, 28(9):1059–1066, 2000.

[34] C. Wolters. Direkte Methoden zur Berechnung dipolinduzierter elektrischer und magnetischer Felder und inverse Strategien zur Quellokalisation im Gehirn. Diplomarbeit in Mathematik mit Nebenfach Medizin, Institut für Geometrie und Praktische Mathematik, RWTH Aachen, 1997.

[35] C. Wolters. *Influence of Tissue Conductivity Inhomogeneity and Anisotropy on EEG/MEG based Source Localization in the Human Brain*. Number 39 in MPI Series in Cognitive Neuroscience. MPI of Cognitive Neuroscience Leipzig, 2003. ISBN 3-936816-11-5 (also: Leipzig, Univ., Diss., http://dol.uni-leipzig.de).

[36] C. Wolters, H. Köstler, C. Möller, J. Härtlein, L. Grasedyck, and W. Hackbusch. Numerical mathematics of the subtraction method for the modeling of a current dipole in eeg source reconstruction using finite element head models. *SIAM J. on Scientific Computing*, 2006.

[37] C. H. Wolters, A. Anwander, G. Berti, and U. Hartmann. Geometry-adapted hexahedral meshes improve accuracy of finite element method based EEG source analysis. *IEEE Trans.Biomed.Eng.*, November 2006. accepted for publication.

[38] C. H. Wolters, L. Grasedyck, and W. Hackbusch. Efficient computation of lead field bases and influence matrix for the FEM-based EEG and MEG inverse problem. *Inverse Problems*, 20(4):1099–1116, 2004.

Erklärung

Hiermit versichere ich, dass ich diese Arbeit selbständig verfasst und keine anderen als die angegebenen Quellen und Hilfsmittel benutzt habe.

Münster, den 20.09.2007